

FATIGUE DAMAGE UNDER VARIABLE
AMPLITUDE LOADS

By

ZHENDONG ZHOU
周震东

Bachelor of Science
Dalian Institute of Technology
Dalian, P.R. of China
1982

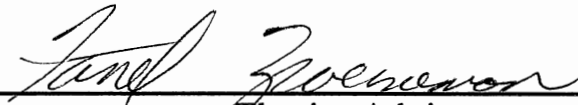
Master of Science
Northeast University of Technology
Shenyang, P.R. of China
1986

Submitted to the Faculty of the
Graduate College of the
Oklahoma State University
in partial fulfillment of
the requirements for
the Degree of
DOCTOR OF PHILOSOPHY
July, 1991

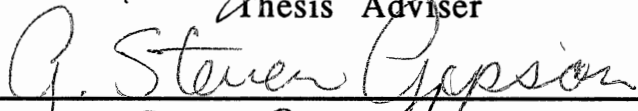
Thesis
1991D
Z63P
cop. 2


FATIGUE DAMAGE UNDER VARIABLE
AMPLITUDE LOADS

Thesis Approved:




Thesis Adviser









Dean of the Graduate College

ACKNOWLEDGMENTS

I wish to express my sincere gratitude to the individuals who assisted me in this work. In particular, I am indebted to my major adviser, Dr. Farrel J. Zwerneman, for his invaluable assistance especially in the experimental phase, and for his guidance and encouragement throughout my PhD study. I am also grateful to the other committee members, Dr. William P. Dawkins, Dr. G. Steven Gipson, and Dr. C. E. Price, for their support, advisement, and assistance during the course of this study. Particular appreciation is extended to Dr. John P. Lloyd for his help, especially in the experimental phase. The advisement of Dr. Steven Y. Liang, who once served on my graduate committee, is also appreciated.

I am grateful to the School of Civil Engineering for supporting this research and funding a new fatigue testing machine. The Structural Engineering Laboratory is acknowledged for providing the experimental facilities for this study. The help of Mr. Don Spoonemore in preparing the experimental setup is sincerely appreciated. Finally, my thanks go to Ms. Charlene Fries for her proofreading the final manuscript.

This thesis is dedicated to my family for their love, sacrifice, support, encouragement, and patience during my PhD study.

TABLE OF CONTENTS

Chapter	Page
I. INTRODUCTION	1
Problem Statement	1
Scope of Work	3
II. LITERATURE REVIEW	5
Effect of Isolated Overloads on Fatigue Damage	5
Experimental Observations	5
Physical Models of the Overload Effect	9
Computational Models of Crack Growth	12
Threshold Behavior of Fatigue Crack Growth	19
Acoustic Emission From Metal Fatigue	23
Acoustic Emission Characteristics	24
Signal Collection	26
Signal Processing	29
Methodology of CMOD, BFS, and Striation	
Measurements	32
Farfield Crack Opening Displacement	32
Fatigue Striations	34
III. EXPERIMENTAL INVESTIGATION	37
Specimens and Their Orientation	37
Specimen Description	37
Specimen Orientation	40
Loading Program	44
Loading Spectra	44
Loading Procedure	49
ΔK Precision	53
Macrocrack Growth Measurement	59
Apparatus	59
Procedure	59

Chapter	Page
Acoustic Emission Signal Acquisition	63
Instrumentation	63
Parameter Setting	71
Noise Isolation	72
AE Monitoring and Signal Processing	81
CMOD and BFS Measurements	84
Striation Observations	89
IV. RESULTS AND DISCUSSION	94
Macrocrack Growth	94
Transition in the Overload Effect	97
Fatigue Damage by Minor Cycles	118
Precision of the Crack Growth Rate Data	123
Acoustic Emission	131
Intermittent Nature of AE Signals	134
Threshold Behavior	135
Minor Cycle Stress Ratio Effect	140
CMOD and BFS	140
Crack Opening Observations.....	144
Feasibility of Determining K_{op}	150
Fatigue Striation	153
Striation Characteristics	153
Microcrack and Macrocrack Growth Rates	156
Summary of the Results	158
Overload Effect	158
Fatigue Damage by Minor Cycles	163
Additional Findings	165
V. SUMMARY AND CONCLUSIONS	168
Summary	168
Conclusions	169
Suggestions for Future Work	172
REFERENCES	173
APPENDICES	

Chapter	Page
APPENDIX A - CONFIDENCE LIMITS OF POPULATION MEAN BASED ON A GROUP OF DATA	189
APPENDIX B - CONFIDENCE LIMITS OF POPULATION MEAN BASED ON A REGRESSION LINE	191

LIST OF TABLES

Table		Page
1.	Chemical Composition of the CT Specimens	4 2
2.	Mechanical Properties of the CT Specimens	4 3
3.	A Summary of the Loading Spectra	4 6
4.	Crack Length Data from the Precision Test	6 1
5.	Summary of the Loading, Measuring, and Shedding Process (Specimen TH1)	64
6.	Summary of the Loading, Measuring, and Shedding Process (Specimen TH2)	6 6
7.	Locations of Striation Observations	9 3
8.	Summary of Crack Propagation Data (Specimen TH1)	9 5
9.	Summary of Crack Propagation Data (Specimen TH2)	9 6
10.	Crack Growth Data of Loading Group One	9 8
11.	Statistical Parameters of Previous Data	10 2
12.	90% Confidence Limits of the Overload Effect (Specimen TH1)	10 7
13.	90% Confidence Limits of the Overload Effect (Specimen TH2)	10 8
14.	90% Confidence Limits of the Overload Effect (Specimens TH1 and TH2)	109

Table		Page
15.	Crack Growth Data of Loading Group Three	122
16.	Crack Growth Data of Loading Group Four.	129
17.	Summary of AE Test Data	133
18.	AE Results of Loading Group One	136
19.	AE Results of Loading Group Two	141
20.	Microcrack Growth Data for Group Two Loading with $n = 49$	159
21.	Macrocrack Growth Data for Group Two Loading with $n = 49$	160

LIST OF FIGURES

Figure		Page
1.	Typical Retardation Behavior Following a Single Overload	6
2.	Effect of the Crack Increment Between Overloads on Retardation	7
3.	Plastic Zones in the Computational Residual Stress Models	15
4.	Three Regions of the Crack Growth Rate Curve	20
5.	A Typical Acoustic Emission Signal From Metal Fatigue	25
6.	A Typical Setup for Acoustic Emission Sensing	27
7.	A Typical Load-Displacement Curve	33
8.	The Functional Diagram of the Experimental Study	38
9.	A View of the Experimental Setup	39
10.	Dimensions of the Compact Tension Specimens Used	41
11.	Orientations of CT Specimens	45
12.	An Example of the Overload Spectra	48
13.	Loading Spectra With Different Minor Cycle Stress Ratios ..	50
14.	The ΔK Precision Curves for CT Specimens When $W=8$ in., $\Delta a_{max}=0.035, 0.046$ in.	57

Figure		Page
15.	The ΔK Precision Curves for CT Specimens When $W=2\text{ in.}$, $\Delta a_{max}=0.05\text{ in.}$	58
16.	The Traveling Microscope Fixture	60
17.	The Flow Chart of Acoustic Emission Signal Acquisition	68
18.	The Acoustic Emission Instrument Console	69
19.	Noise From the Machine Surroundings	74
20.	The FFT Spectrum of the Machine Surrounding Noise	75
21.	The Signal Measured After Using the Preamplifier With a High-Pass Filter	76
22.	Configuration of the Isolation Boxes	77
23.	Two Different Loading Trains for the Loading System	79
24.	An Example of the Signal Measured During the Trial Test	80
25.	An Example of the Signal Measured During the Trial Test After Using the Plastic Loading Pins	82
26.	An Example of the AE Events Recorded in a Peak Amplitude Vs. Time Form	83
27.	The Raw Signal of an AE Event Recorded in the Time Domain	85
28.	The Functional Diagram of the CMOD and BFS Measurement System	86
29.	An Example of the CMOD and BFS Signals Recorded	88
30.	Illustrations of the Crack Tip Position Marks and Beach Markings on a Fractured CT Specimen	90

Figure	Page
31. The Sample for Striation Observations	92
32. Overload Effect on Crack Growth of Specimen TH1	111
33. Statistical Demonstration of the Overload Effect With Crack Growth Rate Data from Specimen TH1	112
34. Overload Effect on Crack Growth of Specimen TH2	114
35. Statistical Demonstration of the Overload Effect With Crack Growth Rate Data From Specimen TH2	115
36. Summary of the Overload Effect on Crack Growth	116
37. Statistical Demonstration of the Overload Effect With Crack Growth Rate Data From both Specimens	117
38. Fatigue Damage Evaluations Using the Conventional and ASTM Baselines	121
39. Minor Cycle Stress Ratio Effect on Crack Growth	124
40. Effect of Crack Length on Crack Growth	130
41. Effect of Loading Pins on Crack Growth	132
42. Threshold Behavior Evaluated Using the AE Count and Amplitude Data	138
43. Threshold Behavior Evaluated Using the AE Energy Data	139
44. R_m Effect on the AE Count and Amplitude Data	142
45. R_m Effect on the AE Energy Data	143
46. A Typical CMOD Signal From Loading Group One	145

Figure		Page
47.	Crack Opening Observed From the CMOD Signal Under Group Two Loading With $n = 9$	146
48.	Crack Opening Observed From the BFS Signal Under Group Two Loading With $n = 9$	147
49.	Crack Opening Observed From the BFS Signal Under Group Two Loading With $n = 49$	149
50.	CMOD Vs. Load Curve of the First Overload in Group Two Loading With $n = 9$	151
51.	BFS Vs. Load Curve of the First Overload in Group Two Loading With $n = 9$	152
52.	Examples of the Striations Observed	154
53.	An Example of Evident Abrasive Damage on the Fracture Surface (Trial Specimen)	157
54.	Comparison of the Microcrack and Macrocrack Growth Rate Data From Loading Group Two	161
55.	Shape of the Confidence Limit Lines for a Regression Line.....	193

NOMENCLATURE

a	crack length
a_i	crack length at the i th cycle
a_{ol}	crack length at the overload cycle
B	specimen thickness
C	material constant
$(C_p)_i$	retardation parameter for the i th cycle
d_f	degree of freedom in a group of data
d_p	diameter of the crack tip plastic zone
F	a factor modifying the solution for an infinite center-cracked plate
K_c	fracture toughness
K_{max}	maximum stress intensity factor
$K_{m,max}$	maximum stress intensity factor of the minor cycle
$K_{m,min}$	minimum stress intensity factor of the minor cycle
$K_{o,max}$	maximum stress intensity factor of the overload cycle
$K_{o,min}$	minimum stress intensity factor of the overload cycle
K_{op}	crack opening stress intensity factor

$(K_{max}^e)_i$	maximum stress intensity factor of the i th cycle calculated using effective stresses
$(K_{min}^e)_i$	minimum stress intensity factor of the i th cycle calculated using effective stresses
$(K_{req})_i$	stress intensity factor required to generate a plastic zone of size $(r_{req})_i$
LL	lower confidence limit of the population mean of a group of data or a regression line
$(LL)_L$	lower confidence limit of the population mean of the regression line in Eq. (4.8)
$(LL)_m$	lower confidence limit of the population mean of the minor cycle crack growth rate
m	material constant
N	number of loading cycles applied
N_f	the final loading cycle
N_i	the initial loading cycle
N_s	number of data
n	number of minor cycles between overload cycles
n_c	number of loading cycles per complex cycle
n_s	number of original data for a regression calculation
n_t	total number of loading cycles
p	an empirical shaping parameter
$P_{m,max}$	maximum loading of the minor cycle

$P_{m,min}$	minimum loading of the minor cycle
$P_{o,max}$	maximum loading of the overload cycle
$P_{o,min}$	minimum loading of the overload cycle
q_{th}	threshold parameter in dB for the AE instrument
R	stress ratio
R_m	minor cycle stress ratio
R_o	overload stress ratio
R_Δ	ratio of ΔK_m to ΔK_o
$(R^e)_i$	stress ratio of the i th cycle calculated using effective stresses
$(r_{req})_i$	size of the plastic zone required to fully eliminate the overload effect at the i th cycle
$(r_p)_i$	size of the plastic zone resulting from the i th cycle
$(r_p)_{ol}$	size of the plastic zone resulting from the overload
S	estimate of the population variance of a group of data
$t_{\theta/2}$	t -distribution variable corresponding to $\theta/2$
UL	upper confidence limit of the population mean of a group of data or a regression line
$(UL)_L$	upper confidence limit of the population mean of the regression line in Eq. (4.8)
$(UL)_m$	upper confidence limit of the population mean of the

	minor cycle crack growth rate
v_{th}	threshold level for raw AE signals, determined by q_{th}
W	specimen width
x	independent variable of a regression line
\bar{x}	average of x over the original data for the regression calculation
y 's	individual number in a group of data
\bar{y}	average of y over a group of data
\hat{y}	regressional function
z	normal-curve variable
$\frac{da}{dN}$	a simplified form of $\left(\frac{da}{dN}\right)_N$
$\left(\frac{da}{dN}\right)_{com}$	complex cycle crack growth rate
$\left(\frac{da}{dN}\right)_m$	minor cycle crack growth rate
$\left(\frac{da}{dN}\right)_N$	crack growth rate of the N th cycle
$\left(\frac{da}{dN}\right)_o$	overload cycle crack growth rate
$\overline{\left(\frac{da}{dN}\right)_{com}}$	average of the complex cycle crack growth rate

$\left(\overline{\frac{da}{dN}}\right)_{com,ll,90}$	lower limit of the population mean of $\left(\overline{\frac{da}{dN}}\right)_{com}$ with 90% confidence
$\left(\overline{\frac{da}{dN}}\right)_{com,ul,90}$	upper limit of the population mean of $\left(\overline{\frac{da}{dN}}\right)_{com}$ with 90% confidence
$\left(\overline{\frac{da}{dN}}\right)_m$	average of the minor cycle crack growth rate
$\left(\overline{\frac{da}{dN}}\right)_{m,ll,95}$	lower limit of the population mean of the minor cycle crack growth rate with 95% confidence
$\left(\overline{\frac{da}{dN}}\right)_{m,ul,95}$	upper limit of the population mean of the overload crack growth rate with 95% confidence
$\left(\overline{\frac{da}{dN}}\right)_o$	average of the overload cycle crack growth rate
$\left(\overline{\frac{da}{dN}}\right)_{o,ll,90}$	lower limit of the population mean of the overload crack growth rate with 90% confidence
$\left(\overline{\frac{da}{dN}}\right)_{o,ul,90}$	upper limit of the population mean of the overload crack growth rate with 90% confidence
$\left(\overline{\frac{da}{dN}}\right)_{o,ll,95}$	lower limit of the population mean of the overload crack growth rate with 95% confidence
$\left(\overline{\frac{da}{dN}}\right)_{o,ul,95}$	upper limit of the population mean of the overload crack growth rate with 95% confidence
Δa	crack increment

Δa_{max}	maximum crack increment between load sheddings
Δa_1	crack increment corresponding to retardation delay
Δa_1^*	crack increment between overloads corresponding to maximum retardation
Δa_2	crack increment required to recover from retardation
Δa_2^*	crack increment between overloads corresponding to minimum retardation
ΔK	stress intensity range
ΔK_{eff}	a simplified form of $(\Delta K_{eff})_i$
ΔK_i	stress intensity range of the i th cycle
ΔK_m	minor cycle stress intensity range
ΔK_o	overload stress intensity range
ΔK_{rms}	root-mean-square stress intensity range
ΔK_{th}	threshold stress intensity range
$(\Delta K_{eff})_i$	effective stress intensity range of the i th cycle
$(\Delta K^e)_i$	stress intensity range of the i th cycle calculated using effective stresses
$(\Delta K)_N$	stress intensity range of the N th cycle
ΔP	load range
η	level of confidence in percentage
θ	$(1-\eta)$

α	ratio of a to W
σ_{op}	crack opening stress
σ_y	yield stress
$(\sigma_{max})_i$	maximum stress of the i th cycle
$(\sigma_{max}^e)_i$	effective stress of $(\sigma_{max})_i$
$(\sigma_{min})_i$	minimum stress of the i th cycle
$(\sigma_{min}^e)_i$	effective stress of $(\sigma_{min})_i$
$(\sigma_{req})_i$	stress required to generate a plastic zone of size $(r_{req})_i$
ξ	ΔK fluctuation resulting from Δa_{max}
ψ	$\frac{da}{dN}$ fluctuation resulting from Δa_{max}
$\hat{\beta}_0$	y-intercept of a regression line
$\hat{\beta}_1$	slope of a regression line

CHAPTER I

INTRODUCTION

Problem Statement

It has been estimated that 50 to 70% of machine and structure failures are due to fatigue [1]. Fatigue analysis is important for design, troubleshooting of service problems, and failure analysis. In the past, fatigue analysis has relied heavily upon fatigue data from constant-amplitude load-time histories [2, 3]. However, recent research reveals that for some variable-amplitude load-time histories, the traditional theory cannot provide satisfactory fatigue life estimates [4-6].

In a study by Zwerneman [6] where a loading program consisting of overloads separated by nine small cycles was applied to high-strength low-alloy steel samples, it was observed that the overloads accelerated the fatigue damage above that predicted by a linear damage summation model. The summation included both overloads and minor cycles. This observation is not in line with the traditional theory that overloads cause fatigue crack retardation [7-9]. This is alarming since it was suggested that overloads can be used to extend the fatigue lives of aircrafts [10, 11].

There are also reported cases of crack growth retardation resulting from overloading [12, 13]. It seems that overload retardation occurs under overloads at low rates of occurrence, while overload acceleration occurs under overloads at high rates of occurrence. There is a lack of knowledge concerning the transition between overload acceleration and retardation. A better understanding of this transition will contribute to an improved understanding of the mechanism of the overload effects on fatigue crack growth, and provide important information on when overloads are beneficial or detrimental.

It is generally accepted that no significant fatigue damage occurs under a certain loading level. This loading level is called the crack growth threshold. A large amount of fatigue crack threshold data have been documented in the literature [14-16]. These data were largely obtained under constant-amplitude load conditions and have been used for engineering design, fatigue testing, and failure analysis. However, it has been found that under variable-amplitude load conditions, reported threshold data sometimes fail to represent experimental results [17-19]. Further research on the fatigue crack threshold is needed to provide a better understanding of the threshold behavior, and more information on threshold values.

Among the many factors which the success of a fatigue study depends upon, the effectiveness of measuring techniques for fatigue damage is one of the most critical. Fatigue crack length, closure, and striations are the commonly used parameters for quantitative evaluation of fatigue damage. Recently, it was reported that the

acoustic emission technique can be used to study the crack propagation phase [20-25]. It is well accepted that fatigue damage in metals generates acoustic emission activities [26-29]. Research on aerospace structures showed that the acoustic emission signal is very sensitive to small crack increments. McBride and Maclachlan [30] discerned a crack increment of $20\text{ }\mu\text{m}$ on a specimen attached to a flying airplane. Horak and Weyhreter [31] detected cracks as small as 0.010 in. long by 0.002 in. deep in threads on a nose landing gear during fatigue testing. Carlyle and Scott [32] were able to detect a fatigue crack in a laboratory specimen at approximately 100,000 cycles before it could be confirmed by visual examination. These facts show that acoustic emission sensing is a promising technique. However, the acceptance of this technique in fatigue study has been very slow due to the experimental difficulty involved in isolation of testing machine noise from real fatigue damage signals. More studies are needed to promote its application.

Scope of Work

The present study investigates fatigue damage of ASTM A588 steel under variable amplitude loads. It focuses on:

1. the effect of isolated periodic overloads on fatigue crack growth, especially the transition phase; and
2. the threshold behavior of the steel.

Acoustic emission (AE), travelling microscopy (TM), back-face strain (BFS), crack mouth opening displacement (CMOD), and scanning electron microscopy (SEM) techniques are extensively employed in

this study. Some investigations were conducted into the applications of these techniques.

Details of this research are presented in the following chapters. Chapter II is a literature review of overload effects on fatigue damage, and fatigue damage caused by loading cycles below the threshold. The background on acoustic emission sensing, far-field crack opening displacement techniques, and the fatigue striation technique is also included. Chapter III describes the experimental investigation. Information on the experimental setup, loading program design, specimens and their orientation is presented. Several aspects relating to the application of the measuring techniques adopted, such as noise isolation in AE signal acquisition, are investigated. Chapter IV contains the results and discussion. The transition range of the overload effect is addressed statistically using the results from five groups of experimental data. The fatigue behavior of A588 steel below the crack threshold is discussed. The CMOD and BFS results are employed to interpret crack growth behavior. A comparison between the macrocrack and microcrack growth results is also demonstrated. Summary and conclusions for the present research are given in Chapter V. This chapter also contains suggestions for future research.

CHAPTER II

LITERATURE REVIEW

Effect of Isolated Overloads on Fatigue Damage

Experimental Observations

It is well accepted that a single overload causes crack growth retardation [33, 34]. Typical retardation phenomenon are illustrated in Fig. 1 for a condition of constant stress intensity range. In this figure, point *A* represents the point when a single overload is applied. After this point, the crack growth rate decreases rapidly until it reaches a minimum (point *B*), then it increases rapidly and converges to a constant value at point *C*. This value is lower than the crack growth rate before overloading. The crack tip at point *A* propagates through a distance, Δa_I , which is reported as being one-quarter of the size of the affected zone [33, 35], before arriving at point *B*. This behavior is termed "delayed retardation".

When another overload is added to the single overload program, it is expected that retardation still occurs. The number of loading cycles retarded was found to be dependent on the crack increment between the overloads [36], as shown in Fig. 2. Maximum retardation occurs when the crack increment between the two overloads, Δa_I^* , is equal to Δa_I (see Fig. 1). When the crack

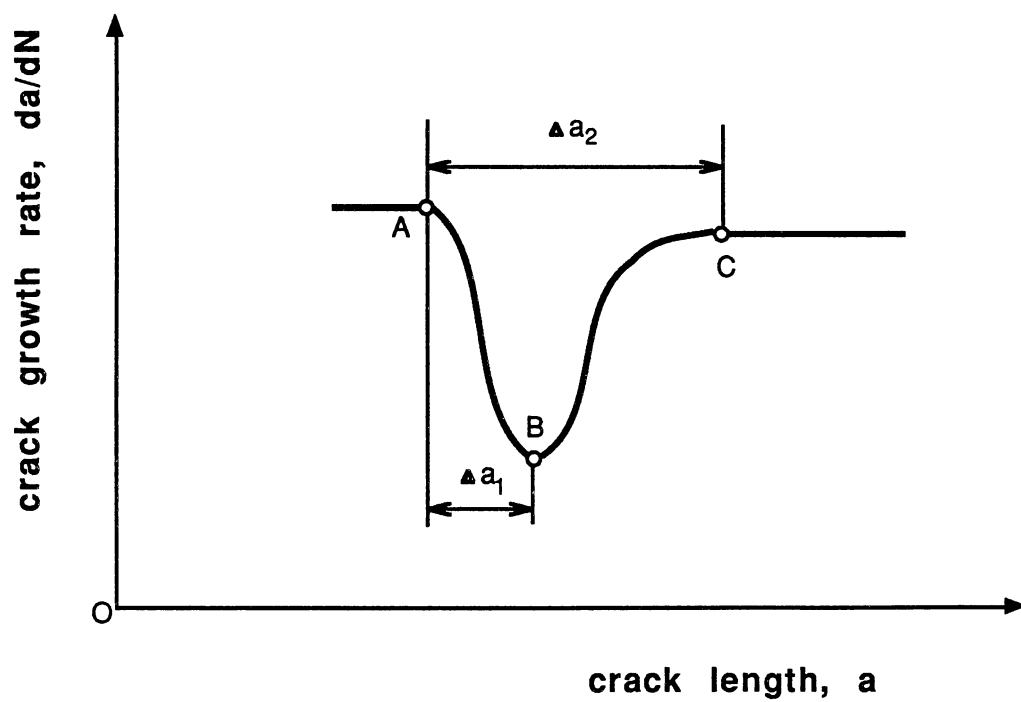


Figure 1. Typical Retardation Behavior Following a Single Overload

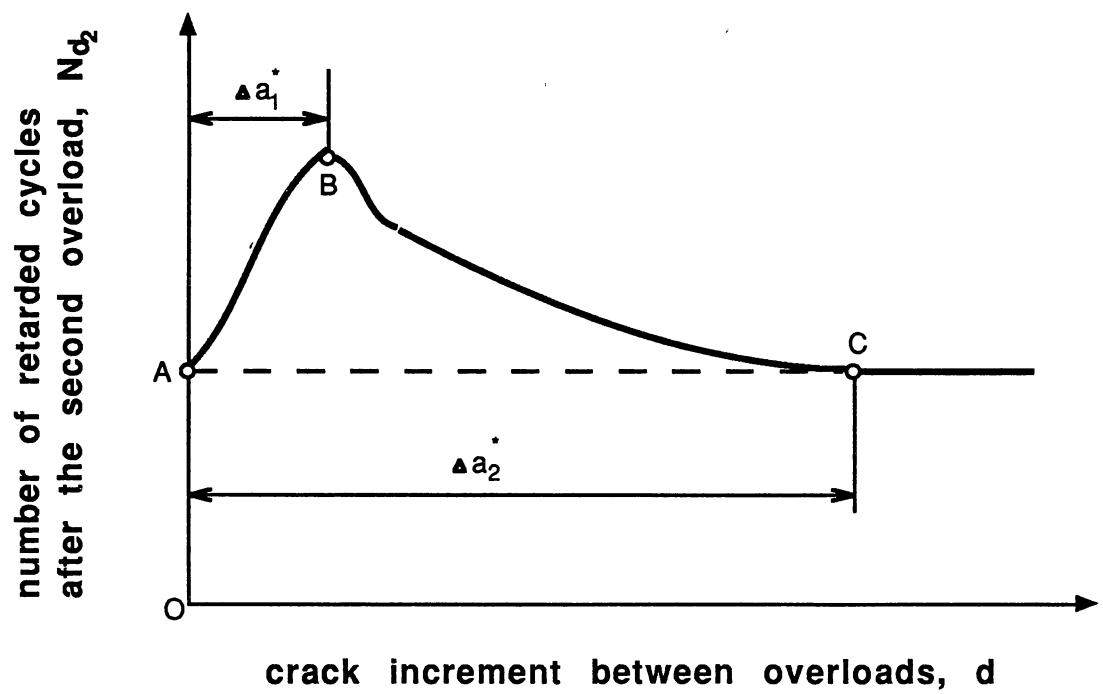


Figure 2. Effect of the Crack Increment Between Overloads on Retardation

increment is equal to or larger than Δa_2^* , the two overloads do not interact. The parameter Δa_2^* is approximately three times the size of the affected zone resulting from a single overload. It has been shown experimentally [12, 13, 18] that overloads isolated by a thousand minor cycles cause crack growth retardation in aluminum 2024, 2091, and 7075.

In a recent study by Zwerneman [6], crack growth acceleration was observed in compact tension specimens under overloads with a high rate of occurrence. The number of the minor cycles between the overloads was nine. The crack tip was tested under the mixed plain stress and plain strain condition. The baseline for the crack growth rate was the linear integration of the constant-amplitude load results. Computational models, such as Willenborg's model (refer to the section of Computational Models of the Crack Growth), were used to calculate the growth rate resulting from the minor cycles.

Albrecht [37, 38] investigated the effect of isolated overloads on the total fatigue life, i.e., the sum of the crack initiation life and the crack propagation life, of welded specimens. Some fatigue damage above the baseline was reported, but acceleration cannot be inferred because the baseline did not include the damage caused by the overload cycles.

Further support for the concept of crack growth acceleration induced by overloads is found in recent research [39-42] indicating that under certain conditions, crack growth acceleration occurs immediately after a single overload is applied and before retardation starts. The plain stress condition and small cracks were considered

to be the major factors contributing to acceleration. Therefore, if the time interval between two adjacent overloads is within the transient period of the acceleration, the isolated overloads might cause crack growth acceleration.

According to the above discussion of previous research, it is possible that overload retardation occurs when isolated overloads are separated by a large number of minor cycles, and overload acceleration occurs when overloads are separated by a small number of minor cycles. However, documented work on the transition between acceleration and retardation has not been found in the literature. One important focus of this research is to study the transition range of the overload effect on fatigue crack growth in A588 steel.

Physical Models of the Overload Effect

Various physical models have been proposed for the mechanism of crack growth after overloading in metals. Among them, the residual stress model [8], the crack tip blunting model [7, 43], and the plasticity-induced crack closure model [44] are the most popular. The first two can be used to account for some aspects of crack growth retardation behavior resulting from isolated overloads, but cannot provide information on crack growth acceleration behavior. The plasticity-induced crack closure model, the irregular crack front model [42, 45], and the crack tip strain hardening model [46] are relevant to the mechanism of acceleration.

Residual Stress Model. After a single peak overload is applied, residual stress ahead of the crack tip is compressive and higher than that generated by the previous minor tensile cycles. Since the compressive residual stress counteracts partly the effect of the tensile loading, the overload retards crack growth.

This model does explain why crack growth is slowed down by an overload, and is the basis of the computational models of Wheeler [47] and Willenborg [10] (refer to the section of Computational Models of the Crack growth). According to this model, the maximum crack growth retardation should occur immediately after overloading and the retardation should end when the crack is extended beyond the plastic zone. This is inconsistent with the concept of delayed retardation and the size of the retarded crack increment as illustrated in Fig. 1. Also, there are experimental results [48] showing that retardation is not caused by residual stresses.

Crack Tip Blunting Model. The overload cycle blunts the crack and hence reduces the stress concentration factor at the crack tip. Crack growth is retarded for a number of minor cycles following the overload until the crack is reinitiated and propagates from the blunted one.

Again, this model does not explain delayed retardation. An analytical study [35] showed the crack increment that might be retarded by blunting is only 2% of the minimum retarded crack increment observed. Another common limitation of the two models is the lack of explanation for crack growth acceleration.

Plasticity-Induced Crack Closure Model. An overload produces a large plastic deformation zone similar to the one in the residual stress model. When the crack propagates into the plastic zone, the residual deformation left behind the crack tip retards the crack growth.

This model can be extended conceptually to predict acceleration. Delayed retardation can also be explained using the crack closure concept, but certain reported cases concluded the plasticity-induced crack closure model failed to account for the retarded crack growth [49, 50].

Irregular Crack Front Model. After overloading, crack branching and microcracking occur ahead of the crack tip. These irregularities in the crack front usually reduce the stress intensity factor. Hence, it was suggested [45] that the irregular crack front causes crack growth retardation. However, accelerated crack growth in thin specimens of 2024-T4, 7075-T6, and 6061-T6 aluminum was also attributed to overload-induced crack branching [42]. It was suggested that under certain conditions, the overload may accelerate crack growth along the heavily deformed shear band in the irregular crack front.

Crack Tip Strain Hardening Model. Strain hardening around the crack tip after overloading was first considered as the cause of the crack growth retardation, because the excessive, plastic deformation strengthens the material in the vicinity of the crack tip [46]. But it was found later [46, 51] that cracks in strain-hardening materials

grow faster in the prestrained material condition than in the as-received condition. Thus, strain hardening may result in crack growth acceleration due to reduced ductility.

As shown above, none of the currently existing models is capable of depicting a complete picture of crack growth behavior after overloading. But each model points out some important factors governing the post-overload crack growth.

Computational Models of Crack Growth

Computational models have been developed to quantify crack growth after overloading. They can be classified into four categories: non-interaction models, residual stress models, crack closure models, and statistical models. Residual stress models and crack closure models can be used to predict crack growth retardation resulting from overloading, but none of the available computational models accounts for acceleration.

Non-Interaction Model. The non-interaction model for crack propagation is also called the direct integration model. In the direct integration model, the interaction effect between the overloads is ignored, and the crack growth increment is calculated by directly summing up the effect of each loading cycle applied. For example, using the Paris law [3],

$$\left(\frac{da}{dN}\right)_N = C[(\Delta K)_N]^m \quad (2.1)$$

this model yields,

$$\Delta a = \int_{N_i}^{N_f} C[(\Delta K)_N]^m dN \quad (2.2)$$

where C and m are material constants, N is the number of the loading cycles, $\left(\frac{da}{dN}\right)_N$ and $(\Delta K)_N$ are the crack growth rate and stress intensity range of the N th-cycle, N_i and N_f are the initial and final loading cycles, and Δa is the crack increment between the loading cycle N_i and N_f . This model accounts for neither crack growth acceleration nor retardation. It can provide a base line for study of the overload effect.

Residual Stress Models. The residual stress models are based on the concept that compressive residual stresses generated by an overload are the primary cause of crack growth retardation. The Wheeler [47] and Willenborg models [10] are two examples of this class of computational model. In both models, retardation reaches its maximum immediately after overloading, then decreases gradually as the crack propagates into the plastic zone, and finally converges to a constant level if no more overload is applied. The two models differ in the manner in which this behavior is described analytically.

The Wheeler model adopts an empirical retardation parameter to modify the direct integration model. For the i th cycle after overloading, the crack growth rate is expressed as

$$\left(\frac{da}{dN}\right)_i = (C_p)_i \{C[(\Delta K)_i]^m\} \quad (2.3)$$

where $(C_p)_i$ is the retardation parameter for the i th cycle. This retardation parameter can be written as,

$$(C_p)_i = \begin{cases} \left[\frac{(r_p)_i}{(r_{req})_i} \right]^p, & (r_p)_i < (r_{req})_i \\ 1, & (r_p)_i \geq (r_{req})_i \end{cases} \quad (2.4)$$

where p is an empirical shaping parameter, $(r_p)_i$ is the size of the plastic zone resulting from the i th cycle, and $(r_{req})_i$ is the size of the plastic zone required to fully eliminate the overload effect at the i th cycle, as shown in Fig. 3. The variable $(r_{req})_i$ is equivalent to the distance between the crack tip and the boundary of the plastic zone generated by the overload,

$$\begin{aligned} (r_{req})_i &= a_{ol} + (r_p)_{ol} - a_i \\ &= a_{ol} + \frac{1}{\beta\pi} \left(\frac{K_{o,max}}{\sigma_y} \right)^2 - a_i \end{aligned} \quad (2.5)$$

where a_{ol} and a_i are crack lengths at the overload cycle and the i th cycle respectively; $(r_p)_{ol}$ is the size of the plastic zone generated by the overload; $K_{o,max}$ is the maximum stress intensity factor for the overload cycle; σ_y is the yield strength of the material; and the

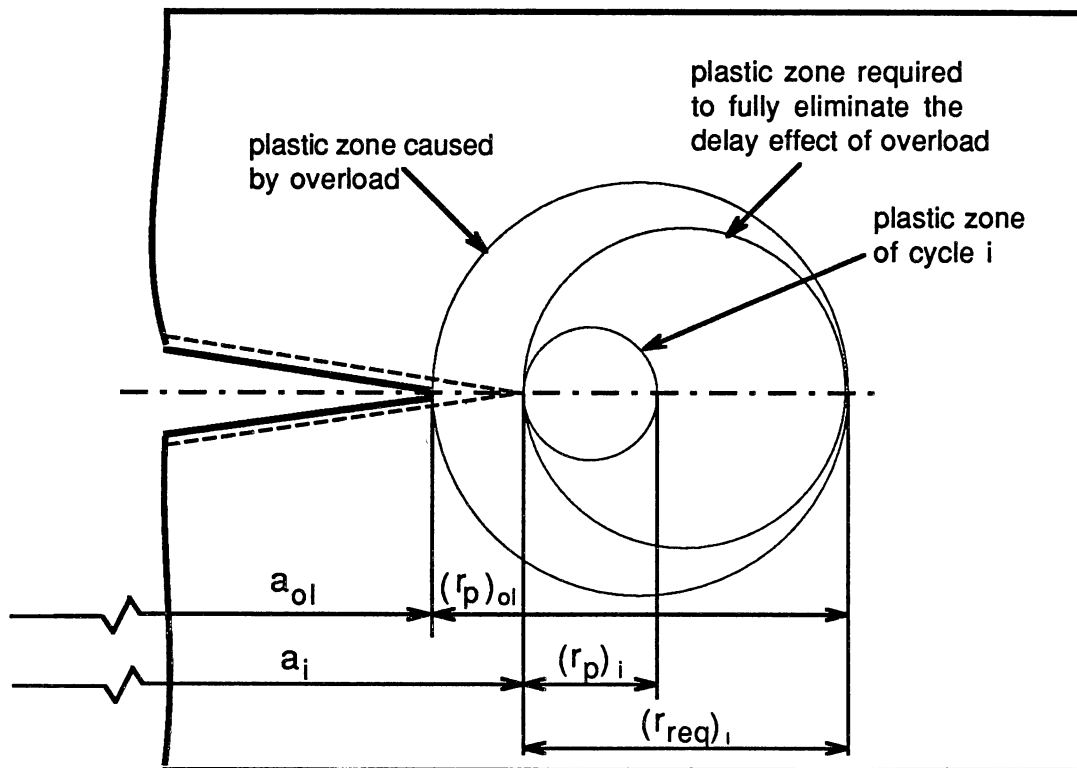


Figure 3. Plastic Zones in the Computational Residual Stress Models

parameter β is 2 for the plain stress condition or 6 for the plain strain condition.

Instead of using a retardation parameter, the Willenborg model introduces the concepts of "effective stress" and "compressive stress". The parameter $(r_{req})_i$ from Eq.(2.5) is now expressed as

$$(r_{req})_i = \frac{1}{\beta\pi} \left(\frac{K_{req}}{\sigma_y} \right)^2 \quad (2.6)$$

where $(K_{req})_i$ is the stress intensity factor required to generate the plastic zone of size $(r_{req})_i$. The variable $(K_{req})_i$ is a function of the stress required to generate that zone $(\sigma_{req})_i$, and the crack length at the i th cycle, a_i .

$$(K_{req})_i = F (\sigma_{req})_i \sqrt{\pi a_i} \quad (2.7)$$

where F is a factor used to modify the solution for an infinite center-cracked plate for the effects of free surface, finite width, nonuniform opening stresses, and elliptical crack front [52]. Combining Eqs. (2.5) through (2.7) results in,

$$(\sigma_{req})_i = \frac{\sigma_y}{F} \sqrt{\frac{\beta}{a_i} \left[a_{ol} + \frac{1}{\beta\pi} \left(\frac{K_{o,max}}{\sigma_y} \right)^2 - a_i \right]} \quad (2.8)$$

The compressive stress of the i th-cycle is defined as,

$$(\sigma_{com})_i = \begin{cases} [(\sigma_{req})_i - (\sigma_{max})_i], & (\sigma_{req})_i > (\sigma_{max})_i \\ 0, & (\sigma_{req})_i \leq (\sigma_{max})_i \end{cases} \quad (2.9)$$

The effective stresses of the i th cycle are defined as,

$$(\sigma_{max}^e)_i = \begin{cases} [(\sigma_{max})_i - (\sigma_{com})_i], & (\sigma_{max})_i > (\sigma_{com})_i \\ 0, & (\sigma_{max})_i \leq (\sigma_{com})_i \end{cases} \quad (2.10)$$

$$(\sigma_{min}^e)_i = \begin{cases} [(\sigma_{min})_i - (\sigma_{com})_i], & (\sigma_{min})_i > (\sigma_{com})_i \\ 0, & (\sigma_{min})_i \leq (\sigma_{com})_i \end{cases} \quad (2.11)$$

where $(\sigma_{max})_i$ and $(\sigma_{min})_i$ are the maximum and minimum actual stresses in the i th cycle, and $(\sigma_{max}^e)_i$ and $(\sigma_{min}^e)_i$ are the effective stresses of $(\sigma_{max})_i$ and $(\sigma_{min})_i$.

In the Willenborg model, the stress intensity factors and the stress ratio are determined using the effective stresses rather than the actual stresses. The stress intensity factors and the stress ratio are expressed as,

$$(K_{max}^e)_i = (\sigma_{max}^e)_i \sqrt{\pi a_i} F \quad (2.12)$$

$$(K_{min}^e)_i = (\sigma_{min}^e)_i \sqrt{\pi a_i} F \quad (2.13)$$

$$(\Delta K^e)_i = (K_{max}^e)_i - (K_{min}^e)_i \quad (2.14)$$

$$(R^e)_i = \frac{(K_{min}^e)_i}{(K_{max}^e)_i} \quad (2.15)$$

where $(K_{max}^e)_i$ and $(K_{min}^e)_i$ are the maximum and minimum stress intensity factors of the i th cycle, and $(\Delta K^e)_i$ and $(R^e)_i$ are the stress intensity range and the stress ratio of the i th cycle. The parameters $(\Delta K^e)_i$ and $(R^e)_i$ can be used with the Paris law, Eq. (2.1), or the Forman equation [53]. Using the Paris law, the Willenborg model yields,

$$\left(\frac{da}{dN}\right)_i = C [(\Delta K^e)_i]^m \quad (2.16)$$

Using the Forman law, the model leads to,

$$\left(\frac{da}{dN}\right)_i = \frac{C [(\Delta K^e)_i]^m}{[1 - (R^e)_i] K_c - (\Delta K^e)_i} \quad (2.17)$$

where K_c is the fracture toughness of the specimen material.

Crack Closure Models. This type of model originates from the physical model of plasticity-induced crack closure. The crack opening stress, σ_{op} , takes the place of the minimum stress in the loading cycle when the stress intensity range is calculated. That is,

$$(\Delta K_{eff})_i = F [(\sigma_{max})_i - (\sigma_{op})_i] \sqrt{\pi a_i} \quad (2.18)$$

where $(\Delta K_{eff})_i$ is the effective stress intensity range for the i th cycle. The crack opening stress is usually calculated using finite element methods [9, 54-56]. If the Paris law is used, the crack growth rate

for the i th cycle is,

$$\left(\frac{da}{dN}\right)_i = C [(\Delta K_{eff})_i]^m \quad (2.19)$$

Statistical Models. Similar to the direct integration model, the statistical models do not account for interaction effects between overloads. These models statistically calculate the average fatigue crack growth rate using data from each loading cycle. For example, the root-mean-square stress intensity range is defined as [57],

$$\Delta K_{rms} = \sqrt{\sum_{i=1}^{n_t} \frac{[(\Delta K)_i]^2}{n_t}} \quad (2.20)$$

where n_t is the total number of the loading cycles, and ΔK_i is the stress intensity range of the i th cycle. The statistical crack growth rate with the Paris law is,

$$\frac{da}{dN} = C (\Delta K_{rms})^m \quad (2.21)$$

Threshold Behavior of Fatigue Crack Growth

The curve of crack growth rate versus stress intensity factor can be divided into three regions as illustrated in Fig. 4. In region III, the crack growth rate is extremely high and the fatigue life is usually insignificant. In region II, the growth curve is basically linear and

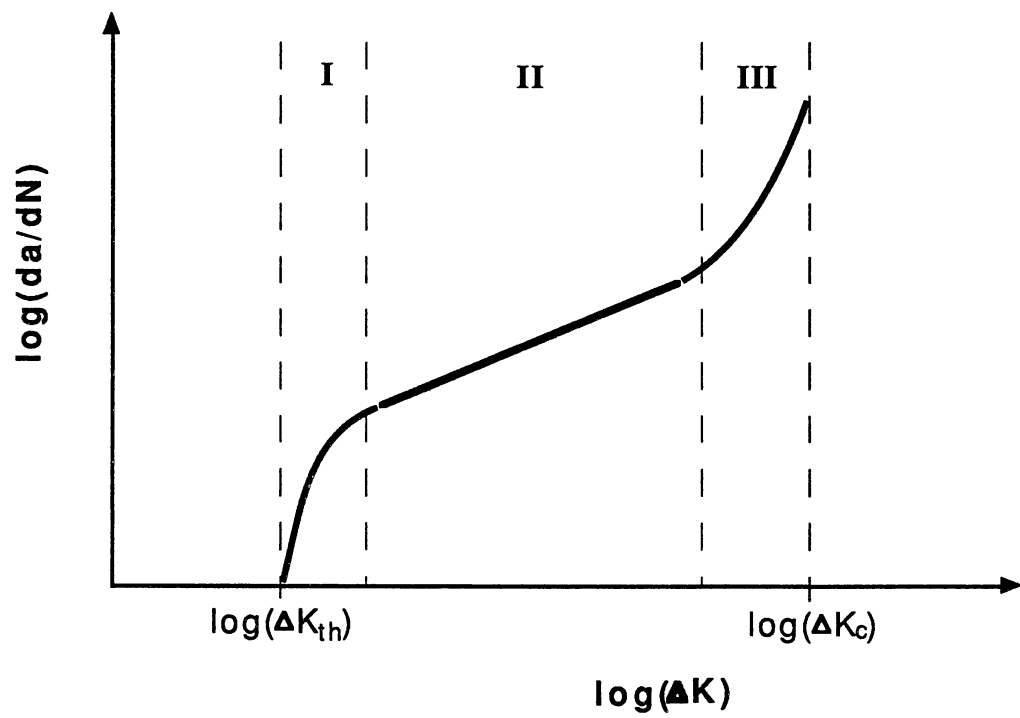


Figure 4. Three Regions of the Crack Growth Rate Curve

several crack growth laws (e.g., the Paris law) have been developed to predict crack growth rates under loading cycles of given stress intensity ranges. In region I, the crack growth rate decreases rapidly as the stress intensity range decreases. When the crack growth rate is below a certain value, crack growth becomes so slow that the growth rate can be considered to be zero. There are several numbers frequently used in the literature as this nominal zero growth rate. They range from 2.5×10^{-10} m/cyc [58], to 10^{-8} m/cyc [34], to 10^{-7} m/cyc [59]. The number recommended by the American Society for Testing and Materials is 10^{-10} m/cyc [60]. The corresponding stress intensity range, ΔK_{th} , is called the threshold stress intensity range or the crack growth threshold. The threshold behavior is of interest to this research.

Many fatigue threshold data have been published by various investigators [14-16, 58, 59]. Most of these data were obtained under constant-amplitude loads. In an attempt to predict the threshold values, Barsom [14] studied various crack growth threshold data reported for seven types of steel. He suggested that a conservative estimate of the threshold stress intensity range for a given stress ratio, R , could be [34, 61]

$$\Delta K_{th} = \begin{cases} [6.4 (1 - 0.85R)] (ksi \sqrt{in}), & R > 0.1 \\ 5.5 (ksi \sqrt{in}), & R \leq 0.1 \end{cases} \quad (2.22)$$

According to this equation, the fatigue crack propagation threshold is only a function of the stress ratio, and is independent of the material

properties of the steels tested. The fatigue threshold decreases with increasing stress ratio when the stress ratio is above 0.1.

However, when variable-amplitude loads were applied, it was found [17] that the concept of a crack growth threshold may not be applicable. To study the fatigue crack growth behavior of steel under variable-amplitude loads mainly consisting of below-threshold cycles, Fisher [17] adopted random-block variable-amplitude stress spectra with a Rayleigh-type distribution. From the crack growth data, he concluded that the existence of a crack growth threshold below which no fatigue crack propagation occurs is assured only if none of the stress cycles exceeds this constant-amplitude load threshold. If any of the stress cycles exceed the threshold, fatigue crack propagation will likely occur at a rate indicated by taking all cycles to be damaging.

Koterazawa [62] further studied threshold behavior under variable-amplitude loading conditions. In the loading program he used, overload blocks consisting of a few overload cycles were separated by a large number of small cycles below the threshold. Significant acceleration of crack propagation (more than one hundred times the damage calculated using the non-interaction model) was observed. He concluded that the threshold stress intensity range loses its physical meaning under such loading conditions.

The fatigue limit in conventional fatigue analysis is similar to the crack growth threshold in fracture mechanics. Under variable-amplitude loads, unexpectedly short fatigue lives were observed in some steel [63] and aluminum [19] components when the majority of

the loading cycles were below the constant-amplitude fatigue limits. It was concluded [63] that as long as some stresses exceed the constant-amplitude fatigue limit, damage should be assumed to occur under all cycles. In Ref. [19], it was also found that omission of cycles lower than one-half of the endurance limit increased the total life by 30 to 70%.

From the above review of threshold behavior under variable-amplitude loading programs with the majority of cycles below the threshold, it seems the existence of the high cycles accelerated crack growth rather than retarded it. However, as mentioned earlier, overload cycles may result in crack growth acceleration in some cases and retardation in others. Therefore, it will be interesting to examine the fatigue damage contributions of the below-threshold loading cycles and the high cycles. This research will explore the effect of the occurrence rate of the overload cycles, separated by a number of minor cycles in a loading program, on the fatigue damage of A588 steel.

Acoustic Emission From Metal Fatigue

Acoustic emissions are transient elastic stress waves generated as a result of rapid strain energy release from localized sources within solid materials [64]. In fatigue testing, acoustic emissions result from three major sources [25]: (1) material deformation and fracture within the plastic zone around the crack tip, (2) crack extension, and (3) crack closure or friction between the crack surfaces. The acoustic emission signal measured during fatigue

testing might provide insight as to the fatigue damage within the material. As mentioned in the introduction, earlier research has shown that acoustic emission signals from fatigue testing are very sensitive to small crack increments, and signal identification and noise isolation have been major obstacles to the application of this technique. This research will attempt to apply acoustic emission sensing to the overload study. The following is an introduction to the characteristics of acoustic emission signals from fatigue testing and the signal measurement technique.

Acoustic Emission Characteristics

In primitive form, the acoustic emission wave is generally a simple step or pulse [65]. However, due to signal reflections and separations in the course of propagation from different sources to the AE sensor, the measured signal is rather random and complicated. There are basically two types of acoustic emission signals: the burst type and the continuous type. A typical AE signal of the burst type is shown in Fig. 5 [65]. A continuous signal is composed of many burst signals occurring at a high frequency and overlapping with respect to time. The acoustic emission signals from fatigue testing are of the burst type.

Generally speaking, the intensity of the acoustic emission signal is material-dependent. For example, aluminum generates higher AE signals during fatigue testing than steels [66]. For steels, the higher the material strength, the more intense the acoustic emission [25]. It has also been observed [67] that the AE signals resulting from crack

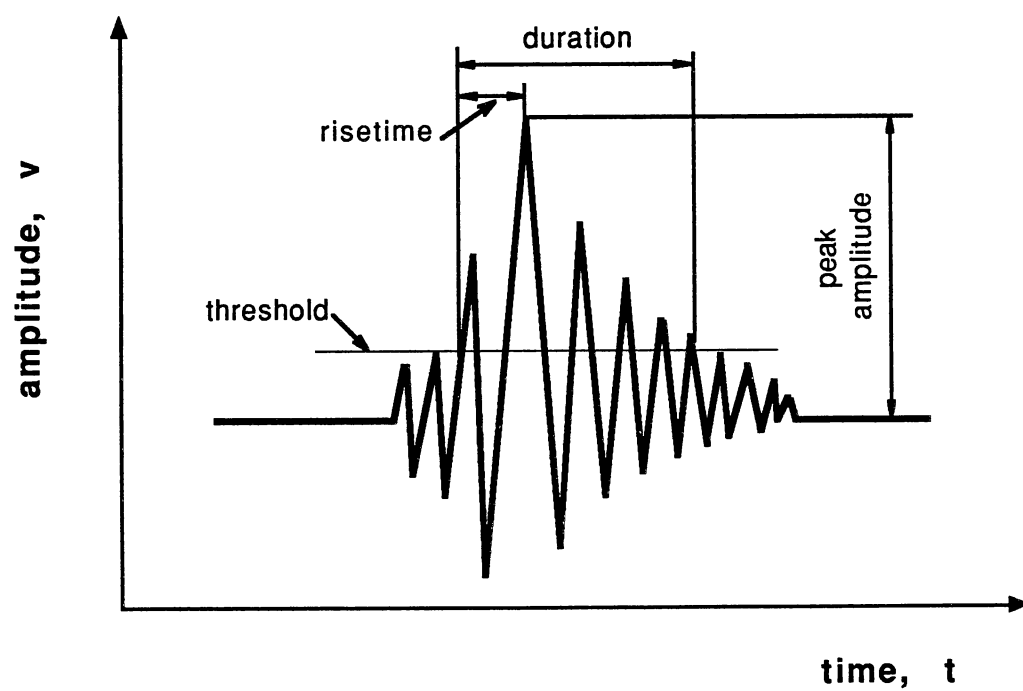


Figure 5. A Typical Acoustic Emission Signal From Metal Fatigue

propagation in some steel weldments are higher than those in their base steel.

As to the effect of the loading frequency on acoustic emission, Morton [68] studied AE signals from fatigue testing of aluminum 2024-T851 and magnesium EZ33A using load cycling frequencies of 1, 4, and 16 *Hz*, respectively. He concluded that the generic behavior of AE signals due to fatigue crack growth was insensitive to variations in the loading frequency. Similarly, Harris [69] reported that the load cycling frequency did not affect the acoustic emission signals from fatigue testing of aluminum 7075-T6 and 4140 steel when both high and low frequencies were used.

Signal Collection

During propagation, acoustic emission waves cause mechanical displacements at the surface of the material. These mechanical motions can be transferred into electrical signals through the acoustic emission sensors. This process is demonstrated in Fig. 6. The AE sensor is usually placed on the surface of the specimen. The interface between the sensor and the specimen is covered by some coupling substance. The electrical signal output of the sensor can be further processed using the AE instrumentation.

There are two major types of AE sensors: resonant type and non-resonant type. The non-resonant sensors are also called broad or flat frequency response sensors. The resonant sensors employ piezoelectric elements and are more sensitive than the non-resonant

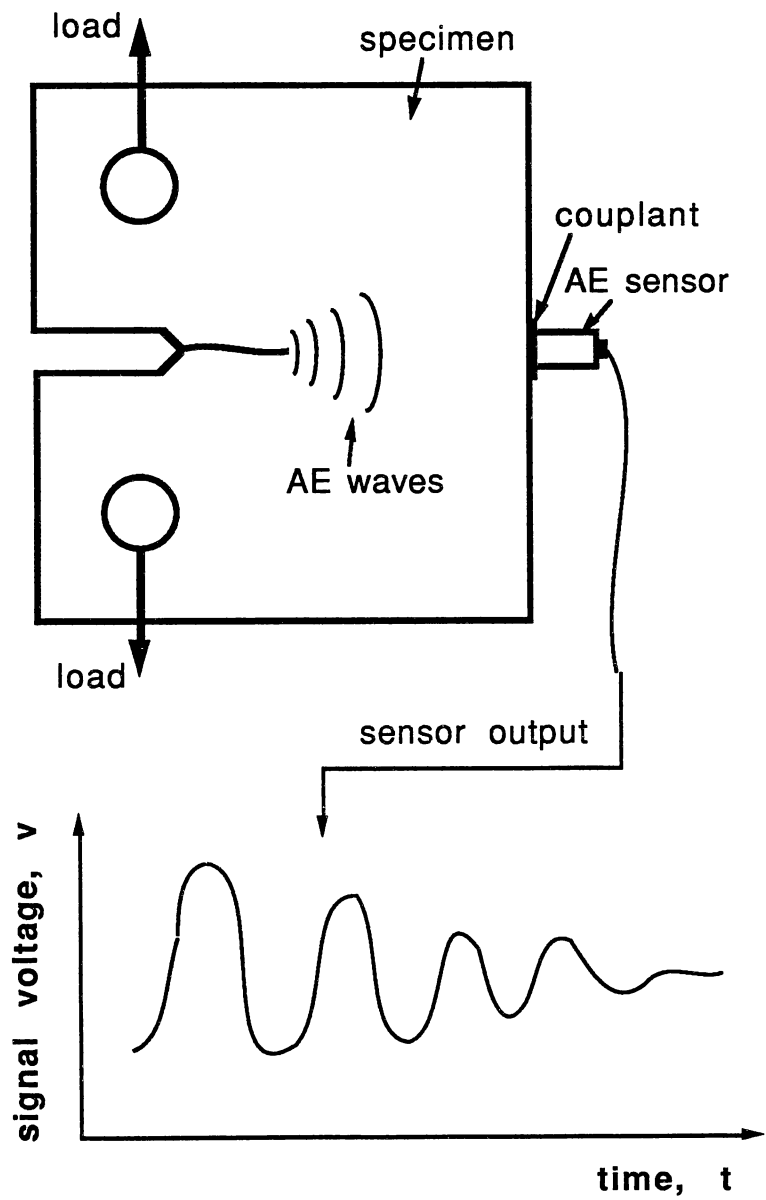


Figure 6. A Typical Set-Up for Acoustic Emission Sensing

type. This type of sensor typically detects acoustic emission signals in a frequency range centered at their resonant frequencies. Broadband sensors are mainly used to investigate the frequency spectra of the AE signals, where a wide frequency range is more important than a high sensitivity.

Acoustic emission signals have a broad frequency range from audible frequencies to above 1 *MHz* [65]. To determine the effect of the operating frequency range of the AE sensor on the acoustic emission measurement, several AE sensors of different frequency ranges were used to monitor acoustic emissions during fatigue crack propagation in aluminum 7075-T6 and 4140 steel [69]. The results showed no distinguishable, qualitative differences in AE signal data from the different sensors.

The primary function of the coupling substance is to eliminate any air gaps and ensure good contact between the sensor and the specimen. The major consideration regarding the selection of the couplant is that the coupling medium be viscous enough to effectively transmit the shear wave components of the acoustic emission signals.

The acoustic emission signal output from the sensors (before amplification) can vary from below 10 *mV* to above 1 *V*. Most AE signals from fatigue testing are at the lower end of this range [25]. Hence, the elimination of noise effects on the AE measurement is very critical to the success of acoustic emission sensing. There are basically two types of noise: mechanical noises and electrical noises [25, 67]. Mechanical noises come from the hydraulic system of the

fatigue testing machine, the machine surroundings, and the loading elements. They can be isolated to some extent by physical or electronic barriers. The electronic barriers include analog or digital filters which discriminate against noises in a particular frequency range. Electrical noises are mainly from the acoustic emission instrument, and their effects can be attenuated by filtering and setting appropriate values of some relevant parameters in the instrument, such as threshold and gain.

Signal attenuation due to geometric and material factors might also affect the detection of an acoustic emission source at a distance. Fortunately, it has been shown [65] that for metallic specimens up to 12 *in.* in size, the attenuation is negligible.

Signal Processing

The acoustic emission signal output at the sensor will be sent to a preamplifier and then to an acoustic emission instrument. The preamplifier usually has a 40 *dB*¹ or 60 *dB* gain and a built-in analog filter. The AE instrument may also have an amplifier with adjustable gains and a built-in analog filter. Therefore, the acoustic emission signal can be amplified at a desired magnification and the effects of background noises can be attenuated before the data acquisition (sampling).

¹The amplifier gain in *dB* is calculated as follows: $dB = 20 \log_{10} (\text{output}/\text{input})$. For example, a 40 *dB* gain means that the output is one hundred times the input.

The sampled signals can be recorded in time domain or frequency domain. In the time domain, the amplitude of the AE signal is expressed as a function of time. In the frequency domain, the signal amplitude is expressed as a function of frequency. The frequency domain data are calculated from the time domain data using the fast Fourier transformation (FFT) algorithm. This approach has been used to study the predominant frequencies of the AE signals from fatigue testing of welded beams [67]. It might also be used to identify the noise frequencies for filter design and noise attenuation purposes.

Several parameters which are frequently used to characterize the acoustic emission signals from fatigue testing can be extracted from the time domain data. They are event count, ring-down count, energy count, and amplitude of an event. The following is a brief description of each parameter.

Event Count. A complete burst signal of the acoustic emission above the threshold setting of the instrument is counted as an event. The signals below the threshold are ignored. The event count is the total number of events. Therefore, the event count depends very much upon the choice of the threshold. An appropriate threshold value is very critical. When the threshold is too high, some important events resulting from weak acoustic emission activities may be missed. When the threshold is too low, background noises may be counted as events by mistake. There is always a trade-off between the signal integrity and the noise attenuation. The event count provides information about the occurrence rate of the acoustic

emission activities. But it gives no weighing in favor of the intense emissions. This parameter is recommended for the case where the acoustic emission events have a statistically uniform intensity.

Ring-Down Count. The number of times that the acoustic emission curve crosses the threshold line (shown in Fig. 5) in an event is defined as the ring-down count. It is also called "count". This parameter qualitatively reflects the intensity of an event. Electronically, this is a very easy measurement and was the first to come into wide use [65]. Many researchers [21-23, 32, 70, 71] have made attempts to relate the ring-down count to fatigue damage.

Energy Count. The area under the envelope of the acoustic emission signal curve of an event is the energy count. The energy count is dependent on both the amplitude and the duration of the signal. It is a better representative of the intensity of an event than the ring-down count. This parameter has only recently become available in acoustic emission instruments due to the complex circuitry required [20, 65].

Amplitude. The amplitude of an event refers to the peak amplitude of the acoustic emission signal during the event. It was frequently used for studying fatigue damage in previous research [24]. It might also be used in combination with the count to measure the intensity of an event.

Methodology of CMOD, BFS, and Striation Measurements

Farfield Crack Opening Displacement

In recent years, crack closure has been recognized to play a dominant role in fatigue crack growth in metals [44, 54, 72-76]. There are four categories of measurement technique for crack closure: (1) global or thickness-averaging compliance techniques, (2) indirect thickness-averaging techniques, (3) surface techniques for measuring closure near the crack tip, and (4) techniques which measure closure in the specimen interior.

Two techniques from the first category, crack mouth opening displacement (CMOD) and back-face strain (BFS), are generally preferred. They provide reproducible and practical, global measurements of the average closure response, and are the most logical choices for standardization [77, 78, 79]. The BFS and CMOD are measured at locations far from the crack tip. Therefore, they are also called farfield crack opening displacements [80, 81]. Both techniques will be tried in this research.

Crack Mouth Opening Displacement. Crack mouth opening displacement is usually measured using a clip gage mounted across the notch mouth and located at the specimen edge [79, 82]. The stress intensity factor for crack opening, K_{op} , is determined graphically from the load-displacement curve illustrated in Fig. 7. In the figure, the crack is fully closed below point A, partially open along curve AB, and fully open above point B. Any point on curve

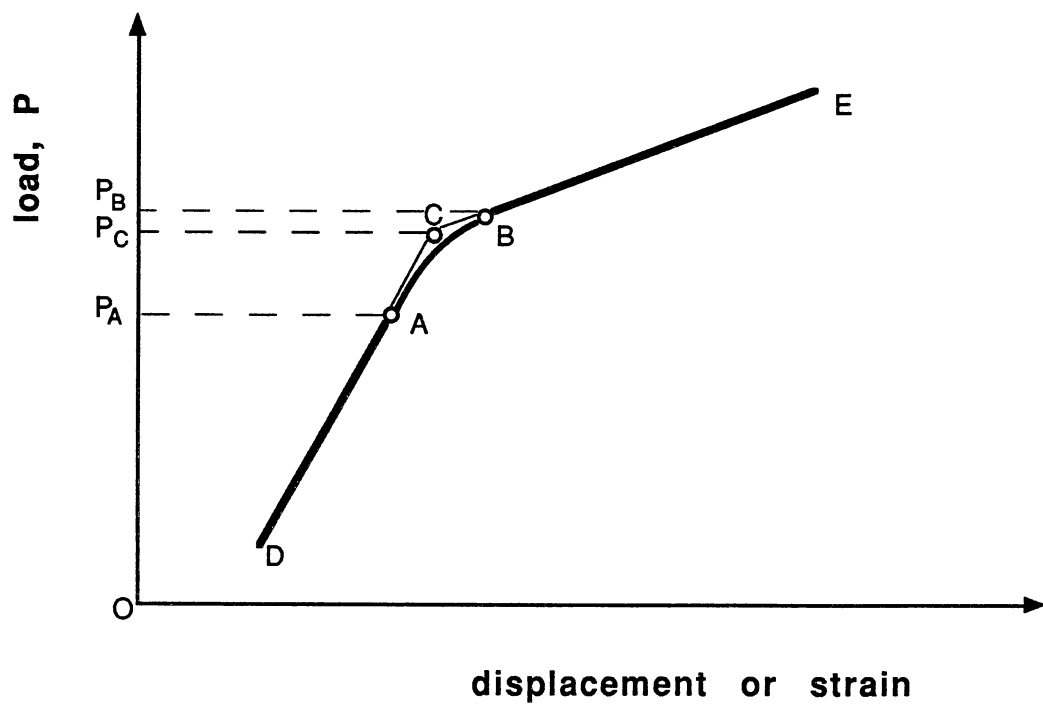


Figure 7. A Typical Load-Displacement Curve

AB could be used as a measurement of the opening load. However, it was reported [81] that the intersection of the extension lines of line AD and AE, point C, has a close relation to the $da/dN - \Delta K_{eff}$ data. Point C is typically used to determine the crack opening stress intensity factor [77, 78].

Back-Face Strain. The back-face strain is measured using a standard strain gage bonded to the back-face of a compact tension (CT) specimen. According to a study using finite element analysis [83], when a tensile load is applied to a CT specimen, the back-face strains are compressive instead of tensile, and the maximum magnitude strain occurs at the center of the specimen back face. So the optimum location of the strain gage would be the back-face center. The crack opening load is determined from the plot of load versus magnitude of the back-face strain, as shown in Fig. 7. The procedure is similar to that used in the CMOD measurement.

The BFS measurement technique is simple and inexpensive. It has been reported to be reliable and sensitive [77,83, 84]. This technique was developed later than the CMOD measurement technique.

Fatigue Striations

Under a scanning electron microscope, many small parallel lines can sometimes be observed on fatigue fracture surfaces. These lines are called fatigue striations. From fatigue testing of aluminum alloys, Forsyth and Ryder [85, 86] found that each striation represents the

incremental advance of the crack front as a result of one loading cycle. Other characteristics of the striation phenomenon are [11]:

1. It is material-dependent. For example, aluminum alloys usually have more visible striations than high-strength steels.
2. The presence of striations on fatigue fracture surfaces may not always be guaranteed due to metallurgical reasons and service conditions. The striations may be straight or curved, continuous or discontinuous.
3. The striations usually occur at intermediate stress intensity ranges (ΔK), which correspond to the second region in Fig. 4. At high ΔK levels, microvoid coalescence may occur. And at low ΔK levels, a cleavage-like faceted appearance may occur.

Although the striation phenomenon is rather complicated in nature, it has been used as a measure of fatigue crack increment [30, 43, 87, 88]. For example, with the aid of striation observation results, McBride [30] successfully correlated a crack advance of 20 μm in a 7075-T6 aluminum specimen with its acoustic emission signal. Hertzberg [87] found reasonable correlation at a given ΔK level between the growth rate macroscopically determined using a traveling microscope and the microscopic growth rate as measured using the striations, in 2024-T3 aluminum alloy.

The striation phenomenon has also been employed to study the fatigue damage under variable-amplitude loading conditions [89-91]. Striation spacings on fracture surfaces of aluminum 2024-T3, 7178-T6, and 7075-T6 have been related to specific cycles in variable-amplitude load-time histories. It was observed [90] that the

minimum striation spacing did not occur immediately after overloading, which indicates the delayed retardation. It was also noted [89] that a slightly expanded striation occurred following an overload, which could be the sign of overload acceleration. It is expected that SEM observation of striations will provide information on the overload effect in the present investigation.

CHAPTER III

EXPERIMENTAL INVESTIGATION

To study the overload effect and the threshold behavior of A588 steel from different aspects, this research employed a traveling microscope (TM), the acoustic emission technique, the farfield crack opening displacement techniques, and fatigue striation observations under a scanning electron microscope (SEM). The functional diagram of the experimental study is shown in Fig. 8. Figure 9 shows the major portion of the experimental setup. Specimens and their orientation, loading program, macrocrack growth measurement, acoustic emission signal acquisition, CMOD and BFS measurement, and fatigue striation observation will be discussed in this chapter.

Specimens and Their Orientation

Specimen Description

Two standard compact tension (CT) specimens of A588-80A steel were used in the present research. The CT specimens were chosen because of their availability and the possibility of utilizing some of their fatigue testing data from previous research [6, 82]. Both specimens were premachined according to the specifications of the American Society for Testing and Materials (ASTM) [61]. Their

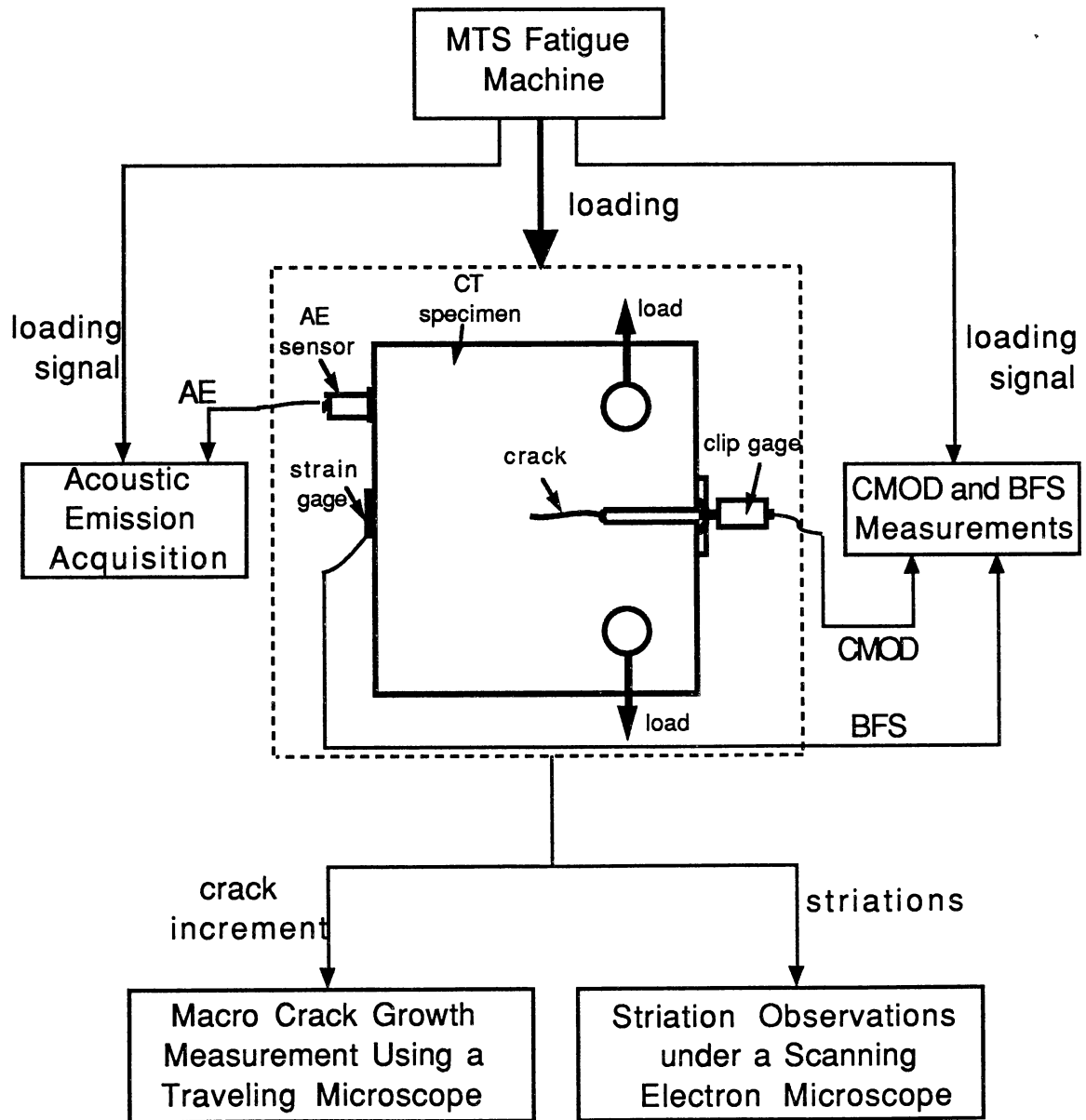


Figure 8. The Function Diagram of the Experimental Study

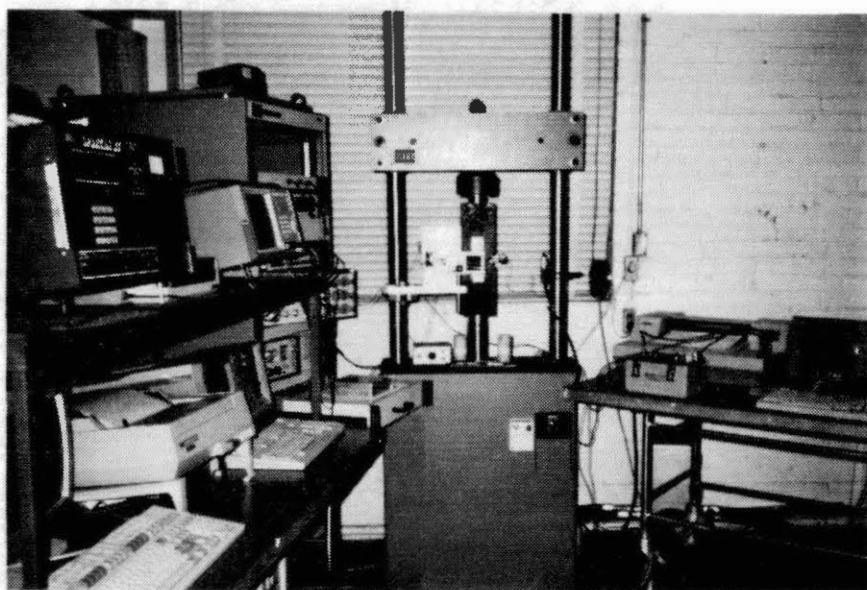


Figure 9. A View of the Experimental Setup

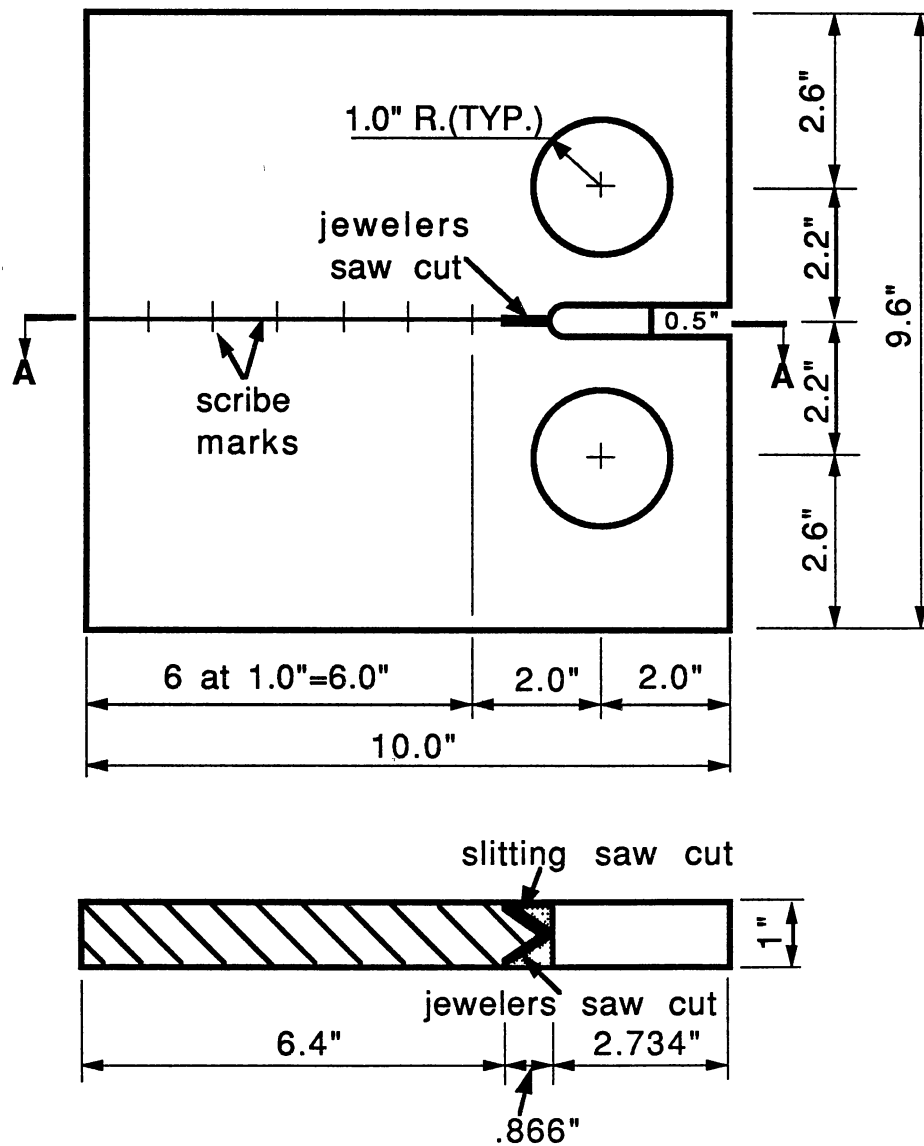
size is shown in Fig. 10. The width of the specimens is greater than that used in other studies [80, 92]. A wider specimen leads to a more accurate estimation of the stress intensity factor, since the stress intensity factor is dependent on the ratio of the measured crack length to specimen width. The notch on the specimens as well as the loading grips and pins used were also designed according to ASTM specifications. Their sizes are dependent upon the size and shape of the specimens.

A588-80A steel is a structural steel used for highway bridges. Chemical compositions are shown in Table 1 [6]. Table 2 [6] lists mechanical properties in directions both longitudinal and transverse to the rolling direction of the material.

On both specimens, a horizontal line and several vertical lines were scribed along the path of crack growth as shown in Fig. 10. The horizontal line represents the idealized plane of crack growth. It was used as a base line to identify any deviation of the crack path. The ASTM specifications stipulate that if at any point during testing, the crack path deviates outside an envelope that encompasses the material between two planes oriented at $\pm 5^\circ$ from the idealized plane of crack growth and intersecting at the axis of loading, the data are invalid [61]. All vertical lines are references for crack length measurement.

Specimen Orientation

The orientation of a specimen in relation to loading direction is



Sect. A-A

Figure 10. Dimensions of the Compact Tension Specimens Used

TABLE 1
CHEMICAL COMPOSITION OF THE CT SPECIMENS [6]

Source	Chemical Composition, %										
	C	Mn	P	S	Si	Ni	Cu	Cr	Mo	V	Al
Mill Test	0.13	1.02	.015	.017	0.48	0.35	0.22	0.57	-	.050	-
Laboratory	0.14	0.99	.014	.031	0.37	0.34	0.21	0.56	0.01	.034	.024

TABLE 2
MECHANICAL PROPERTIES OF THE CT SPECIMENS [6]

	Yield Stress (ksi)		Ultimate Stress (ksi)		Elongation (%)		Reduction of Area (%)	
	L ^{*1}	T ^{*2}	L	T	L	T	L	T
Mill Test ^{*3}	63.2		90.8		18.5 ^{*4}		-	
Present Work	50.0 ^{*5}	49.4 ^{*5}	82.9	82.5	33.0 ^{*6}	27.0 ^{*6}	67.5	47.0

¹L = longitudinal to rolling direction.

²T = transverse to rolling direction.

³Orientation unknown, load rate unknown.

⁴Gage length of 8 in.

⁵Static yield stress.

⁶Gage length of 2 in.

an important factor governing the fracture toughness of the specimen [11, 93]. Orientation also influences the relationship between crack growth rate and stress intensity range [6]. Several possible orientations of the standard specimens are shown in Fig. 11. The code system for the specimen orientation consists of two hyphenated letters, with the first representing the loading direction and the second representing the crack growth direction. The letter "L" stands for the longitudinal (rolling or extrusion) direction, "S" for the thickness direction, and "T" for the transverse direction.

It was previously known that the orientation of the specimens used in this research is either L-T or T-L. Since grains and inclusions in a steel plate elongate along its longitudinal direction, a metallurgy test was carried out to determine the "L" direction of the specimens. The result showed that the specimens are in the L-T orientation as illustrated by the shadowed specimen in Fig. 11.

Loading Program

Loading Spectra

Four groups of loading spectra were adopted in this research. The first three groups are isolated overload spectra. The last group is a constant-amplitude loading spectrum. Table 3 is a summary of all loading spectra used. Details of each loading group and the objectives it served are described below.

The first loading group has six isolated overload spectra. They share the same overload cycles and minor cycles. Their stress

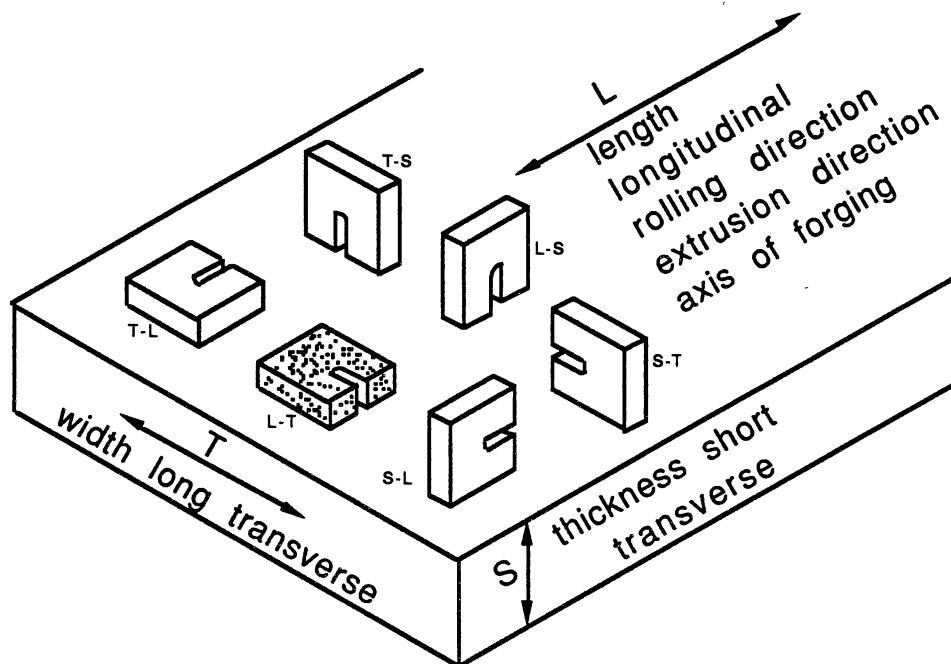


Figure 11. Orientations of CT Specimens

TABLE 3.3
A SUMMARY OF THE LOADING SPECTRA

Parameters Loading Group		Overload Cycles				Minor Cycles				R _Δ	n
		ΔK _o (ksi√in)	K _{o,max} (ksi√in)	K _{o,min} (ksi√in)	R _o	ΔK _m (ksi√in)	K _{m,max} (ksi√in)	K _{m,min} (ksi√in)	R _m		
1		15	16.7	1.67	0.1	4.5	6.17	1.67	0.3	0.3	0, 4, 9, 49, 99, 999
2		45	64.3	19.3	0.3	13.5	32.8	19.3	0.6	0.3	9, 49
3	top	15	16.7	1.67	0.1	4.5	16.7	12.2	0.7	0.3	9
	middle						11.5	6.92	0.6		
	bottom						6.17	1.67	0.3		
4		constant-amplitude loading ΔK, K _{max} , K _{min} = 8.5, 9.44, 0.944(ksi√in) and R = 0.1									

intensity factor versus time histories are illustrated in Fig. 12. The stress range ratio or stress intensity range ratio of the minor cycles to the overload cycles, R_{Δ} , was chosen to be 0.3. As compared to the R_{Δ} values (0.4 or 0.5) used in other overload studies [36, 41, 94], 0.3 is relatively small and is expected to give a more significant overload effect. The stress ratio or stress intensity ratio of the overload cycles, R_o , is 0.1, which is the same as that adopted in Refs. [6, 82] for data comparison. The stress intensity range of the minor cycles was chosen to be $4.5 \text{ ksi}\sqrt{\text{in.}}$. It is below the threshold level of $4.93 \text{ ksi}\sqrt{\text{in.}}$, calculated using the Barsom formula in Eq. (2.22). The only difference between the six spectra in this group is the number of minor cycles between two adjacent overloads, n . Values for n were chosen to be 0, 4, 9, 49, 99, and 999, respectively. This loading group was employed to study the transition from overload retardation to acceleration as well as the threshold behavior under variable-amplitude loading.

The second group of loadings was designed to make striations and crack opening displacement more visible by increasing the stress intensity factor and the stress intensity range. Increasing the stress intensity factor leads to a larger plastic zone ahead of the crack tip and more visible crack opening displacement. Increasing the stress intensity factor and the stress intensity range leads to a wider striation spacing. The stress intensity range of the minor cycles and the stress ratio of the overloads were chosen to be $13.5 \text{ ksi}\sqrt{\text{in.}}$ and 0.3 instead of $4.5 \text{ ksi}\sqrt{\text{in.}}$ and 0.1. This higher stress ratio is also expected to reduce the abrasion between the fracture surfaces and

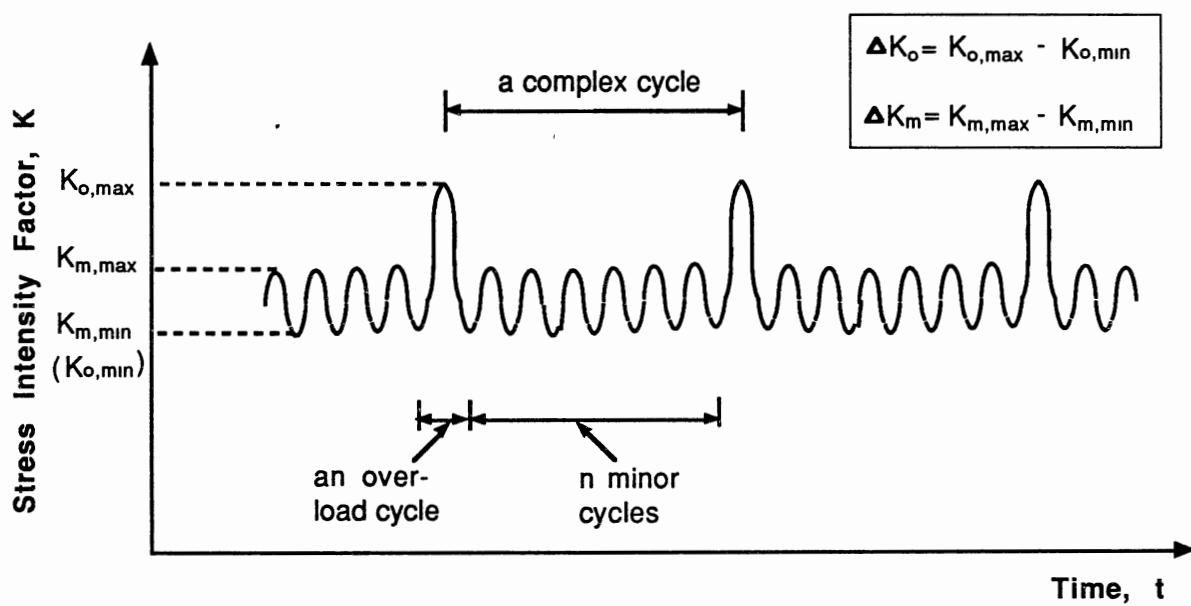


Figure 12. An Example of the Overload Spectra

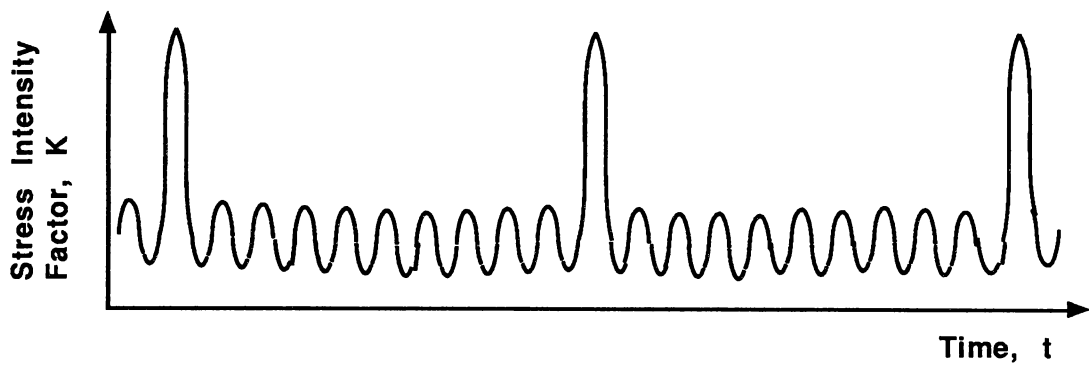
protect the striation profiles. The R_{Δ} value remains 0.3. This group has two isolated overload spectra, one with $n = 9$ and the other with $n = 49$.

In the first two groups of loading, the minor and overload cycles have the same minimum stress intensity factor. Practical load-time histories usually have minor cycles with different minimum stresses. To study the effect of varying minimum stress, tests were conducted in which the stress intensity range of minor cycles was held constant but the minimum stress intensity factor varied. This third loading group has three isolated overload spectra similar to the spectrum with $n = 9$ in the first loading group, except that the stress ratio of the minor cycles, R_m , in each spectrum has a different value. The relative position of the minor cycles with respect to the overload cycles in each loading spectrum is shown in Fig. 13. In the following discussion, the effect studied in this loading group will be referred to as the minor cycle stress ratio effect or the R_m effect.

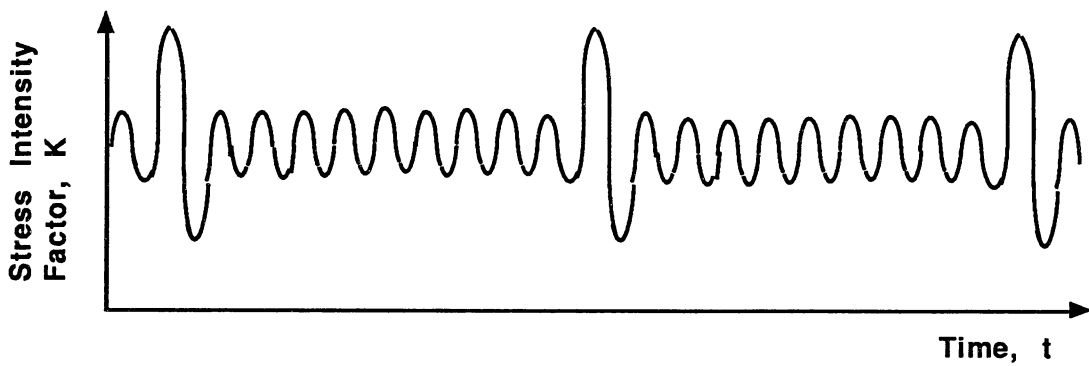
For the above three groups of loading, each loading spectrum was applied at a different crack length. Thus, the effect of the crack length was a concern. A final loading group was designed to study the effect of crack length. The last loading group has a constant stress intensity range of $8.5 \text{ ksi}\sqrt{\text{in.}}$ and a stress ratio of 0.1.

Loading Procedure

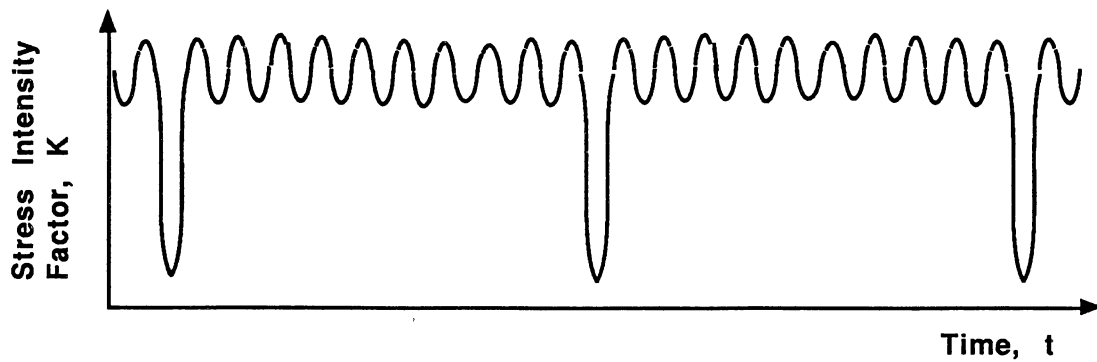
The loading system used is an MTS 810 material testing system. It includes an MTS 318.10 fatigue loading frame with a 22 kip,



(a) with minor cycles at the bottom level of overload cycles



(b) with minor cycles at the middle level of overload cycles



(c) with minor cycles at the top level of overload cycles

Figure 13. Loading Spectra With Different Minor Cycle Stress Ratios

model 204.22c-05 hydraulic actuator, and a loading console consisting of an MTS 430 digital indicator, an MTS 410 digital function generator, an MTS 442 controller, and an MTS 436 control unit. It was basically designed for constant-amplitude loading. The loading range can be adjusted through two channels. An adjustable cyclic impulsor was added to one of the channels to provide the ability to produce intermittent overloads.

The minimum level of minor cycles with respect to overload cycles was set with the digital function generator. Referring to Fig. 13, the haversine, sine, and invert-haversine functions of the loading system were employed for cases (a), (b), and (c), respectively.

The loading process was continuously monitored with a built-in peak detector. When the loading frequency was above 10 *Hz*, the last digit of the peak detector showed a significant fluctuation, which indicated the deterioration of the loading precision. When the loading frequency was below 10 *Hz*, the fluctuations of the maximum loading and the loading range were found to be within the limit of $\pm 2\%$ stipulated by ASTM specifications [61]. Since a high loading frequency results in a short testing time, the loading frequencies in all tests conducted in this research were chosen to be 10 *Hz*. When only the crack length was being measured, the loading frequency was reduced to 1 *Hz* to enable location of crack tip with less difficulty. The number of cycles of frequency 1 *Hz* was insignificant as compared to that of frequency 10 *Hz*. In general, it is considered that a fatigue test in a noncorrosive environment can be run at almost any frequency without affecting the results [34, 95].

Prior to formal fatigue tests, both specimens were precracked under cyclic loadings to minimize the geometric effect of the machined starter notch and provide a sharpened fatigue crack of adequate size and straightness. Precracking followed the procedure suggested by the ASTM specifications [61]. The ratio of maximum loading to minimum loading was chosen to be 0.1, the same as that in the fourth loading group. The maximum stress intensity factor was set to be higher than that in the formal tests, because a crack needed to be initiated from the machined notch. The minimum fatigue precrack length of both specimens was chosen to be 2 *in.* for reasons to be discussed in the section on ΔK precision. This choice also meets the ASTM stipulation [61] that the fatigue precrack length should be larger than or equal to the greater of one-tenth of the specimen thickness and the notch width.

The loading range was stepped down gradually during precracking until it reached the loading level of the formal test. The reduction of the loading range per step was 20%. To minimize the transient effect of the step change in loading, it was ensured that the crack length increment in each step was larger than three times the diameter of the plastic zone resulting from a loading cycle in the previous step. The diameter, d_p , of a plastic zone resulting from a loading cycle with maximum stress intensity factor K_{max} can be calculated as follows,

$$d_p = \frac{1}{\pi} \left(\frac{K_{max}}{\sigma_y} \right)^2 \quad (3.1)$$

For two adjacent formal tests, the above concept of step-down loading was also used to eliminate the interaction between two loading spectra. If the previous loading spectrum had any loading cycle higher than the loading cycles in the following spectrum, a step-down loading spectrum was added at the end of the previous test. The loading range stepped down at a speed of 20% reduction per step until it reached the loading level of the following test. The minimum crack increment during each step was three times the diameter of the plastic zone resulting from the last overload cycle in the previous test. The diameter of the plastic zone can be calculated using Eq. (3.1). A typical sequence of formal fatigue tests conducted is: the fourth loading group \rightarrow a loading spectrum from one of the first three loading groups \rightarrow a step-down loading spectrum \rightarrow the fourth loading group \rightarrow

ΔK Precision

When the loading range, ΔP , is kept constant, the stress intensity range, ΔK , increases as the crack length increases. To conduct fatigue tests with constant ΔK values, load should be shed while the crack grows. The crack increment between two adjacent load sheddings plays a dominant role in determining the precision of the constant- ΔK tests. The smaller the crack increment between two sheddings, the less the deviation of the actual ΔK from the desired constant value. But shedding frequently is unfavorable because of the time and effort required for each shedding. It is

preferred to use the maximum possible crack increment as long as the ΔK precision is met. However, no documented work regarding the precision of ΔK during a constant- ΔK test was found in the literature. An equation for the ΔK precision associated with CT specimens will be derived below.

According to the ASTM specifications [61], the stress intensity range of a CT specimen can be calculated as follows,

$$\Delta K = \frac{\Delta P}{B\sqrt{W}} \frac{(2+\alpha)}{(1-\alpha)^{3/2}} H(\alpha), \quad \alpha \geq 0.2 \quad (3.2)$$

where

$$H(\alpha) = 0.886 + 4.64\alpha - 13.32\alpha^2 + 14.72\alpha^3 - 5.6\alpha^4 \quad (3.3)$$

B is the specimen thickness, W is the specimen width measured from the centerline of the loading pins to the back surface of the specimen, and α is the ratio of the crack length, a , to the specimen width. The parameter a is measured from the centerline of the loading pins to the crack tip.

From Eqs. (3.2) and (3.3), the partial derivative of ΔK with respect to the crack length can be derived as follows,

$$\begin{aligned} \frac{\partial(\Delta K)}{\partial a} = & \frac{\Delta P}{B\sqrt{W} (1-\alpha)^3} \left\{ (1-\alpha)^{3/2} \left[\frac{1}{W} H(\alpha) + (2+\alpha) H'(\alpha) \frac{1}{W} \right] \right. \\ & \left. + \frac{1}{W} \frac{3}{2} (1-\alpha)^{1/2} (2+\alpha) H(\alpha) \right\} \end{aligned} \quad (3.4)$$

where,

$$H'(\alpha) = \frac{d(H(\alpha))}{d\alpha} = 4.64 - 26.64\alpha + 44.16\alpha^2 - 22.4\alpha^3 \quad (3.5)$$

Equation (3.4) can be simplified as,

$$\frac{\partial(\Delta K)}{\partial a} = \frac{\Delta P}{B W^{3/2}} \frac{Q(\alpha)}{(1-\alpha)^{5/2}} \quad (3.6)$$

where

$$Q(\alpha) = 12.824 - 38.917\alpha + 59.36\alpha^2 - 10.1\alpha^3 - 36.8\alpha^4 + 19.6\alpha^5 \quad (3.7)$$

From Eqs. (3.2) and (3.6), the fractional change rate of ΔK with respect to the crack length is,

$$\frac{1}{\Delta K} \frac{\partial(\Delta K)}{\partial a} = \frac{1}{W(1-\alpha)(2+\alpha)} \frac{Q(\alpha)}{H(\alpha)} \quad (3.8)$$

If the maximum crack increment between two load sheddings is Δa_{max} , the ΔK fluctuation denoted as ξ is,

$$\begin{aligned} \xi &= \left(\frac{1}{\Delta K} \frac{\partial(\Delta K)}{\partial a} \right) (\Delta a_{max}) \times 100\% \\ &= \frac{\Delta a_{max}}{W(1-\alpha)(2+\alpha)} \frac{Q(\alpha)}{H(\alpha)} \times 100\% \end{aligned} \quad (3.9)$$

where $Q(\alpha)$ and $H(\alpha)$ can be calculated using Eqs. (3.3) and (3.7).

In the present research, the specimen width is 8 *in.* Thus the precrack length should not be smaller than 1.6 *in.* in order to utilize Eq. (3.2). The maximum crack increment between sheddings was 0.046 *in.* for $0.25 \leq \alpha < 0.53$ and 0.035 *in.* for $0.53 \leq \alpha < 0.57$. No additional tests were carried out on the specimens when their crack length was larger than 4.53 *in.* (i.e., $\alpha > 0.566$). The ξ - α plots for $W = 8$ *in.* and $\Delta a_{max} = 0.046, 0.035$ *in.*, obtained from Eq. (3.9), are shown in Fig. 14. It is clear that the fluctuation of ΔK is within 2%, a suggested value for loading precision by ASTM [61]. Therefore, the ΔK precision of the constant- ΔK tests in current research is reasonable.

In previous research, it was common that the crack increment between sheddings was selected without proper justification [65, 68, 91, 92]. This is alarming because the ΔK fluctuation could be unexpectedly large with a random choice of the crack increment as the crack becomes longer and longer. As an example, the ΔK precision in Ref. [68] is discussed below according to Eq. (3.9). In that study, the specimen width was 2 *in.*, and the crack increment between sheddings was 0.05 *in.* The ξ - α plot from Eq. (3.9) is shown in f. 15. It is noted that when the crack length is 0.4 *in.* (i.e., $\alpha = 0.2$), the ΔK fluctuation is already higher than 2%, meaning that the ΔK fluctuation will be larger than 2% for the entire test.

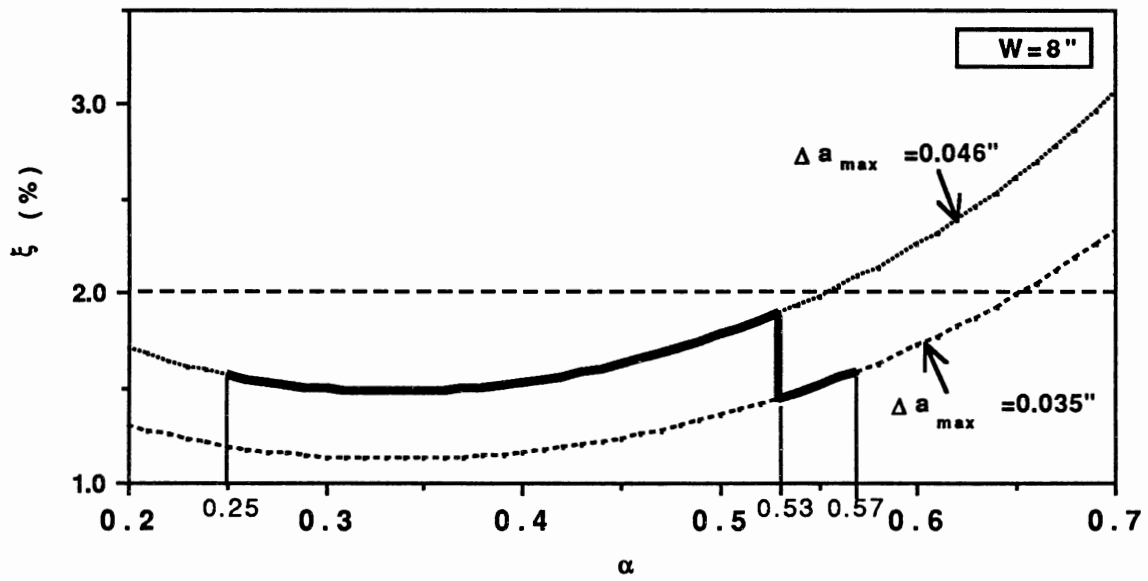


Figure 14. The ΔK Precision Curves for CT Specimens when $W = 8 \text{ in.}$, $\Delta a_{max} = 0.035, 0.046 \text{ in.}$

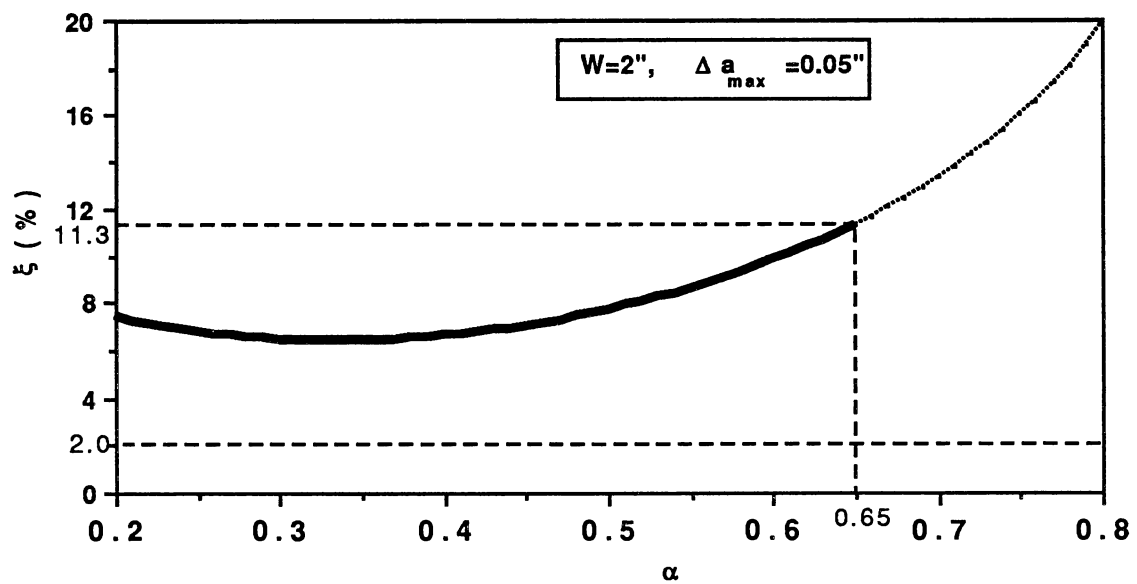


Figure 15. The ΔK Precision Curves for CT Specimens when $W = 2 \text{ in.}$, $\Delta a_{max} = 0.05 \text{ in.}$

Unfortunately, a crack length as large as 1.25 *in.* (i.e., $\alpha = 0.65$) was reported in Ref.[68], which means that the ΔK fluctuation in a constant test was as high as 11% in that study. It is very important to choose an appropriate crack increment between load sheddings.

Macrocrack Growth Measurement

Apparatus

A Gaertner traveling microscope with 32X magnification was used to measure macrocrack growth. Lateral movement of the microscope could be measured to a precision of 0.00005 *in.* A specially designed two-piece fixture was used to connect the microscope to the loading frame as shown in Fig. 16.

To determine the accuracy of the crack length measurement, a precision test was carried out at a loading frequency of 1 *Hz*, which simulated the actual measuring condition. For this test, the minimum and maximum stress intensity factors were set at 19.3 and 32.8 *ksi* $\sqrt{\text{in.}}$. At the identical crack tip position, the crack length was measured fifteen times. The fifteen readings are shown in Table 4. The standard deviation of these data is 0.00067 *in.* According to the ASTM specifications, 0.00067 *in.* is an estimate of the precision of the crack length measurement.

Procedure

In each test, four to six crack tip positions were measured so as

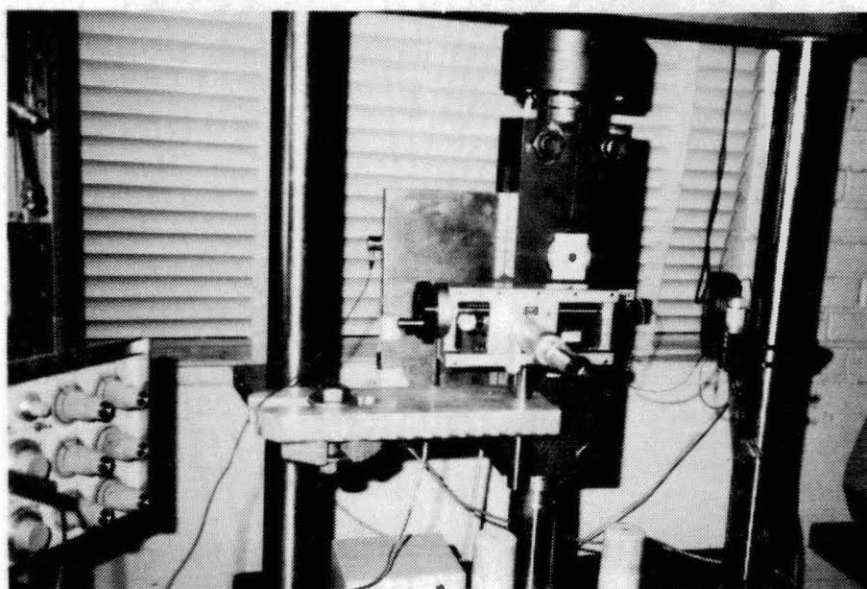


Figure 16. The Traveling Microscope Fixture

TABLE 4
CRACK LENGTH DATA FROM THE
PRECISION TEST

Measurement No.	Crack Length Measured (in)
1	2.77175
2	2.77430
3	2.77260
4	2.77260
5	2.77195
6	2.77230
7	2.77245
8	2.77140
9	2.77190
10	2.77240
11	2.77185
12	2.77220
13	2.77225
14	2.77160
15	2.77200
Average = 2.77224 in.	
Standard Deviation= 0.00067 in.	

to obtain three to five crack growth values for each loading spectrum. The availability of multiple data can minimize any misleading effect of random errors in the experimental data. While measuring crack length, the loading frequency was decreased to 1 Hz, and the vertical crosshair on the microscope was used to locate the crack tip. The difference between two consecutive position measurements is the crack growth increment resulting from the corresponding loading cycles. The ratio of the crack increment to the number of the loading cycles applied is the crack growth rate.

In the variable-amplitude loading situation, it is usually more difficult to locate the crack tip than in the constant-amplitude loading situation. For convenience, the microscope crosshair was first moved close to the tip during minor cycles. When an overload cycle came, the crack tip could be located with a fine adjustment.

Due to the limited measuring precision, the crack increment between two measurements should be sufficiently large to ensure the accuracy of the crack increment measured. In the ASTM specifications [61], it is suggested that the crack increment to be measured be larger than or equal to ten times the precision of the measuring system. In this study, the minimum crack increment between measurements was selected to be 0.018 in., which is about twenty-seven times the crack length measurement precision of 0.00067 in. To simplify the test procedure, load sheddings were introduced immediately after the crack tip position measurements. The process of loading, measuring, and shedding are summarized in Tables 5 and 6.

Acoustic Emission Signal Acquisition

Instrumentation

The major elements of the AE measurement system used are a transducer, a preamplifier, an AE analyser, a digital oscilloscope, and two microcomputers. Figure 17 is the signal flow chart of this system. The instrument console is shown in Fig. 18.

Transducers and Preamplifiers Two piezoelectric transducers were used. One is a broadband transducer of model PAC-WD772. It has a relatively flat frequency response curve between 100 *kHz* and 1 *MHz*, and was used with an all-pass preamplifier of model PAC 1220A-BP-SYS to identify the frequency range of noise. The other is a PAC-R15 resonant transducer with a resonant frequency of 150 *kHz*. It has a satisfactory frequency response from 100 *kHz* to 450 *kHz*, and was used together with a Dunegan 1801 preamplifier in the formal fatigue tests. The preamplifier has a high-pass filter with a corner or cut-off frequency of 50 *kHz*. In other words, ideally, only signals of frequencies higher than 50 *kHz* can pass through the preamplifier. The diameter of both transducers is one half inch. The gain of both preamplifiers is 40 *dB*. The coupling material is a hot glue which provides a firm contact between the transducers and the specimens and is removable.

AE analyser The AE analyser is a PAC 8000 SPARTAN-AT system. It provides multiple signal processing functions such as

TABLE 5
SUMMARY OF THE LOADING, MEASURING, AND
SHEDDING PROCESS (SPECIMEN TH1)

Crack Length a (in.)	Loading Spectrum		Loading Data in <i>kips</i>			
	Group No.	n	Overload Cycles		Minor Cycles	
			P _{o,max}	P _{o,min}	P _{m,max}	P _{m,min}
2.86965-2.89720	4				4.04	0.40
2.89720-2.93085					4.02	0.40
2.93085-2.95130					4.00	0.40
2.95130-2.98675	1	99	7.02	0.70	2.60	0.70
2.98675-3.02365			6.94	0.70	2.58	0.70
3.02365-3.06620			6.86	0.68	2.54	0.68
3.14040-3.16975	4				3.70	0.38
3.16975-3.19395					3.68	0.36
3.19395-3.22465					3.66	0.36
3.22465-3.24530	1	9	6.42	0.64	4.76	0.64
3.24530-3.26570			6.36	0.64	2.36	0.64
3.26570-3.28375			6.34	0.64	2.34	0.64
3.37330-3.39820	4				3.44	0.34
3.39820-3.43020					3.42	0.34
3.43020-3.45065					3.38	0.34
3.45065-3.47795	1	4	5.92	0.60	2.20	0.60
3.47795-3.49975			5.88	0.58	2.18	0.58
3.49975-3.52500			5.84	0.58	2.16	0.58
3.59035-3.61230	4				3.18	0.32
3.61230-3.63305					3.18	0.32
3.63305-3.66695					3.18	0.32
3.66695-3.69000	1	49	5.50	0.56	2.04	0.56
3.69000-3.71705			5.46	0.54	2.02	0.54
3.71705-3.74730			5.40	0.54	2.00	0.54

TABLE 5 (CONTINUED)

Crack Length a (in.)	Loading Spectrum		Loading Data in kips			
	Group No.	n	Overload Cycles		Minor Cycles	
			P _{o,max}	P _{o,min}	P _{m,max}	P _{m,min}
3.74730-3.78040	1	49	5.34	0.54	1.98	0.54
3.78040-3.80965			5.28	0.52	1.96	0.52
3.95085-3.97885	4				2.80	0.28
3.97885-4.00790					2.78	0.28
4.00790	2	49	18.76	5.64	9.58	5.64
4.10895-4.13865			17.96	5.34	9.16	5.38
4.13865-4.16140			17.74	5.32	9.06	5.32
4.16140-4.18200			17.58	5.28	8.96	5.28
4.18200-4.20790			17.44	5.22	8.90	5.22
4.20790-4.23675			17.26	5.18	8.80	5.18
4.23675-4.25770			17.04	5.12	8.70	5.12
4.25770-4.28655			16.90	5.08	8.63	5.08
4.28655-4.31030			16.70	5.00	8.52	5.00
4.31030-4.33710			16.56	4.96	8.44	4.96
4.33710-4.35880			16.34	4.90	8.34	4.90
4.35880-4.38175			16.20	4.86	8.26	4.86
4.38175-4.40495			16.06	4.82	8.20	4.82
4.40495-4.42865			15.92	4.78	8.10	4.78
4.42865-4.45195			15.72	4.72	8.02	4.72
4.45195-4.47320			15.56	4.66	7.94	4.66
4.47320-4.50400			15.42	4.62	7.86	4.62
4.50400-4.52795			15.22	4.56	7.76	4.56

TABLE 6
SUMMARY OF THE LOADING, MEASURING, AND
SHEDDING PROCESS (SPECIMEN TH2)

Crack Length a (in.)	Loading Spectrum		Loading Data in <i>kips</i>			
	Group No.	n	Overload Cycles		Minor Cycles	
			P _{o,max}	P _{o,min}	P _{m,max}	P _{m,min}
2.66925-2.69445	4				4.34	0.44
2.69445-2.71960					4.30	0.44
2.76860-2.80105	1	49	7.42	0.74	2.74	0.74
2.80105-2.82045			7.34	0.74	2.72	0.74
2.82045-2.84450			7.30	0.74	2.72	0.74
2.84450-2.86850			7.24	0.72	2.68	0.72
2.86850-2.90020			7.18	0.72	2.66	0.72
3.00745-3.02795	4				3.90	0.40
3.00745-3.02795					3.86	0.38
3.05455-3.07660	1	0	6.78	0.68		
3.07660-3.09890			6.72	0.68		
3.09890-3.12745			6.66	0.66		
3.12745-3.14990			6.60	0.66		
3.14990-3.16995			6.56	0.66		
3.26810-3.29375	4				3.58	0.36
3.29375-3.31880					3.54	0.36
3.31880-3.35080	3 (top)	9	6.20	0.62	6.20	4.52
3.35080-3.37920			6.14	0.62	6.14	4.48
3.37920-3.41145			6.08	0.60	6.08	4.44
3.41145-3.43960			6.00	0.60	6.00	4.38
3.43960-3.45960			5.94	0.60	5.94	4.34
3.56680-3.58725	4				3.22	0.32

TABLE 6 (CONTINUED)

Crack Length a (in.)	Loading Spectrum		Loading Data in <i>kips</i>			
	Group No.	n	Overload Cycles		Minor Cycles	
			P _{o,max}	P _{o,min}	P _{m,max}	P _{m,min}
3.58725-3.61005	4				3.20	0.32
3.61005-3.64490	3 (middle)	9	5.60	0.56	3.84	2.32
3.64490-3.67580			5.54	0.56	3.80	2.30
3.67580-3.69610			5.48	0.54	3.76	2.28
3.69610-3.71705			5.44	0.54	3.72	2.26
3.81240-3.83900	4				2.96	0.30
3.83900-3.86220					2.94	0.30
3.86220-3.89230	3 (bottom)	9	5.12	0.52	1.90	0.52
3.89230-3.91415			5.06	0.50	1.84	0.50
3.91415-3.93545			5.02	0.50	1.86	0.50
3.93545-3.96060			4.98	0.50	1.84	0.50
3.96060-3.98265			4.94	0.50	1.82	0.50
4.08315-4.10895	4				2.66	0.26
4.10895-4.13110					2.64	0.26
4.13110-4.15495	1	999	4.62	0.46	1.70	0.46
4.15495-4.17790			4.56	0.46	1.68	0.46
4.17790-4.22335			4.52	0.46	1.68	0.46
4.22335-4.25195			4.44	0.44	1.64	0.44
4.25195-4.28695			4.39	0.44	1.62	0.44
4.44135-4.47310	4				2.30	0.24
4.47310-4.50100					2.26	0.22
4.50100	2	9	12.66	4.44	7.64	4.44

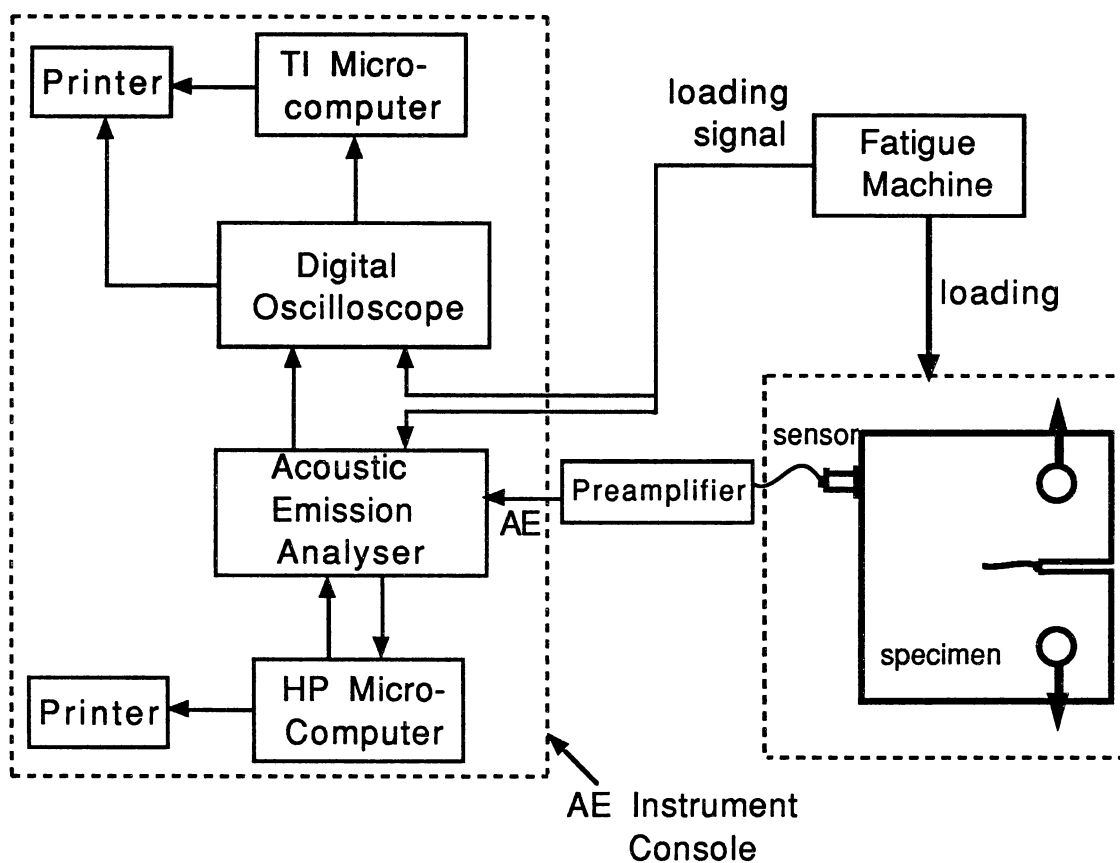


Figure 17. The Flow Chart of Acoustic Emission Signal Acquisition



Figure 18. The Acoustic Emission Instrument Console

system. It provides multiple signal processing functions such as measurement, storage, display, and analysis. Its core elements are Independent Channel Controllers (ICCs), which are two-channel computerized analog boards with linear and log frequency responses from 1.2 *kHz* to 1.2 *MHz*. Two types of signals can be used as the input to this system. One type is an AE signal, the other is a parametric signals such as a loading signals. A parameter called "threshold" is used as a criterion to determine the occurrence of an event. The amplitude, count, energy, time of occurrence, and corresponding loading of each event can be recorded and displayed on the screen. The system also provides other types of output, such as time-domain output and event output.

The SPARTAN-AT analyser is interfaced with an HP Vectra RS/20 microcomputer. The microcomputer monitors the analyser through a provided software package called "SPARTAN-AT.INI." Most of the instrumental operations, such as setting parameters, recording data, and starting or interrupting signal acquisition, can be carried out using the microcomputer. The output data from the analyser can be stored on floppy disks through the microcomputer.

Digital Oscilloscope A digital oscilloscope, model HP54501A, with a sampling frequency of 10 *MHz* was used to acquire, store, and display AE data. According to the sampling theorem [96], the maximum signal frequency below which aliasing due to sampling can be avoided is equal to one-half of the sampling frequency. Therefore, signals with frequencies ranging to 5 *MHz* can be

monitored without distortion using the oscilloscope. During fatigue tests, the time-domain output and event output of the analyser as well as the loading signal were connected to the input channels of the oscilloscope. The time-domain signal is the amplitude-time history of the AE signal, and the event signal consists of positive pulses with each pulse representing the occurrence of an AE signal. The loading signal was used as a reference to observe any correlation between the AE signals and the loading cycles. To dump the AE data in the oscilloscope memory to floppy disks, a TI microcomputer was connected to the oscilloscope via its HP-IB connector.

Parameter Setting

Both the SPARTAN-AT AE analyser and the HP 54501 digital oscilloscope are comprehensive instruments which have operating parameters to be determined by the user. The selection of several critical parameters is discussed below.

For the AE analyser, 'threshold' and 'gain' are the key parameters governing the measuring sensitivity and the isolation of the electric noise. Both parameters are in *dB* units. For a threshold q_{th} in *dB*, the corresponding AE signal level in volts, below which any AE signal cannot pass, is,

$$v_{th} = 10^{(q_{th}/20 - 3)} \quad (3.10)$$

The higher the threshold level, the lower the sensitivity. The sensitivity is considered to be very high and very low when the

threshold is below 25 *dB* and above 55 *dB*, respectively. High sensitivity is usually used in the case of low signal intensity. In such an instance, special attention should be paid to noise isolation due to the increased risk of picking up noise. In the present research, the AE signals from A588 steel were very weak, so an extremely low threshold level of 18 *dB* was chosen. The corresponding measures to isolate noise will be discussed later.

The SPARTAN-AT analyser manual suggests that the sum of the gain and threshold should lie between 55 and 88 *dB* to ensure accurate functioning and good adjustability of the system. Within this suggested range, a relatively low gain of 39 *dB* was chosen because it may provide a good barrier to the electric noises (i.e., parasitic noise and white noise) of the system [97].

In the oscilloscope, signal display is controlled by a trigger. For noise study, the oscilloscope was in the auto trigger mode. For the formal tests, the raising-edge trigger mode was chosen and the event output of the AE analyser was used as the trigger. When an event occurred, a positive-going pulse from the analyser triggered the display of the corresponding AE amplitude-time history (scope output) and the corresponding loading signal.

Noise Isolation

In addition to the use of a relatively low gain for reducing the effect of the electric noises, three other precautions were taken to isolate the three types of mechanical noise (machine surrounding noise, hydraulic system noise, and loading element noise).

A noise survey was first conducted to determine the frequency range of the noise from the fatigue machine surroundings. When the machine was in a power-on condition, the signal measured under the auto trigger mode of the oscilloscope is shown in Fig. 19. The preamplifier used is the one with an all-pass filter. This signal is considered to be the machine surrounding noise. The Fast Fourier Transformation (FFT) version is shown in Fig. 20. From this frequency spectrum, it is clear that the dominant noise frequency range is below 50 *kHz*. This is why the corner frequency of the high-pass filter of the preamplifier chosen for the fatigue tests is 50 *kHz*. When this preamplifier was used, the signal shown in Fig. 21 was measured. The effect of the filtering is clear.

The noise generated by the hydraulic system is a major concern in noise isolation, because it is usually transmitted into the specimen [67]. In previous research [67, 68], several approaches based upon the principle of sound reflection, were taken to isolate this type of noise. In Ref. [68], sound isolation was provided by numerous aluminum-steel interfaces between the test frame, the hydraulic actuator, and the specimen. The sound wave was reflected at the interfaces due to the impedance mismatch. In Ref. [67], two noise isolation boxes effectively isolated the noise and resulted in 99.5% reduction in noise transmission. Similar to Ref.[67], two noise isolation boxes were designed for this research. The configuration of the boxes is illustrated in Fig. 22. Each box contains three plastic pads separated by two aluminum pads. One box was placed between the loading grips and the actuator; the other was placed between the

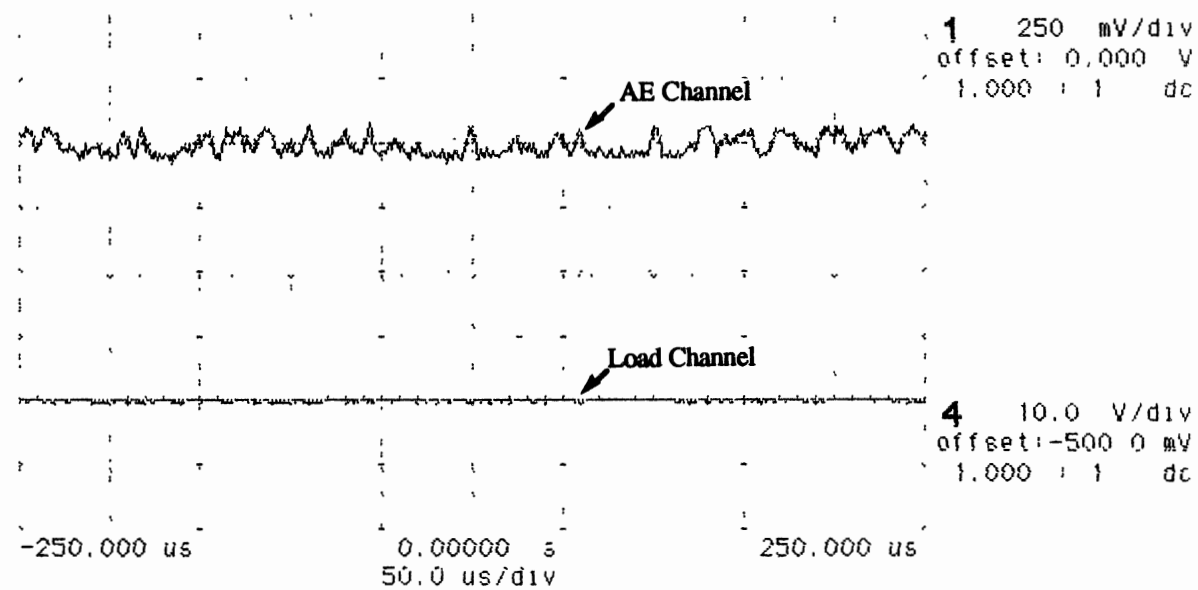


Figure 19. Noise from the Machine Surroundings

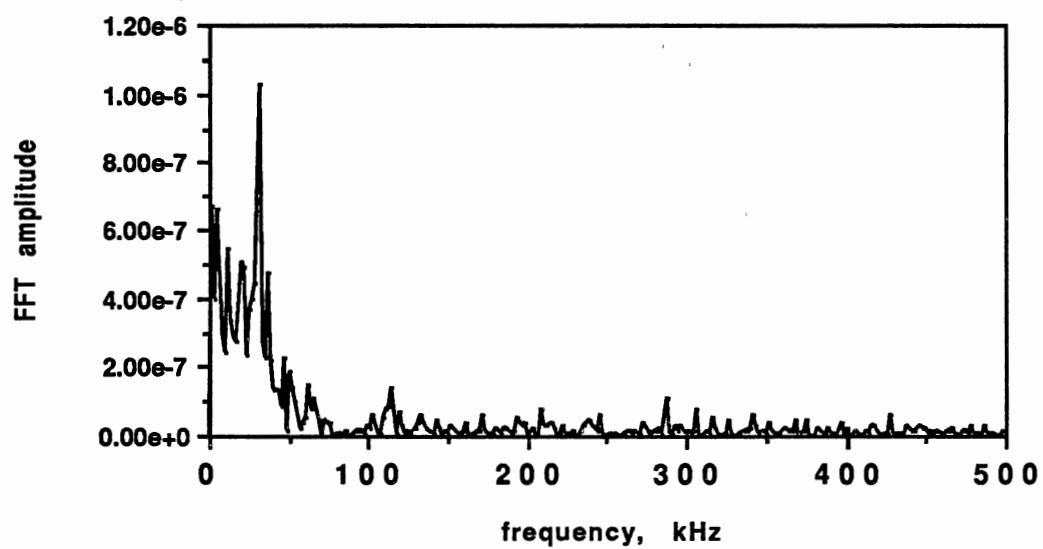


Figure 20. The FFT Spectrum of the Machine Surrounding Noise

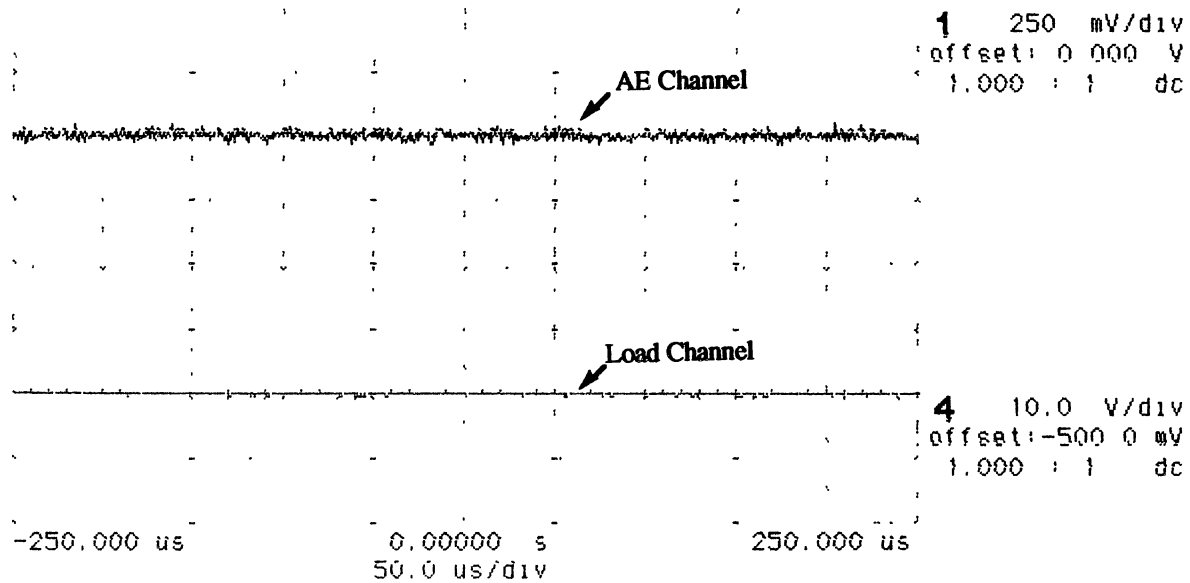


Figure 21. The Signal Measured After Using the Preamplifier With a High-Pass Filter

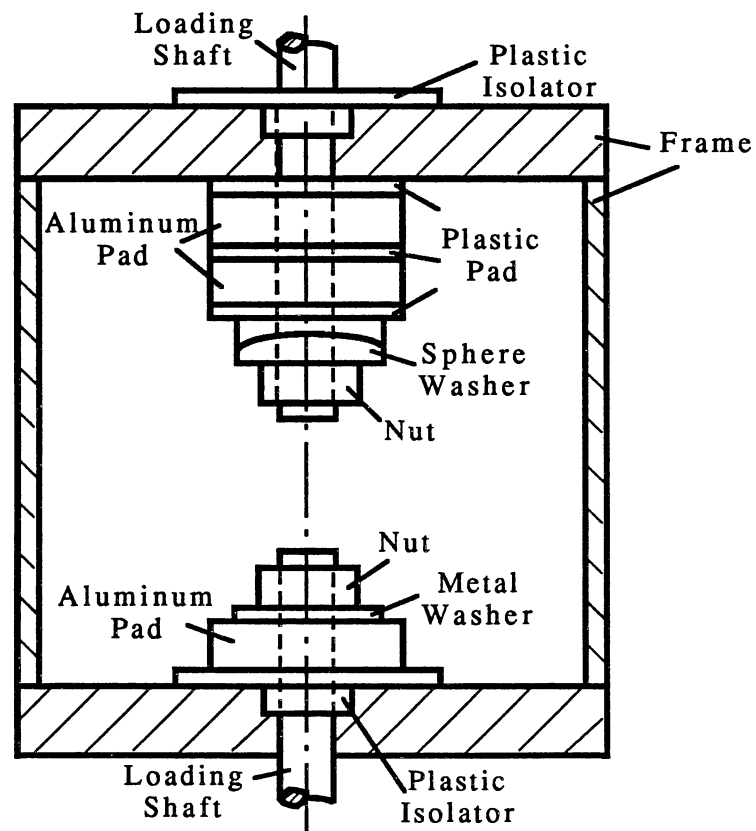
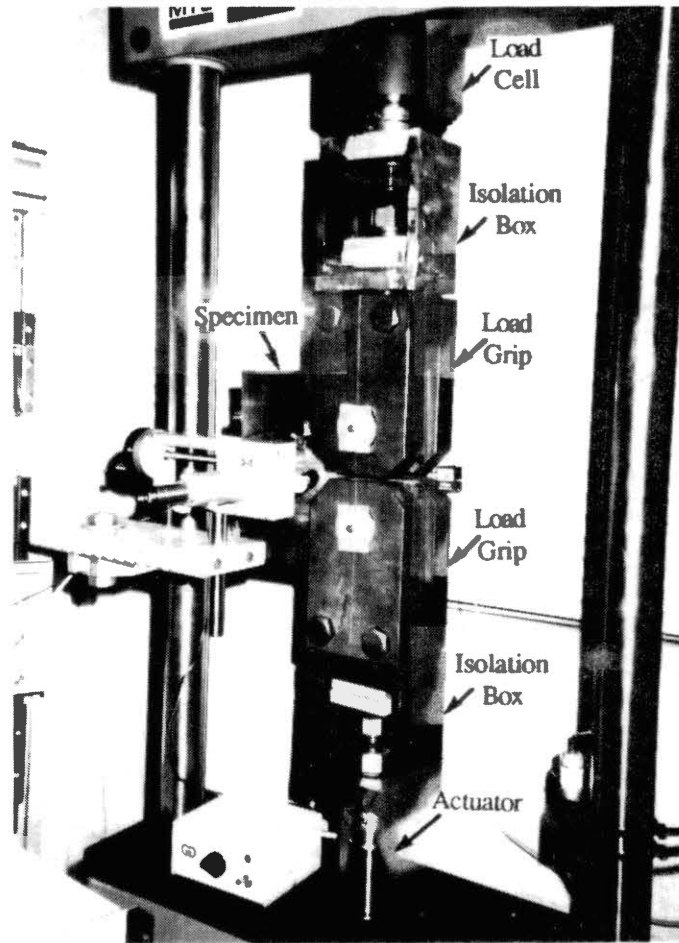


Figure 22. Configuration of the Isolation Boxes

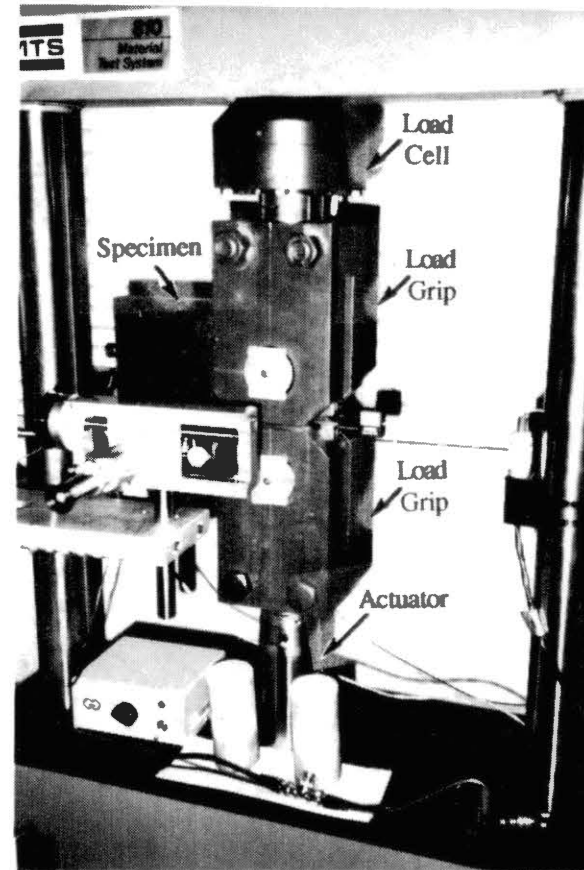
actuator and the load cell. The loading trains with and without the isolation boxes are shown in Fig. 23. The noise isolation achieved by these two boxes was satisfactory. Unfortunately, the loading frequency had to be reduced because of the flexibility of the boxes. Tests originally run at 10 *Hz* were slowed to 4 *Hz* to achieve the same accuracy in load.

After the above measures were taken, a trial test was conducted to determine if external noise had been adequately blocked. The maximum and minimum loadings of all loading cycles applied were 7.4 and 0.74 *kips*, respectively. The loading frequency was 10 *Hz* which simulated the formal fatigue tests. The signal measured under the auto trigger mode is shown in Fig. 24. It was noted that the intense portions of the signal coincided with the decreasing-loading portion of each loading cycle. Previous research [98-100] has shown that such signals are most likely from crack closure or friction caused by rotation of metal loading pins.

To eliminate the signal from crack closure, the crack wake in the trial specimen was widened by using a band saw with a 1/8 *in.* thick blade to cut out the crack. In addition to eliminating contact between crack surfaces, the sawing blunted the crack tip and reduced the level of fatigue damage occurring under initial load cycles. The above trial test was repeated using the sawed specimen. The signal measured remained basically the same as that in Fig. 24. This behavior suggested that loading pin friction was the likely cause of the periodic occurrence of intense signal components.



(a) with the isolation boxes



(b) without the isolation boxes

Figure 23. Two Different Loading Trains for the Loading System

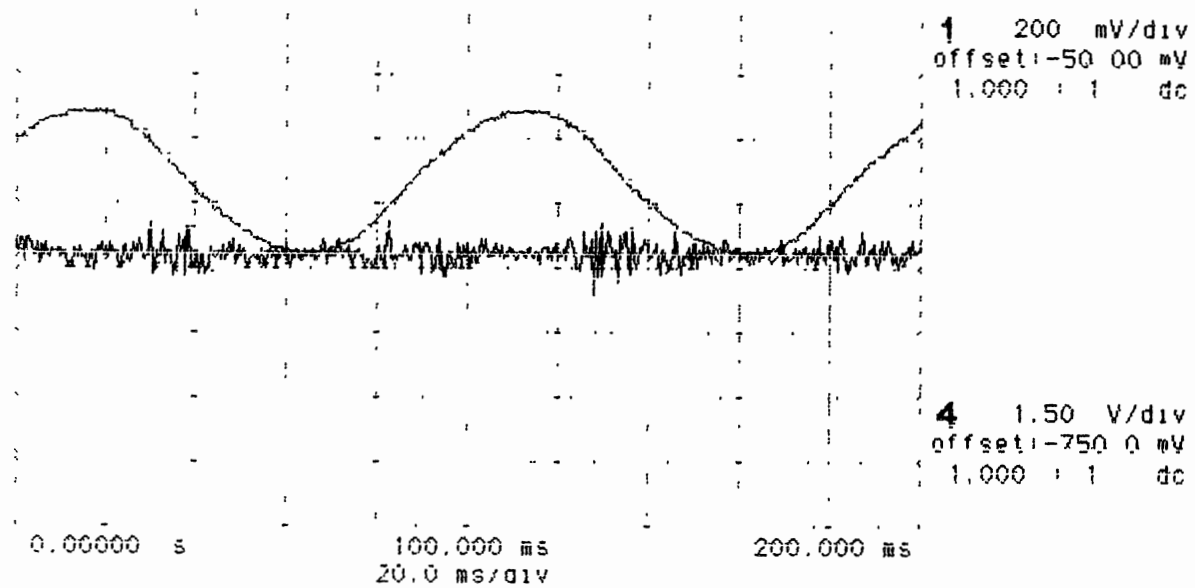


Figure 24. An Example of the Signal Measured during the Trial Test

In previous research [25, 100], coating metal loading pins with Teflon was found to be an effective measure to reduce pin friction. However, this approach is not economical due to the material and manufacturing process costs. Since the loading levels in this research are not very high, a pair of plastic pins made of Delrin were employed. The plastic pins functioned very well. They isolated not only the pin rotation noise but also the hydraulic system noise. Figure 25 is the signal measured from the blunted specimen, under the auto trigger mode, when the plastic pins were used but the isolation boxes were not. It is clear that the periodic, intense signal components disappeared. Under such test conditions, the signal was monitored for a long period of time and no intense signal appeared. Because of the excellent performance of the plastic pins, the isolation boxes became unnecessary for the formal tests.

To reduce the working hours of the plastic pins, they were employed only when the AE signal acquisition was conducted. For the remainder of testing, the original metal loading pins were used. One pair of plastic pins was sufficient for this research.

AE Monitoring and Signal Processing

The AE signal was monitored at preselected points during application of the first and third loading groups. AE data were collected each time the crack length was measured. Figure 26 is an example of the AE events recorded in a peak amplitude vs. time form. The raw signal of an AE event recorded in the time domain is

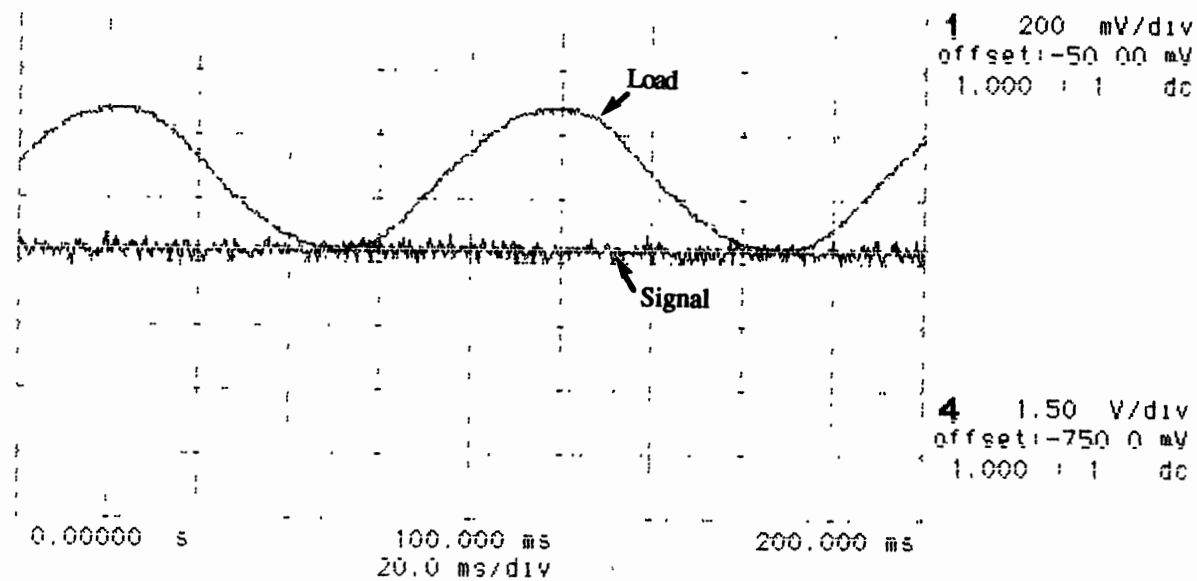


Figure 25. An Example of the Signal Measured During the Trial Test After Using the Plastic Loading Pins

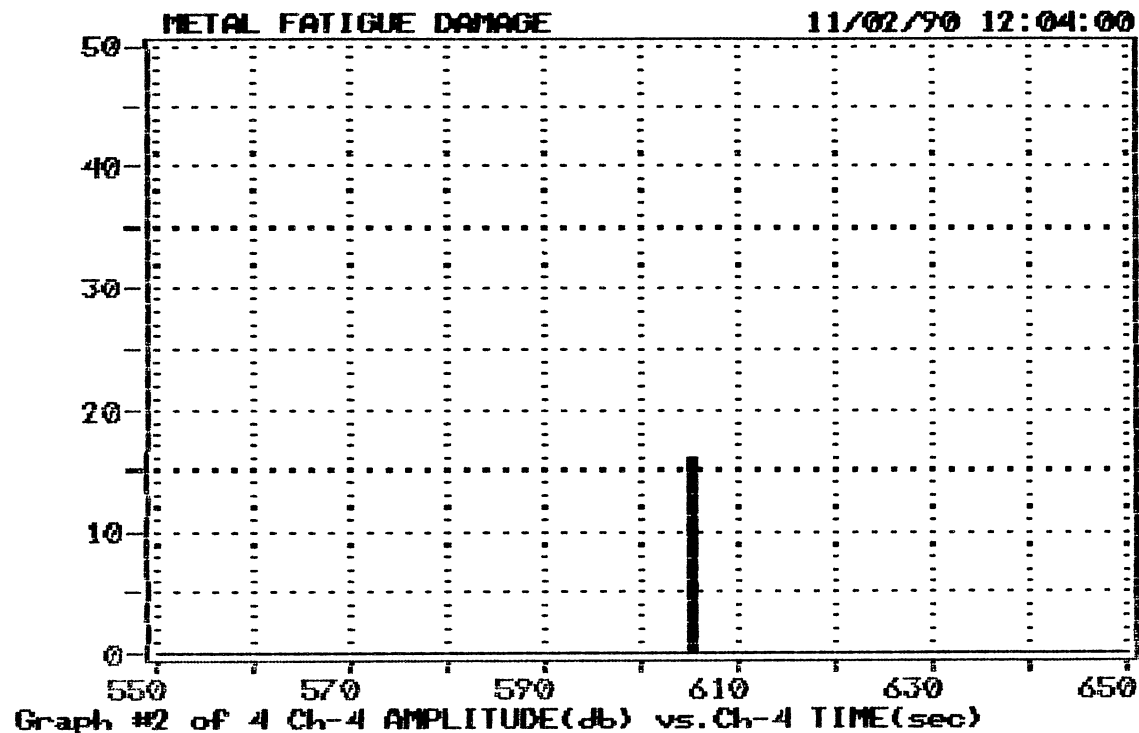
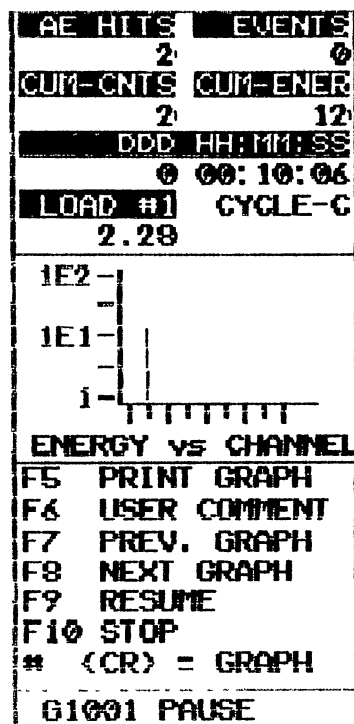


Figure 26. An Example of the AE Events Recorded in a Peak Amplitude vs. Time Form

illustrated in Fig. 27. As mentioned in Chapter II, the AE signal may come from three sources: material deformation and fracture within the plastic zone around the crack tip, crack extension, and crack closure. The first two are directly related to fatigue damage during loading, and are the focuses of this AE study. The last one is relatively unimportant to the present study, although its AE signal component is of potential use for crack closure study. The objective of the signal processing is to separate information on fatigue damage from that on crack closure.

Previous research has shown that AE activities from the first two sources usually occur at the peaks of loading cycles, while the AE activities from crack closure occur near the valleys of loading cycles [31, 63, 99, 101]. The former are defined as "peak emissions", and the latter as "closure emissions". During AE monitoring, the AE signal and the corresponding load signal were simultaneously recorded. With the loading signal as a reference, the peak emissions and the closure emissions can be separated. Similar to Ref.[31], an AE event is counted as a peak emission only if its corresponding load level is not less than 80% of the maximum load in the cycle.

CMOD and BFS Measurements

In this research, crack mouth opening displacement and back-face strain were measured using similar approaches and with the same recording instruments. Figure 28 is the functional diagram of

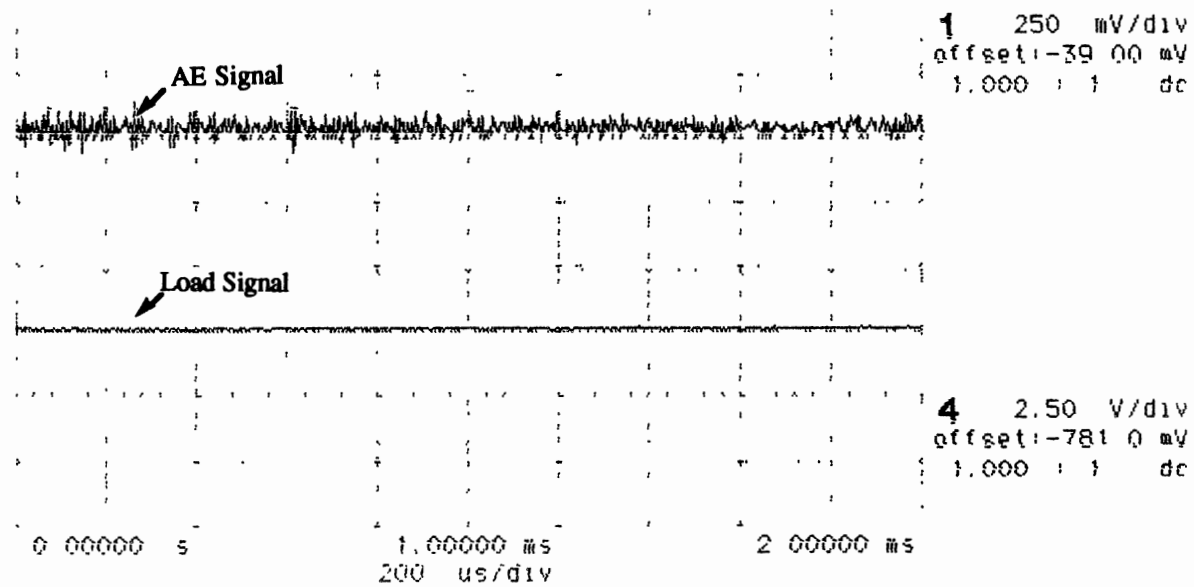


Figure 27. The Raw Signal of an AE Event Recorded in Time Domain

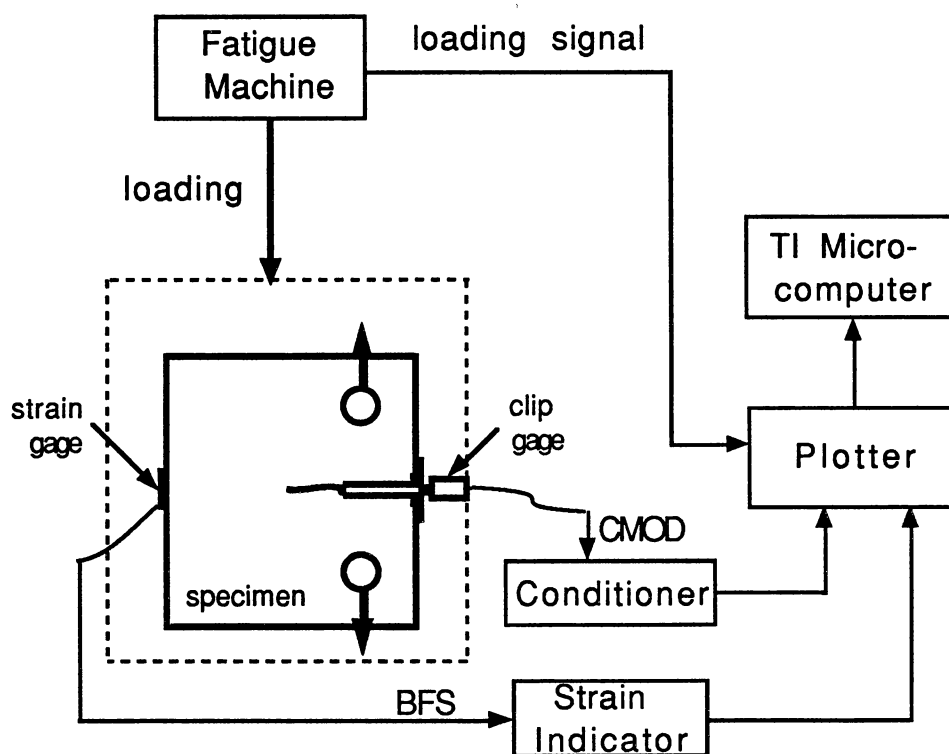


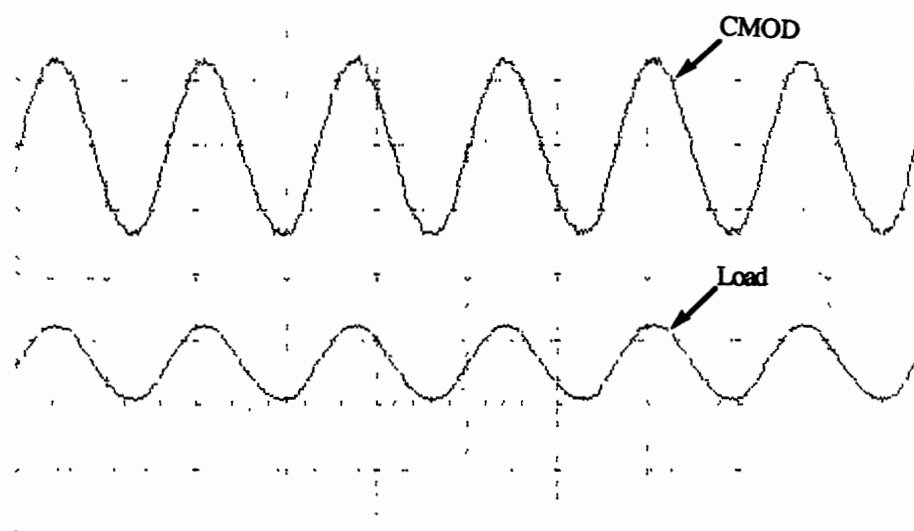
Figure 28. The Functional Diagram of the CMOD and BFS Measurement System

the measurement system. The major elements of the system are transducers, signal processors, a plotter, and a microcomputer.

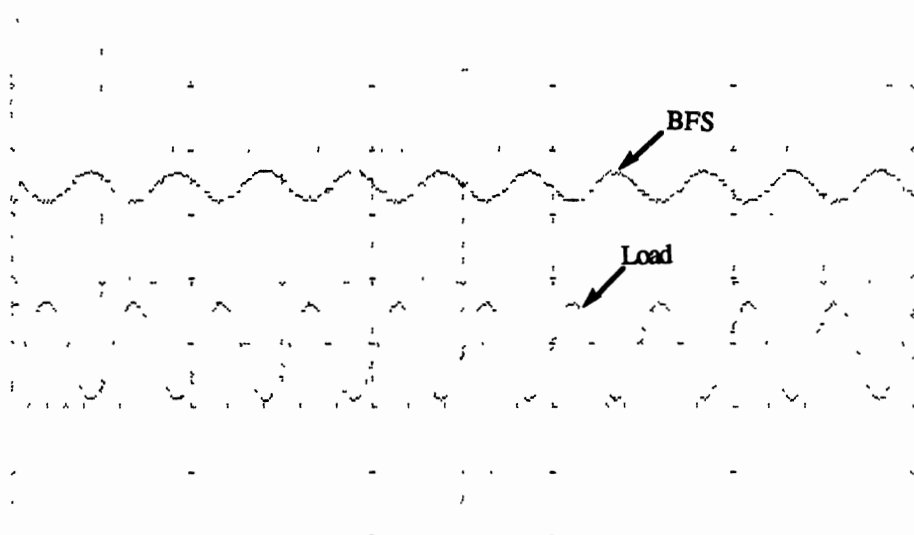
For CMOD measurement, the transducer is a clip gage made by MTS Systems Co. It is capable of measuring displacement up to 0.150 in. The output of the clip gage was amplified by an MTS DC conditioner of model 440.21 and then sent to the plotter.

For BFS measurement, the transducer is a CEA-06-125uw-120 strain gage. Its fatigue life at $\pm 1500 \mu\text{in/in}$ is 10^5 cycles. For each fatigue test with COD monitoring, the maximum number of loading cycles did not exceed 5×10^4 and the strain magnitude was below $500 \mu\text{in/in}$. Thus, a strain gage can easily last a single test. At the beginning of each test, the old strain gage was replaced by a new one to prevent the strain gage from failing during a test. The output of the strain gage was sent to a P-3500 strain indicator. The 1/4-bridge connection mode was adopted. The output from the strain indicator was sent to the plotter for recording.

The plotter is a model HP 7090A and served as a sampler and recorder in this research. The plotter has three input channels, Each channel has its own analog-to-digital (A/D) converter and buffer. Therefore, the CMOD, BFS, and loading signals can be recorded simultaneously. Each buffer can store up to 1000 data points. The recording time and frequency were 200 seconds and 0.1 Hz, respectively. Twenty cycles were recorded each time measurements were taken, with 50 data points per cycle. A TI microcomputer was used to dump the recorded data from the plotter to floppy disks. Figure 29 is an example of the recorded signals. The CMOD and BFS



(a) CMOD and Load Histories



(b) BFS and Load Histories

Figure 29. An Example of the CMOD and BFS Signals Recorded

signals varied following the variations in loading with almost no phase delay. Also the BFS signal was always negative as mentioned in Chapter II.

Striation Observations

Striation observations were made on one sample under a scanning electron microscope of model Jeol JSM 35. The magnification capability of the microscope ranges from approximately 20 to 20,000. The sample was taken from the fracture surface of a broken CT specimen. The dimensions of the sample are $0.55 \times 0.45 \times 0.35$ in. The fracture surface on the sample was formed with $n = 49$ in the second loading group. The match between the sample fracture surface and the corresponding loading spectrum is assured using the following procedure.

For each crack growth test, the crack tip positions at the beginning and end of the loading spectrum were marked on the specimen surface. Any striations resulting from the loading spectrum should be between the two marks. These marks are illustrated in Fig. 30. "Beach markings" on the fracture surface of the specimen were used to check the mark positions. Beach markings are the visible bands perpendicular to the growth direction as shown in Fig. 30. They are also called "clam shell markings". Each band represents a different loading condition. Therefore, the two marks for each loading spectrum correspond to the edges of its band or its pair of beach markings. The marks for the loading spectrum chosen

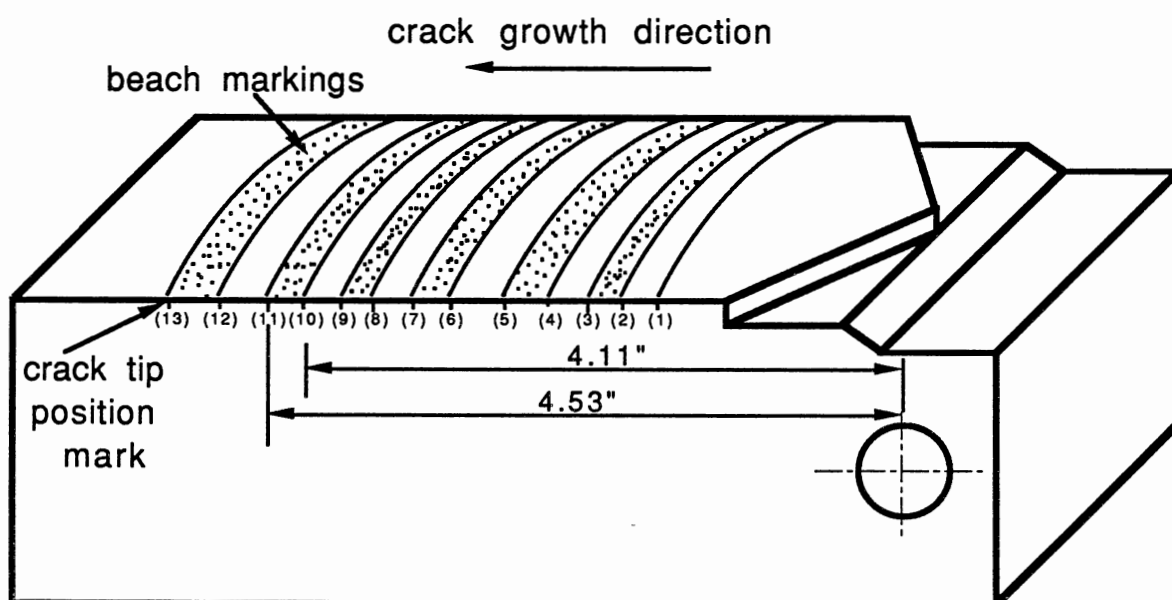


Figure 30. Illustration of the Crack Tip Position Marks and Beach Markings on a Fractured CT Specimen

signals varied following the variations in loading with almost no sample encompasses the band between mark (11) and (10) as shown in Fig. 31.

The striation observations were made at seven arbitrary points on the sample. Their locations are indicated in Fig. 31. Table 7 lists the coordinates of each point in the X-Y coordinate system in Fig. 31.

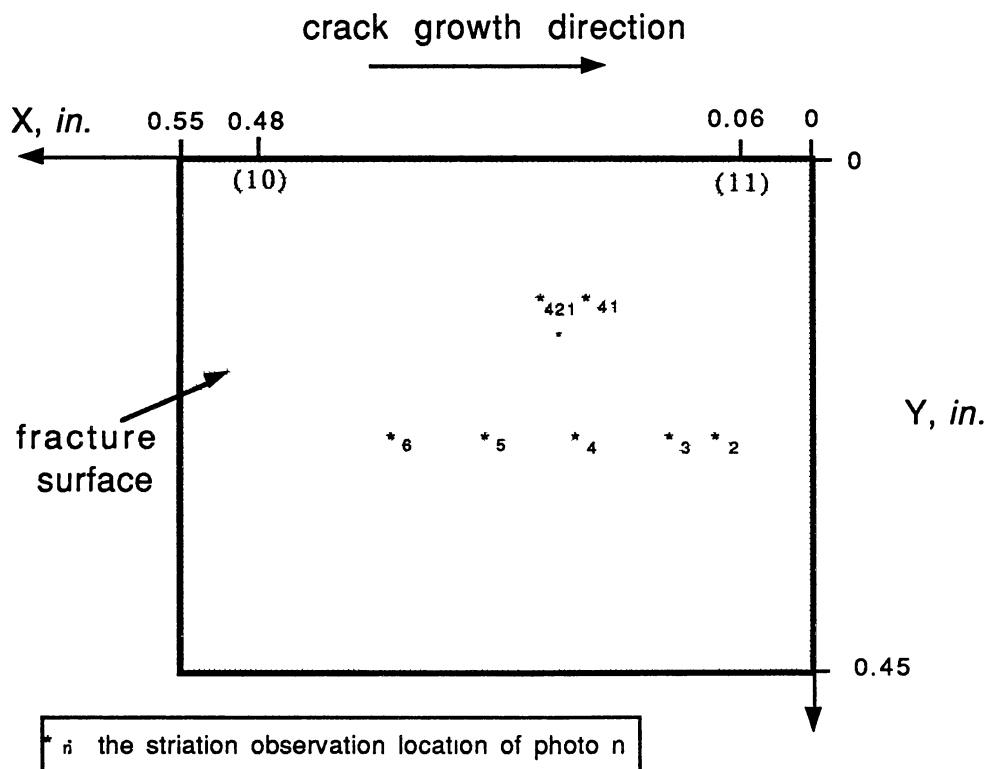


Figure 31. The Sample for Striation Observations

TABLE 7
LOCATIONS OF STRIATION OBSERVATIONS

Location & Crack Length	Photo No.						
	2	3	4	5	6	41	421
X(mm)	0.08	0.12	0.20	0.28	0.36	0.19	0.23
Y(mm)	0.24	0.24	0.24	0.24	0.24	0.12	0.12
a(in.)	4.51	4.47	4.39	4.31	4.23	4.40	4.36

CHAPTER IV

RESULTS AND DISCUSSION

This chapter presents the results of crack growth measurements made with a traveling microscope, acoustic emission measurements, crack opening displacement measurements, back-face strain measurements, and striation observations. The presentation of each type of result is followed by a discussion. Finally, a summary of the results is given at the end of this chapter.

Macrocrack Growth

In this section, the transition in the overload effect and the minor cycle behavior will be discussed in terms of the crack growth rate data. Overload acceleration and retardation will be evaluated using average and statistical baselines. The minor cycle behavior to be studied includes the threshold aspect and the R_m effect. The effects of crack increment between load sheddings, crack length and loading pins on the crack growth rate data are also discussed.

The crack growth data of the two specimens, namely TH1 and TH2, are listed in Tables 8 and 9, respectively. For each crack increment, the number of loading cycles applied and the loading group name are also given. The characteristics of each loading group

TABLE 8

SUMMARY OF CRACK PROPAGATION DATA (SPECIMEN TH1)

Crack Length a (in.)	Cycles Applied ΔN (10^2 cycles)	Loading Spectrum		Crack Length a (in.)	Cycles Applied ΔN (10^2 cycles)	Loading Spectrum	
		Group No.	n			Group No.	n
2.86965-2.89720	1652	4		3.71705-3.74730	6168	1	49
2.89720-2.93085	1654			3.74730-3.78040	6489		
2.93085-2.95130	1456			3.78040-3.80965	6115		
2.95130-2.98675	17865	1	99	3.95085-3.97885	1376	4	
2.98675-3.02365	13114			3.97885-4.00790	1510		
3.02365-3.06620	11768			4.00790	20		
3.14040-3.16975	1348	4		4.10895-4.13865	378	2	49
3.16975-3.19395	1350			4.13865-4.16140	305		
3.19395-3.22465	1816			4.16140-4.18200	330		
3.22465-3.24530	1647	1	9	4.18200-4.20790	317		
3.24530-3.26570	1841			4.20790-4.23675	289		
3.26570-3.28375	1365			4.23675-4.25770	260		
3.37330-3.39820	1318	4		4.25770-4.28655	290		
3.39820-3.43020	2162			4.28655-4.31030	274		
3.43020-3.45065	1028			4.31030-4.33710	292		
3.45065-3.47795	1290	1	4	4.33710-4.35880	245		
3.47795-3.49975	1124			4.35880-4.38175	275		
3.49975-3.52500	1223			4.38175-4.40495	275		
3.59035-3.61230	1284	4		4.40495-4.42865	223		
3.61230-3.63305	1271			4.42865-4.45195	265		
3.63305-3.66695	1969			4.45195-4.47320	253		
3.66695-3.69000	3564	1	49	4.47320-4.50400	288		
3.69000-3.71705	5622			4.50400-4.52795	255		

TABLE 9
SUMMARY OF CRACK PROPAGATION DATA (SPECIMEN TH2)

Crack Length a (in.)	Cycles Applied ΔN (10^2 cycles)	Loading Spectrum		Crack Length a (in.)	Cycles Applied ΔN (10^2 cycles)	Loading Spectrum	
		Group No.	n			Group No.	n
2.66925-2.69445	1368	4		3.58725-3.61005	1295	4	
2.69445-2.71960	1463			3.61005-3.64490	2178	3 (middle)	9
2.76860-2.80105	5187	1	49	3.64490-3.67580	1818		
2.80105-2.82045	2845			3.67580-3.69610	873		
2.82045-2.84450	4440			3.69610-3.71705	896		
2.84450-2.86850	4991			3.81240-3.83900	1646	4	
2.86850-2.90020	5258			3.83900-3.86220	1585		
3.00745-3.02795	910	4		3.86220-3.89230	2508	3 (bottom)	9
3.02795-3.05455	1329			3.89230-3.91415	1883		
3.05455-3.07660	186	1	0	3.91415-3.93545	1431		
3.07660-3.09890	221			3.93545-3.96060	1469		
3.09890-3.12745	306			3.96060-3.98265	1538		
3.12745-3.14990	271			4.08315-4.10895	1340	4	
3.14990-3.16995	219			4.10895-4.13110	1403		
3.26810-3.29375	1207	4		4.13110-4.15495	19640	1	999
3.29375-3.31880	1127			4.15495-4.17790	29293		
3.31880-3.35080	1723	3 (top)	9	4.17790-4.22335	41873		
3.35080-3.37920	1370			4.22335-4.25195	27963		
3.37920-3.41145	1211			4.25195-4.28695	33429		
3.41145-3.43960	1274			4.44135-4.47310	1814	4	
3.43960-3.45960	726			4.47310-4.50100	1459		
3.56680-3.58725	1153	4		4.50100	10	2	9

can be found in Table 3. The crack growth rate data which will be discussed next are calculated from Tables 8 and 9, and are summarized in Table 10.

In Table 10, parameter a is the average of the initial and final crack lengths for each crack increment measured, $\frac{da}{dN}$ is the ratio of the crack increment to the number of loading cycles applied, and $\left(\frac{da}{dN}\right)_{com}$ is the crack growth rate of the complex cycles. The complex cycle crack growth rate is equal to the ratio of the crack increment to the number of complex loading cycles applied or $(n+1)\left(\frac{da}{dN}\right)$. In the following, the transition in the overload effect and the minor cycle behavior will be discussed in relation to the crack growth rate data from different types of complex cycle.

Transition in the Overload Effect

Baseline Calculation. Both overload acceleration and retardation are the result of load interaction. The non-interaction model as mentioned in Chapter II is used as a baseline for evaluating accelerated and retarded crack growths. According to the non-interaction model, the crack growth rate of a complex cycle is equal to the sum of the crack growth rate of the overload cycle and that of each minor cycle in the complex cycle. That is,

$$\left(\frac{da}{dN}\right)_{com} = \left(\frac{da}{dN}\right)_o + n\left(\frac{da}{dN}\right)_m \quad (4.1)$$

where $\left(\frac{da}{dN}\right)_o$ is the crack growth rate of the overload cycles, and $\left(\frac{da}{dN}\right)_m$

TABLE 10
CRACK GROWTH DATA OF LOADING GROUP ONE

Specimen TH1				Specimen TH2			
Crack Length a (in.)	Crack Growth Rate		n	Crack Length a (in.)	Crack Growth Rate		n
	da/dN (10 ⁻⁸ in/cyc)	(da/dN) _{com} (10 ⁻⁶ in/cyc)			da/dN (10 ⁻⁸ in/cyc)	(da/dN) _{com} (10 ⁻⁶ in/cyc)	
2.96903	1.984	1.984	99	2.78483	6.256	3.128	49
3.00520	2.183	2.183		2.81075	6.818	3.409	
3.04493	3.615	3.615		2.83248	5.416	2.708	
				2.85650	4.808	2.404	
3.23500	12.54	1.254	9	2.88435	6.028	3.014	0
				3.06588	118.5	1.185	
3.25500	11.08	1.108		3.08775	100.9	1.009	
3.27470	13.22	1.322	4	3.11318	93.30	.9330	9
				3.13868	82.84	.8284	
3.46430	21.16	1.058		3.15993	91.55	.9155	
3.48890	19.40	.9698	49	3.87725	12.00	1.200	999
3.51240	20.65	1.032		3.90323	11.60	1.160	
				3.92480	14.88	1.488	
3.67848	6.467	3.234	49	3.94803	17.12	1.712	999
3.70353	4.811	2.405		3.97163	14.34	1.434	
3.73218	4.904	2.452		4.14303	1.214	12.14	
				4.16643	0.783	7.830	
3.76385	5.100	2.550	49	4.20063	1.085	10.85	999
				4.23765	1.022	10.22	
3.79503	4.783	2.392		4.26945	1.046	10.46	

is the crack growth rate of the minor cycles. If the measured crack growth rate of a complex cycle is larger than the value calculated from Eq. (4.1), overload acceleration is assumed to occur. If the measured crack growth rate is smaller than the calculated value, overload retardation is assumed to occur.

To determine the crack growth rate baseline, the overload crack growth rate data from the present research and the minor cycle crack growth rate data from previous research [6] are employed. Because the crack growth rate data are scattered, an average baseline and two statistical baselines are calculated. The average baseline is determined using the average values of the overload and minor cycle crack growth rate data. The statistical baselines are determined using the upper and lower confidence limits of the population means calculated from the data, respectively. Details of the calculation are provided in the following.

The five crack growth rate data corresponding to loading group one and $n = 0$ in Table 10 are used to determine the overload crack growth rate. Their average is,

$$\left(\overline{\frac{da}{dN}}\right)_o = 9.742 \times 10^{-7} \text{ in/cycle} \quad (4.2)$$

The confidence limits of their population mean can be calculated as follows, using the approach in Appendix A. For these crack growth rate data, the number of data, N_s , is five and the estimate of the population variance, S , is 0.13421×10^{-6} in/cycle. With 95% confidence, the upper and lower limits of the population mean are,

$$\left(\frac{da}{dN}\right)_{o,ul,95} = \left(\frac{da}{dN}\right)_o + 1.96 \frac{S}{\sqrt{N_s}} = 10.9 \times 10^{-7} \text{ in/cycle} \quad (4.3)$$

$$\left(\frac{da}{dN}\right)_{o,ll,95} = \left(\frac{da}{dN}\right)_o - 1.96 \frac{S}{\sqrt{N_s}} = 8.57 \times 10^{-7} \text{ in/cycle} \quad (4.4)$$

With 90% confidence, the upper and lower limits of the population mean are,

$$\left(\frac{da}{dN}\right)_{o,ll,90} = \left(\frac{da}{dN}\right)_o + 1.65 \frac{S}{\sqrt{N_s}} = 10.7 \times 10^{-7} \text{ in/cycle} \quad (4.5)$$

$$\left(\frac{da}{dN}\right)_{o,ll,90} = \left(\frac{da}{dN}\right)_o - 1.65 \frac{S}{\sqrt{N_s}} = 8.75 \times 10^{-7} \text{ in/cycle} \quad (4.6)$$

A regression line for crack growth rate under loading of $R=0.3$, reported in Ref. [6], was used to determine the minor cycle growth rate, since the R value of the minor cycles in loading group one is also 0.3. The regression line can be expressed as [6],

$$\frac{da}{dN} = 1.77 \times 10^{-10} \Delta K^{3.24} \quad (4.7)$$

or,

$$\log\left(\frac{da}{dN}\right) = -9.75203 + 3.24 \log(\Delta K) \quad (4.8)$$

The confidence limits of the population mean of the minor cycle

crack growth rate are calculated as follows using the approach in Appendix B.

Letting $x = \log(\Delta K)$, $\hat{y} = \log\left(\frac{da}{dN}\right)$, $\hat{\beta}_0 = -9.75203$, and $\hat{\beta}_1 = 3.24$, Equation (4.8) can be rewritten as,

$$\hat{y} = \hat{\beta}_0 + \hat{\beta}_1 x \quad (4.9)$$

Several simple statistical parameters for the original test data described by the regression line are calculated and listed in Table 11. The remaining statistical parameters needed for the confidence limit calculation are,

$$S_{xx} = \Sigma x^2 - \frac{(\Sigma x)^2}{n_s} = 2.78816353$$

$$S_{yy} = \Sigma y^2 - \frac{(\Sigma y)^2}{n_s} = 29.5704311$$

$$S_{xy} = \Sigma xy - \frac{(\Sigma x)(\Sigma y)}{n_s} = 8.99533677$$

$$S_\varepsilon = \sqrt{\frac{S_{yy} - \hat{\beta}_1 S_{xy}}{n_s - 2}} = 0.065499751$$

$$d_f = n_s - 2 = 128$$

For 95% confidence, θ is 0.05 and $t_{\theta/2}$ is 1.98. The upper and lower limits of the population mean of the regression line in Eq. (4.9)

TABLE 11
STATISTICAL PARAMETERS FOR DATA
FROM [6]

n	130
Σx^2	160.31326
Σx	143.10228
\bar{x}	1.100786769
Σxy	-879.08493
Σy^2	5036.30636
Σy	-806.76866
\bar{y}	-6.20591276

are,

$$\begin{aligned}
 (UL)_l &= \hat{y} + 1.98S_\varepsilon \sqrt{\frac{1}{n_s} + \frac{(x-\bar{x})^2}{S_{xx}}} \\
 &= \hat{y} + 0.129689507[0.007692307 + \\
 &\quad 0.35865902(x-1.00786769)^2]^{1/2}
 \end{aligned} \tag{4.10}$$

$$\begin{aligned}
 (LL)_l &= \hat{y} - 1.98S_\varepsilon \sqrt{\frac{1}{n_s} + \frac{(x-\bar{x})^2}{S_{xx}}} \\
 &= \hat{y} - 0.129689507[0.007692307 + \\
 &\quad 0.35865902(x-1.00786769)^2]^{1/2}
 \end{aligned} \tag{4.11}$$

For the first loading group, the stress intensity factor range of the minor cycles is $4.5 \text{ ksi}\sqrt{in}$, therefore,

$$x = \log(4.5) = 0.653212513 \quad \log(\text{ksi}\sqrt{in})$$

$$\hat{y} = -9.75203 + 3.24x = -7.635621455 \quad \log(\text{ksi}\sqrt{in})$$

Plugging x and \hat{y} into Eqs. (4.10) and (4.11) yields the upper and lower confidence limits for these particular minor cycles,

$$(UL)_m = -7.599045368 \quad \log(\text{ksi}\sqrt{in})$$

$$(LL)_m = -7.672197542 \log(ksi\sqrt{in})$$

Thus, the upper and lower confidence limits of the population mean of the minor cycle crack growth rate are,

$$\left(\frac{da}{dN}\right)_{m,ul,95} = 10^{(UL)_m} = 2.52 \times 10^{-8} \text{ in/cycle} \quad (4.12)$$

$$\left(\frac{da}{dN}\right)_{m,ll,95} = 10^{(LL)_m} = 2.13 \times 10^{-8} \text{ in/cycle} \quad (4.13)$$

The average minor cycle crack growth rate is taken as,

$$\left(\frac{da}{dN}\right)_m = \frac{1}{2} \left[\left(\frac{da}{dN}\right)_{m,ul,95} + \left(\frac{da}{dN}\right)_{m,ll,95} \right] = 2.32 \times 10^{-8} \text{ in/cycle} \quad (4.14)$$

From Eqs. (4.1), (4.2), and (4.14), the average baseline for the crack growth rate is,

$$\left(\frac{da}{dN}\right)_{com} = \left(\frac{da}{dN}\right)_o + n \left(\frac{da}{dN}\right)_m = (9.72 + 0.232n) \times 10^{-7} \text{ in/cycle} \quad (4.15)$$

Equation (4.15) represents the crack growth rate of a complex cycle with n minor cycles in the first loading group under the assumption of no interaction between loading cycles.

According to the chain rule of compound probabilities [102], the upper limit of the population mean of the crack growth rate of a complex cycle with n minor cycles in the first loading group is, with 90% confidence and the assumption of no load interaction,

$$\left(\frac{da}{dN}\right)_{com,ul,90} = \begin{cases} \left(\frac{da}{dN}\right)_{o,ul,95} + n \left(\frac{da}{dN}\right)_{m,ul,95} & (n>0) \\ \left(\frac{da}{dN}\right)_{o,ul,90} & (n=0) \end{cases} \quad (4.16)$$

or,

$$\left(\frac{da}{dN}\right)_{com,ul,90} = \begin{cases} (10.918+0.252n) \times 10^{-7} \text{ in/cycle} & (n>0) \\ 10.732 \times 10^{-7} \text{ in/cycle} & (n=0) \end{cases} \quad (4.17)$$

Similarly, its lower limit is obtained as follows, with 90% confidence and the assumption of no load interaction,

$$\left(\frac{da}{dN}\right)_{com,ul,90} = \begin{cases} \left(\frac{da}{dN}\right)_{o,ul,95} + n \left(\frac{da}{dN}\right)_{m,ul,95} & (n>0) \\ \left(\frac{da}{dN}\right)_{o,ll,90} & (n=0) \end{cases} \quad (4.18)$$

or,

$$\left(\frac{da}{dN}\right)_{com,ll,90} = \begin{cases} (8.566+0.213n) \times 10^{-7} \text{ in/cycle} & (n>0) \\ 8.752 \times 10^{-7} \text{ in/cycle} & (n=0) \end{cases} \quad (4.19)$$

Equations (4.17) and (4.19) constitute a bounded baseline range for evaluating the overload effect.

Overload Effect. In this section, the crack growth rate data for specimens TH1 and TH2 are first discussed as separate topics. The

original data for each specimen in Table 10 are compared with the average baseline from Eq. (4.15). The 90% confidence limits of the population means of these original data are compared with the 90% confidence limit baselines of Eqs. (4.17) and (4.19). Then the data for both specimens are combined, and compared with the average baseline and the 90% confidence limit baselines. These comparisons are used to demonstrate the existence of a transition in the overload.

The statistical parameters for the crack growth rate data from specimens TH1 and TH2 are listed in Table 12 and 13, respectively. Table 14 presents the statistical parameters of the crack growth rate data from both specimens. These parameters are calculated using the approach in Appendix A. As an example, calculations for the case of $n = 49$ in Table 14 follow.

For the load spectra with $n = 49$ in the first loading group, each specimen has five crack growth rate data. They are listed in the fourth row and the second column of Table 14. Therefore,

$$N_s=10$$

The average and the estimation of the population variance of these ten data are,

$$\left(\overline{\frac{da}{dN}}\right)_{com} = 2.77 \times 10^{-6} \text{ in/cycle}$$

$$S = 3.91 \times 10^{-7} \text{ in/cycle}$$

TABLE 12
90% CONFIDENCE LIMITS OF THE OVERLOAD EFFECT
(SPECIMEN TH1)

n	$\left(\frac{da}{dN}\right)_{com}$ (10^{-6} in/cyc)	$\left(\frac{da}{dN}\right)_{com}$ (10^{-6} in/cyc)	S (10^{-7} in/cyc)	n _s	$\left(\frac{da}{dN}\right)_{com,ul}$ (10^{-6} in/cyc)	$\left(\frac{da}{dN}\right)_{com,ll}$ (10^{-6} in/cyc)
4	1.058	1.020	0.45	3	1.063	0.977
	.9698					
	1.032					
9	1.254	1.228	1.09	3	1.332	1.124
	1.108					
	1.322					
49	3.234	2.607	3.56	5	2.870	2.344
	2.406					
	2.452					
	2.550					
	2.392					
99	1.984	2.804	8.16	3	3.586	2.022
	2.813					
	3.615					

TABLE 13
90% CONFIDENCE LIMITS OF THE OVERLOAD EFFECT
(SPECIMEN TH2)

n	$\left(\frac{da}{dN}\right)_{com}$ (10^{-6} in/cyc)	$\left(\frac{da}{dN}\right)_{com}$ (10^{-6} in/cyc)	S (10^{-6} in/cyc)	n _s	$\left(\frac{da}{dN}\right)_{com,ul}$ (10^{-6} in/cyc)	$\left(\frac{da}{dN}\right)_{com,ll}$ (10^{-6} in/cyc)
0	1.185	0.974	.1340	5	1.073	.8750
	1.009					
	.9330					
	.8284					
	.9155					
9	1.200	1.399	.2257	5	1.566	1.232
	1.160					
	1.488					
	1.712					
	1.434					
49	3.128	2.933	.3880	5	3.221	2.645
	3.409					
	2.708					
	2.404					
	3.014					
999	1.214	10.31	1.565	5	11.47	9.143
	.7830					
	1.085					
	1.022					
	1.046					

TABLE 14

90% CONFIDENCE LIMITS OF THE OVERLOAD EFFECT
(SPECIMENS TH1 & TH2)

n	$\left(\frac{da}{dN}\right)_{com}$ (10^{-6} in/cyc)	$\left(\frac{da}{dN}\right)_{com}$ (10^{-6} in/cyc)	S (10^{-6} in/cyc)	n_s	$\left(\frac{da}{dN}\right)_{com,ul}$ (10^{-6} in/cyc)	$\left(\frac{da}{dN}\right)_{com,ll}$ (10^{-6} in/cyc)
0	1.185	0.974	0.134	5	1.073	0.875
	1.009					
	.9330					
	.8284					
	.9155					
4	1.058	1.020	0.045	3	1.063	0.977
	.9698					
	1.032					
9	1.254	1.355	0.201	8	1.503	1.167
	1.108					
	1.322					
	1.200					
	1.160					
	1.488					
	1.712					
	1.434					
49	3.234	2.770	0.391	10	3.060	2.480
	2.406					
	2.452					
	2.550					
	2.392					
	3.128					
	3.409					
	2.708					
	2.404					
	3.014					
99	1.984	2.804	0.816	3	3.586	2.022
	2.813					
	3.615					
999	1.214	10.31	1.565	5	11.47	9.143
	.7830					
	1.085					
	1.022					
	1.046					

With 90% confidence, the upper and lower limits of their population mean are,

$$\left(\frac{da}{dN}\right)_{com,ul,90} = \left(\frac{da}{dN}\right)_{com} + 1.65 \frac{S}{\sqrt{N_s}} = 3.06 \times 10^{-6} \text{ in/cycle}$$

$$\left(\frac{da}{dN}\right)_{com,ll,90} = \left(\frac{da}{dN}\right)_{com} - 1.65 \frac{S}{\sqrt{N_s}} = 2.48 \times 10^{-6} \text{ in/cycle}$$

The 90% confidence limits of the population means in Tables 12 through 14 are used to evaluate the overload effect from a statistical point of view.

Figure 32 is a comparison between the original crack growth rate data from specimen TH1 and the average baseline of Eq. (4.15). Figure 33 is a comparison between the 90% confidence limits of the population means of these data and the 90% confidence limit baselines of Eqs. (4.17) and (4.19). The horizontal axes of both figures are the number of loading cycles per complex cycle, n_c in log scale. In the present research,

$$n_c = n + 1 \tag{4.20}$$

For a particular value of n_c , the crack growth rate range bounded by the two baselines in Fig. 33 represents the estimated variation range of the crack growth rate of a complex cycle with $(n_c - 1)$ minor cycles when load interaction is ignored. The confidence interval calculated from the test data represents the estimated variation range of the

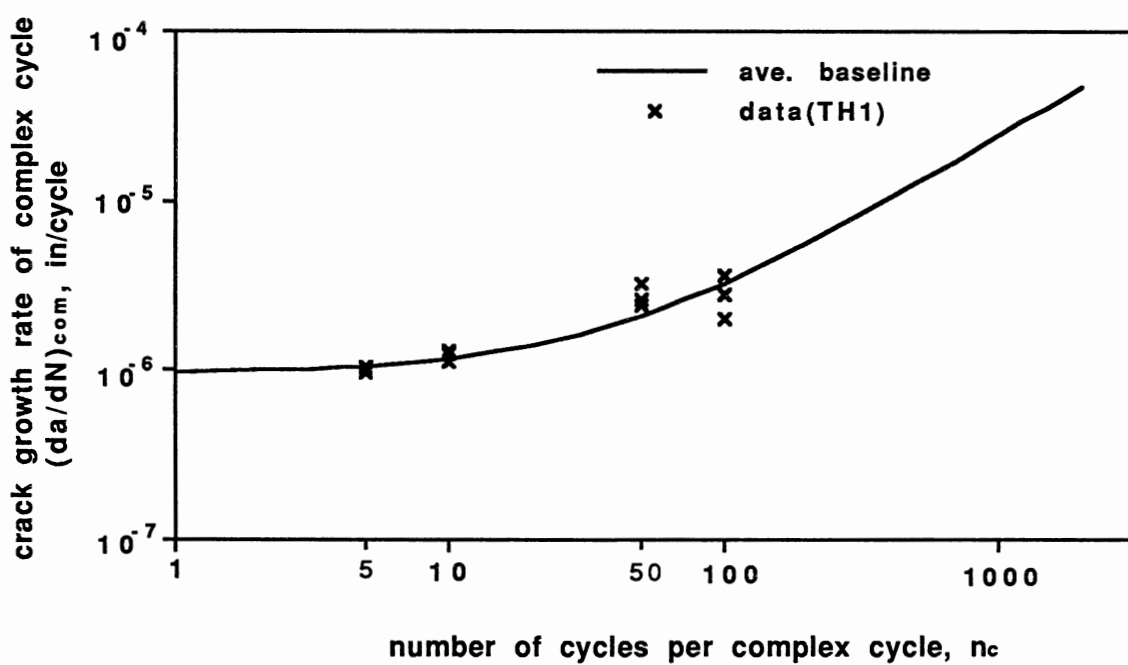


Figure 32. Overload Effect on Crack Growth of Specimen TH1

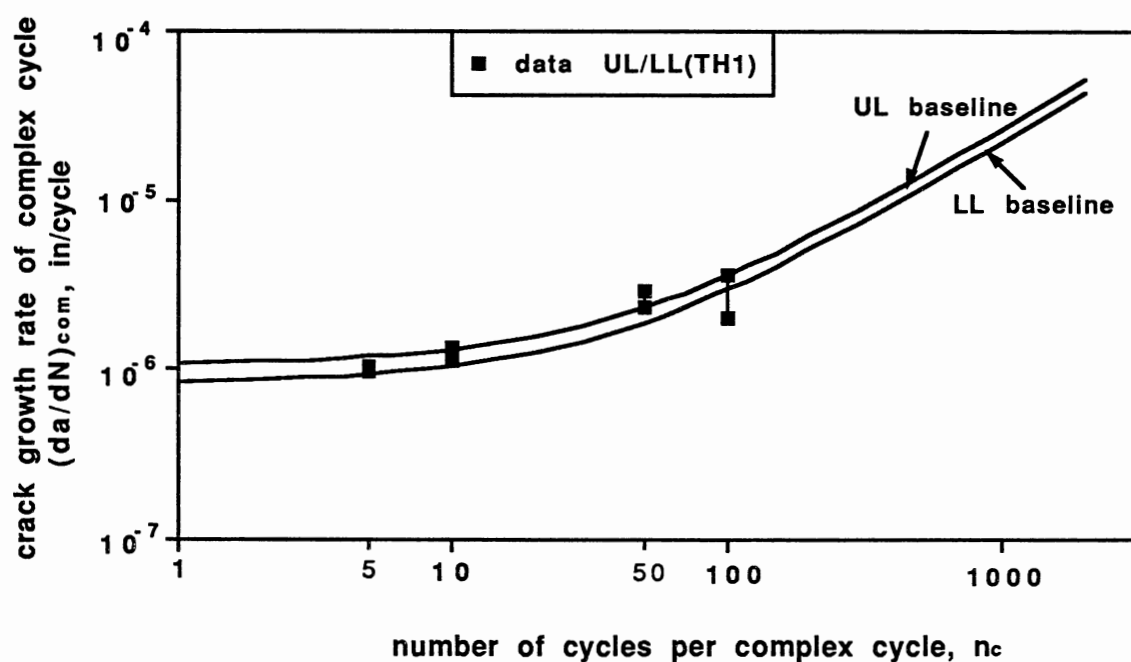


Figure 33. Statistical Demonstration of the Overload Effect With Crack Growth Rate Data from Specimen TH1

crack growth rate when load interaction is experimentally taken into account. Both estimates are obtained with 90% confidence.

Figures 32 and 33 show that the test data are on or slightly above the baseline (range) for $5 < n_c \leq 50$, which means that crack growth retardation is not occurring under such loading. As n_c approaches 50, there is some evidence of acceleration. At $n_c=100$, the test data lie below the baseline values, indicating the transition.

Similar to Figs. 32 and 33, Figs. 34 and 35 compare the test results from specimen TH2 with the average baseline and the 90% confidence limit baselines, respectively. Figures 34 and 35 show that crack growth retardation does not occur under loading spectra with $1 < n_c \leq 50$ in the first loading group, since the test data in this range are on or above the baseline (range). Definite evidence of acceleration is seen as n_c approaches 50. At $n_c = 1000$, it is obvious that overload retardation occurs because the test data are well below the baseline (range).

To achieve a better view of the overload effect, the crack growth rate data from specimen TH1 and specimen TH2 are plotted in Fig. 36. The average baseline of Eq. (4.15) and a line connecting the average points of the test data are also illustrated in the figure. Figure 37 is the statistical version of Fig. 36. It compares the 90% confidence limits of the population means of the test data from both specimens with the 90% confidence limit baselines of Eqs. (4.17) and (4.19).

From Fig. 36 and Fig.37, the test data gradually rise above the baseline (range) as n_c increases from unity to fifty. In the neighbor-

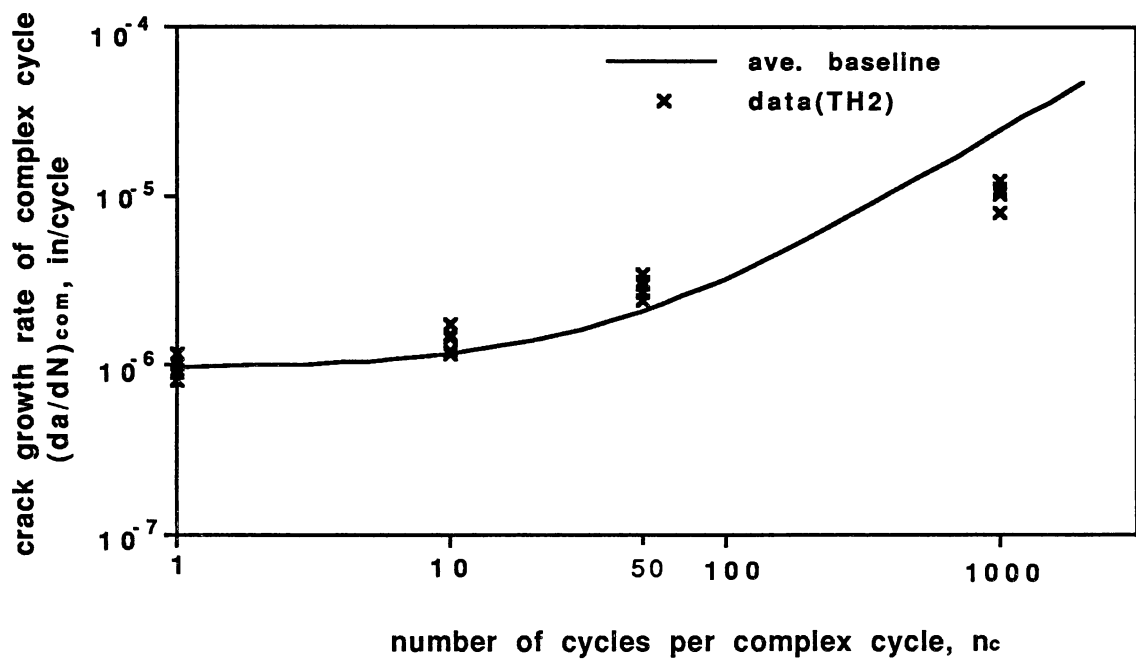


Figure 34. Overload Effect on Crack Growth of Specimen TH2

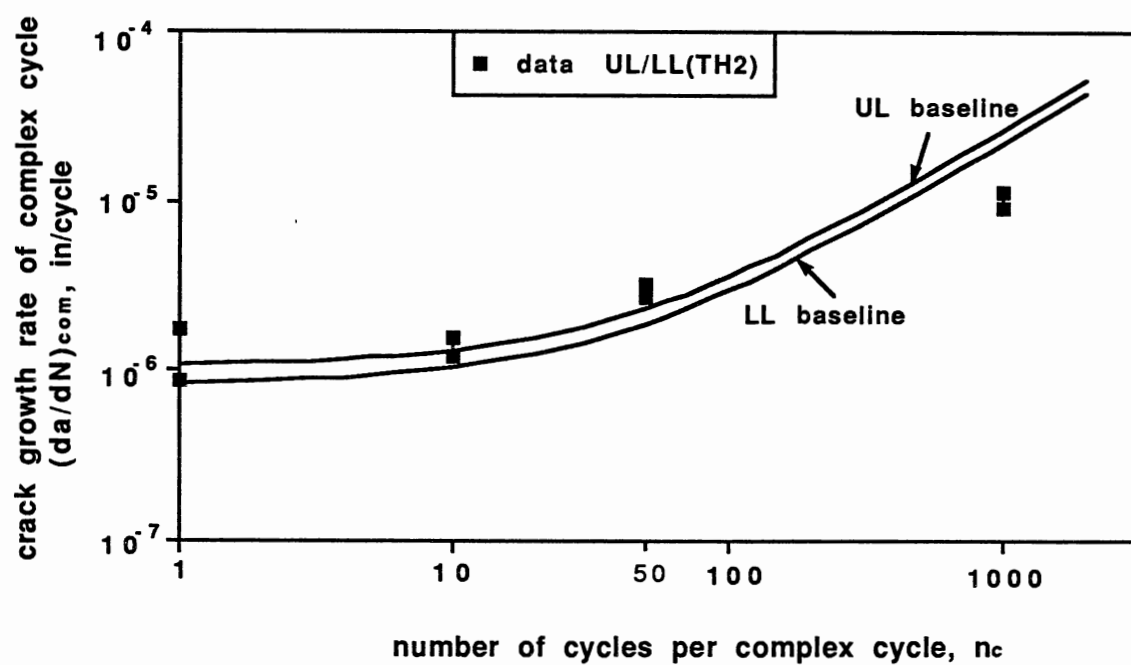


Figure 35. Statistical Demonstration of the Overload Effect With Crack Growth Rate Data From Specimen TH2

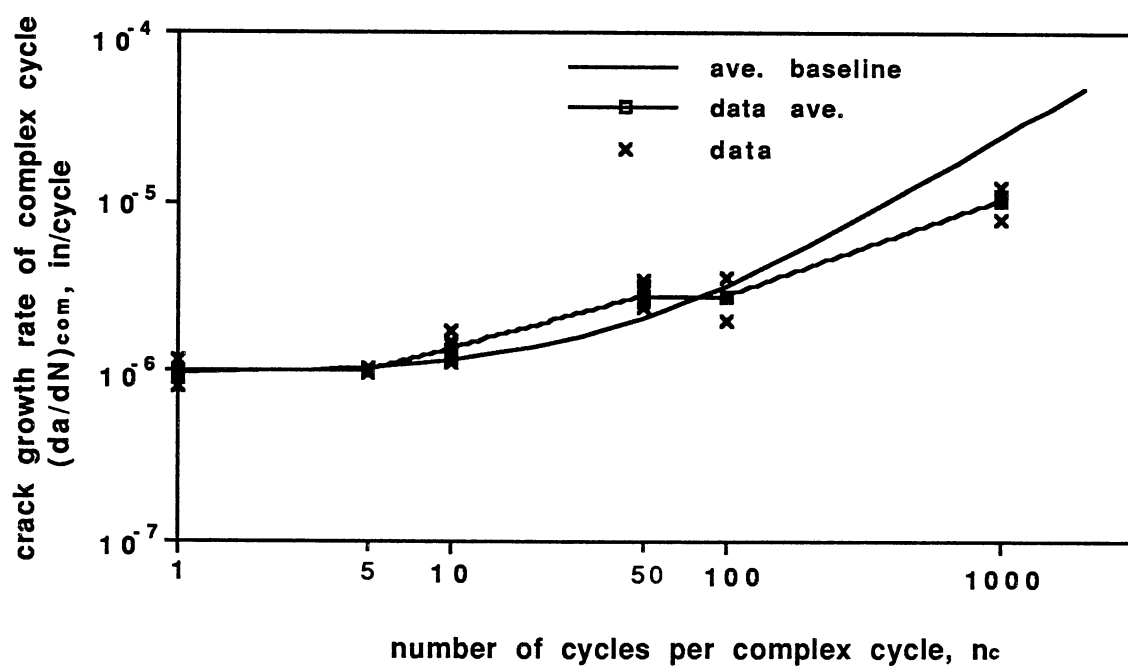


Figure 36. Summary of the Overload Effect on Crack Growth

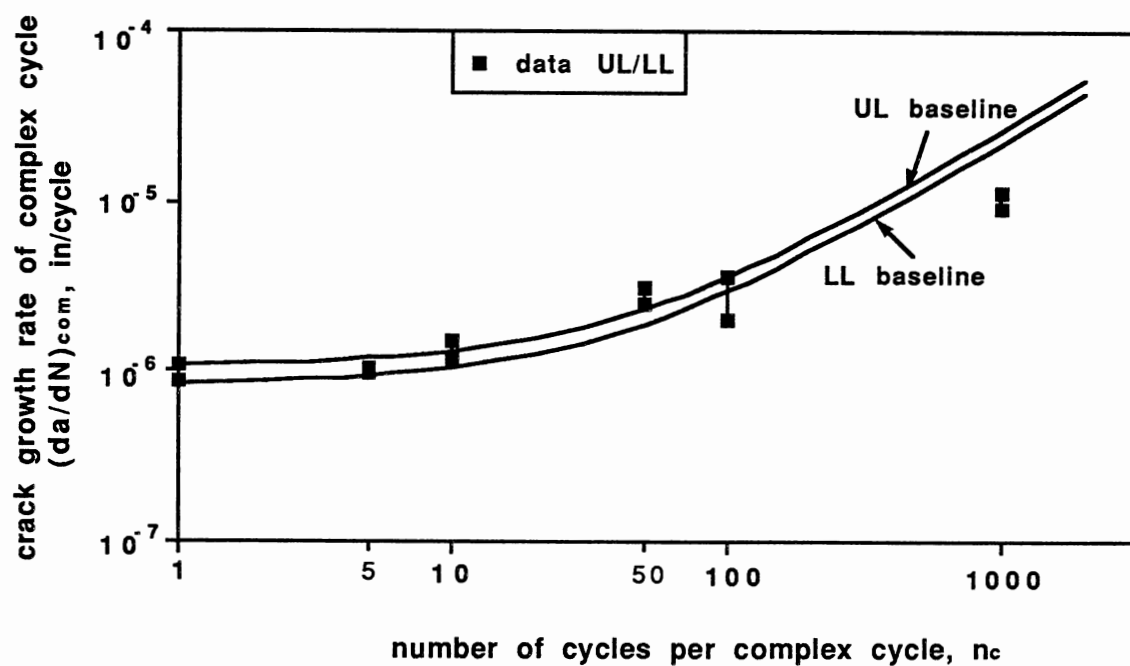


Figure 37. Statistical Demonstration of the Overload Effect With Crack Growth Rate Data From Both Specimens

hood of $n_c = 100$, the test data fall back to the baseline (range). By $n_c = 1000$, the test data have fallen well below the baseline (range). It has been pointed out in the literature review that overload retardation occurs when overload cycles are isolated by a large number of minor cycles. Therefore, it is expected that for $n_c > 1000$, retardation would likely continue to happen.

Based on the data presented in Figs. 32 through 37, it is concluded that under the conditions of the first loading group, overload acceleration occurs in the range of $10 < n_c < 50$; overload retardation occurs in the range of $n_c \geq 100$; and the transition of the overload effect must lie between $n_c = 50$ and $n_c = 100$. In the acceleration and retardation phases, the level of fatigue damage acceleration or retardation is not constant. It appears that the acceleration increases with increasing n_c until it reaches a maximum; then it falls rapidly back to zero at the transition point. Retardation occurs after the transition point and increases with increasing n_c .

Fatigue Damage by Minor Cycles

Two aspects of minor cycle behavior are discussed in this section. One is fatigue damage induced by minor cycles below the threshold mixed with overload cycles above the threshold. This behavior will be referred to as threshold behavior under variable amplitude loadings. The threshold is calculated using the Barsom formula. The other aspect is the minor cycle stress ratio, or R_m , effect. The former is studied using test results from the first loading

group; the latter is studied using test results from the third loading group.

Threshold Behavior. As mentioned in Chapter III, the minor cycles in the first loading group are all below the threshold. So the results of this loading group also provide information about the load interaction effect on the threshold behavior. The transition of the overload effect, observed from the results of this loading group, might be interpreted as follows from the threshold point of view. In the fatigue damage acceleration phase of $10 < n_c < 50$, the acceleration might imply a decrease in the threshold. In the fatigue damage retardation phase of $n_c \geq 100$, the retardation might imply an increase in the threshold. So it appears that the crack growth threshold decreases with increasing n_c for $10 < n_c < 50$ and increases with increasing n_c for $n_c \geq 100$. Here, the minor cycle fatigue damage in the baseline calculation is based upon the experimental results of a previous study [6].

As mentioned in Chapter II, at the threshold point, the crack growth rate is considered to be zero in the traditional concept and is recommended as 10^{-10} m/cycle (3.94×10^{-9} in./cycle) in the ASTM specifications [61]. By assigning these two values to $\left(\frac{da}{dN}\right)_m$ in Eq. (4.1), two baselines, namely, the conventional baseline and the ASTM baseline, can be obtained. By using the $\left(\frac{da}{dN}\right)_o$ value given in Eq. (4.2), the conventional baseline becomes,

$$\left(\frac{da}{dN}\right)_m = 9.742 \times 10^{-7} \text{ in/cycle} \quad (4.21)$$

and the ASTM baseline becomes,

$$\left(\frac{da}{dN}\right)_m = 9.742 \times 10^{-7} + 3.94 \times 10^{-9} n \text{ in/cycle} \quad (4.22)$$

Comparisons between the crack growth rate data for the first loading group from both specimens and these two baselines are given in Fig. 38. It is clear that all test data are above the baselines. This indicates that the threshold loading level calculated using the Barsom formula is not a conservative estimate of the threshold, under all isolated overload spectra in the first loading group, from both traditional concept and the ASTM recommendation. This behavior might be interpreted as a decreasing threshold due to the presence of the overload cycles.

Minor Cycle Stress Ratio (R_m) Effect. In the third loading group, the minor cycles are positioned "bottom," "middle," and "top" with respect to the overload cycles, as shown in Fig. 13. For each position, the minor cycle stress ratio has a different value. The crack growth rate data of the third loading group can be calculated using the raw data in Tables 8 and 9. They are listed in the Table 15. The physical meanings of parameters a , $\frac{da}{dN}$, and $\left(\frac{da}{dN}\right)_{com}$ are the same as those in Table 10. The parameter $\left(\frac{da}{dN}\right)_{com}$ is the average of the $\left(\frac{da}{dN}\right)_{com}$ data available for each type of complex cycle.

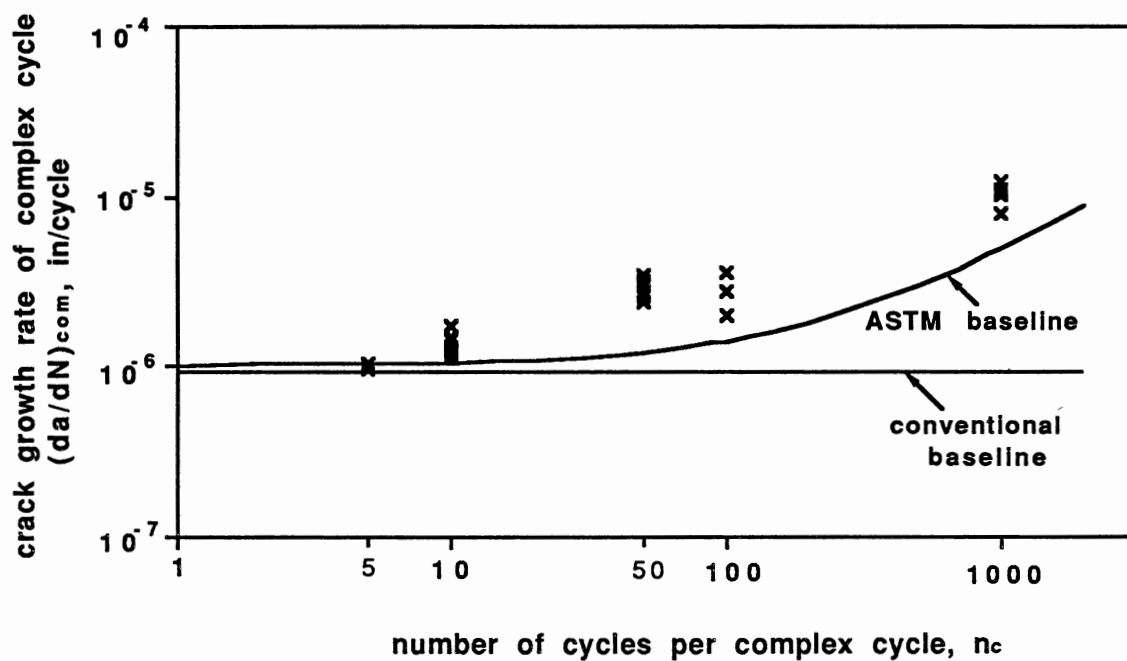


Figure 38. Fatigue Damage Evaluations using the Conventional and ASTM Baselines

TABLE 15
CRACK GROWTH DATA OF LOADING GROUP THREE

minor cycle stress ratio R_m	crack length a (in)	crack growth rate		
		$\frac{da}{dN}$ (10^{-7} in/cyc)	$\left(\frac{da}{dN}\right)_{com}$ (10^{-6} in/cyc)	$\left(\frac{da}{dN}\right)_{com}$ (10^{-6} in/cyc)
0.7 (top)	3.33480	1.857	1.857	2.3116
	3.36500	2.073	2.073	
	3.39533	2.663	2.663	
	3.42553	2.210	2.210	
	3.44960	2.755	2.755	
0.6 (middle)	3.62748	1.600	1.600	1.991
	3.66035	1.700	1.700	
	3.68595	2.325	2.325	
	3.70658	2.338	2.338	
0.3 (bottom)	3.23500	1.254	1.254	1.335
	3.25500	1.108	1.108	
	3.27470	1.322	1.322	
	3.87725	1.200	1.200	
	3.90323	1.160	1.160	
	3.92480	1.488	1.488	
	3.94803	1.712	1.712	
	3.97163	1.434	1.434	

The complex cycle crack growth rate data in Table 10 are plotted in Fig. 39 with the horizontal axis representing the minor cycle stress ratio. A line connecting the average point of the test data corresponding to each R_m value is also drawn in the figure. The horizontal line represents the level of the average crack growth rate under constant amplitude loading conditions (i.e., loading group one, $n = 0$). The average crack growth rate has been given by Eq. (4.2).

It is clear from Fig. 39 that all of the minor cycles in the third loading group are damaging, since the test data are all above the horizontal line. Similar to that reported in Refs. [34, 93], Figure 39 shows that the complex cycle crack growth rate increases when the minor cycle stress ratio increases. The increased fatigue damage under a higher R_m can be attributed to the increased minor cycle mean stress. Furthermore, the data average line is basically linear in the double log coordinate system.

Quantitatively, when the minor cycle position changed from the bottom to the top with respect to the overload cycles (i.e., R_m increases from 0.3 to 0.7), the average complex cycle crack growth rate increased by 65%. This indicates that the minor cycle stress ratio does have an influence on fatigue damage, but the resulting variation in the complex cycle crack growth rate is smaller than the variation in R_m .

Precision of the Crack Growth Rate Data

Effect of Crack Increment between Load Sheddings. In Chapter III, it has been shown that to achieve a desired ΔK precision in a

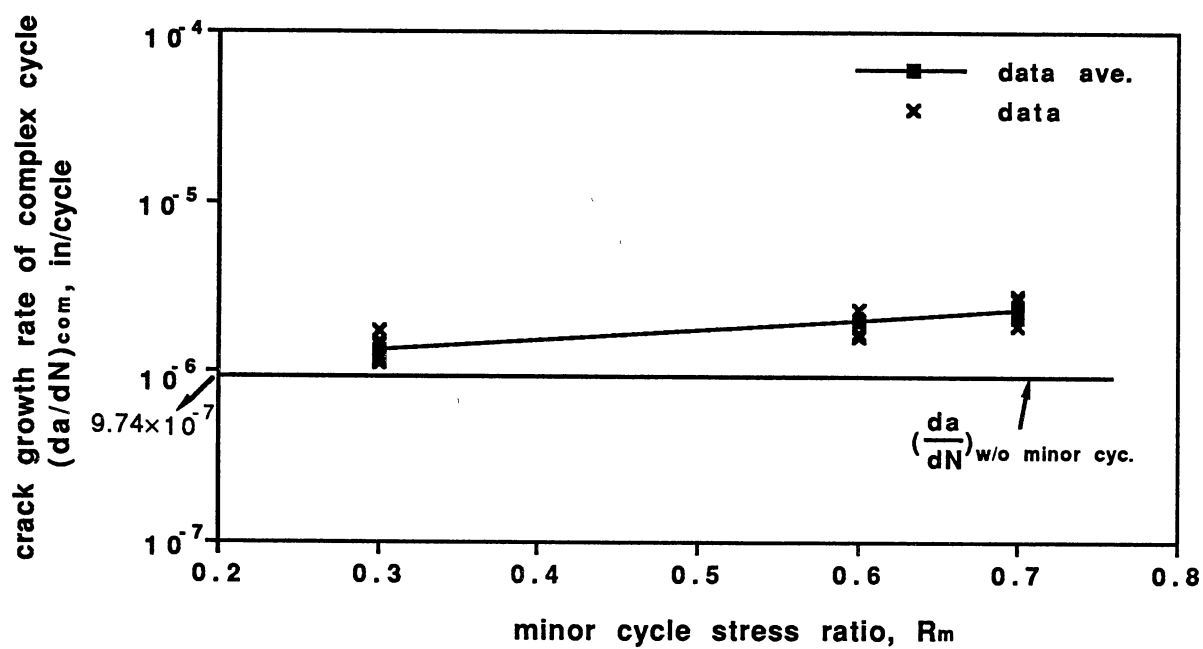


Figure 39. Minor Cycle Stress Ratio Effect on Crack Growth

constant ΔK test, the crack increment between load sheddings should be carefully selected. In fact, the crack increment between load sheddings affects not only the precision of the stress intensity range, but also the precision of the crack growth rate. This can be appreciated from the following derivation.

The effect of the crack increment between load sheddings on the crack growth rate can be reflected by the partial derivative of the crack growth rate with respect to the crack length, $\frac{\partial(\frac{da}{dN})}{\partial a}$. The parameter $\frac{\partial(\frac{da}{dN})}{\partial a}$ can be expressed as,

$$\frac{\partial(\frac{da}{dN})}{\partial a} = \frac{\partial(\frac{da}{dN})}{\partial(\Delta K)} \frac{\partial(\Delta K)}{\partial a} \quad (4.23)$$

According to the Paris law,

$$\frac{da}{dN} = C (\Delta K)^m \quad (4.24)$$

results in,

$$\frac{\partial(\frac{da}{dN})}{\partial(\Delta K)} = C m (\Delta K)^{m-1} \quad (4.25)$$

Combining Eqs. (4.23) through (4.25) leads to,

$$\frac{1}{\left(\frac{da}{dN}\right)} \frac{\partial\left(\frac{da}{dN}\right)}{\partial(a)} = \frac{C m(\Delta K)^{m-1}}{C (\Delta K)^m} \frac{\partial(\Delta K)}{\partial(a)} = m \frac{1}{\Delta K} \frac{\partial(\Delta K)}{\partial(a)} \quad (4.26)$$

When the crack increment between load sheddings is Δa_{max} , the resulting fluctuation of the crack growth rate, denoted as ψ , is,

$$\begin{aligned} \psi &= \frac{1}{\left(\frac{da}{dN}\right)} \frac{\partial\left(\frac{da}{dN}\right)}{\partial(a)} (\Delta a_{max}) \times 100\% \\ &= m \frac{1}{\Delta K} \frac{\partial(\Delta K)}{\partial(a)} (\Delta a_{max}) \times 100\% \end{aligned} \quad (4.27)$$

Recall that in Chapter III, the ΔK fluctuation resulting from Δa_{max} was defined as ξ and expressed as,

$$\begin{aligned} \xi &= \left(\frac{1}{\Delta K} \frac{\partial(\Delta K)}{\partial a} \right) (\Delta a_{max}) \times 100\% \\ &= \frac{\Delta a_{max}}{W(1-\alpha)(2+\alpha)} \frac{Q(\alpha)}{H(\alpha)} \times 100\% \end{aligned} \quad (3.9)$$

where $Q(\alpha)$ and $H(\alpha)$ are given by Eqs. (3.3) and (3.7), respectively. Substituting Eq. (3.9) into Eq. (4.27) yields,

$$\psi = \frac{m \Delta a_{max}}{W(1-\alpha)(2+\alpha)} \frac{Q(\alpha)}{H(\alpha)} \times 100\% \quad (4.28)$$

and ψ is related to ξ by

$$\psi = m \xi \quad (4.29)$$

Equation (4.28) shows clearly that the precision of the crack growth rate in a constant ΔK test is dependent upon the crack increment between load sheddings. A higher crack increment results in a lower precision of the crack growth rate. Furthermore, it is also shown by Eq. (4.29) that for a given crack increment between load sheddings, the fluctuation of the crack growth rate is equal to m times the ΔK fluctuation, where the parameter m is a material constant.

For the specimen material, A588 steel, m is about 3.3 [6]. As discussed in Chapter III, the ΔK fluctuation resulting from the crack increment between load sheddings is kept within 2%. So, according to Eq. (4.29), the maximum fluctuation of the crack growth rate should be 6.6%, which is an acceptable number.

For the example from previous research [68] discussed in the section on ΔK precision, the ΔK fluctuation was up to 11%; the material used was 2024 aluminum. According to Ref.[3], the material constant m of 2024 aluminum is four. Therefore, the fluctuation of the crack growth rate resulting from the crack increment between load sheddings can be up to 44%, which is an unsatisfactorily large number.

The discussion on the precisions of the stress intensity range and the crack growth rate in a constant ΔK test in this dissertation has shown the importance of load shedding design. Equations (3.9)

and (4.26) can be used to study the precision of ΔK and $\frac{da}{dN}$, and to design load sheddings in a constant ΔK test on compact tension specimens. The approach, in which these two equations are derived, can be used to derive similar formulas for other types of specimens.

Effect of Crack Length. The crack growth rate data presented so far were obtained at different crack lengths. To evaluate the effect of the crack length on the crack growth rate, the constant- ΔK loading in the fourth loading group was applied at several different crack lengths. Approximately thirty crack growth data were taken. These data are presented in Table 16. The table also lists the type of loading pins used for later discussion on the loading pin effect on the crack growth rate.

The crack growth rate vs. crack length data in Table 16 are plotted in Fig. 40. It is clear that all data points are distributed along a horizontal line. No significant variation of the crack growth rate data in response to variations in the crack length is observed. Therefore, it can be concluded that the crack length has no influence on the crack growth rate. The crack growth rate data of the first three loading groups are valid at any crack length. This conclusion is in line with a previous observation as well [94]. From Fig. 40, it is also noted that the data points from specimen TH1 and those from specimen TH2 have a similar distribution along the horizontal line. Therefore, the results from both specimens are compatible.

TABLE 16
CRACK GROWTH DATA OF LOADING GROUP FOUR

Specimen TH1			Specimen TH2		
Crack Length a (in.)	Crack Growth Rate da/dN (10^{-7} in/cyc)	loading pins	Crack Length a (in.)	Crack Growth Rate da/dN (10^{-7} in/cyc)	loading pins
2.88343	1.668	metal	2.68185	1.842	plastic
2.91403	2.046	plastic	2.70703	1.719	plastic
2.94108	1.405	plastic	3.01770	2.460	plastic
3.15508	2.177	metal	3.04125	2.002	plastic
3.18185	1.793	plastic	3.28093	2.125	plastic
3.20930	1.691	plastic	3.30628	2.223	plastic
3.38575	1.889	metal	3.57703	1.774	plastic
3.41420	1.480	plastic	3.59865	1.761	plastic
3.44043	1.989	plastic	3.82570	1.616	plastic
3.60133	1.710	metal	3.85060	1.464	plastic
3.62268	1.633	plastic	4.09605	1.925	plastic
3.65000	1.722	plastic	4.12003	1.579	plastic
3.96485	2.035	metal	4.45723	1.750	metal
3.99338	1.924	metal	4.48705	1.912	metal

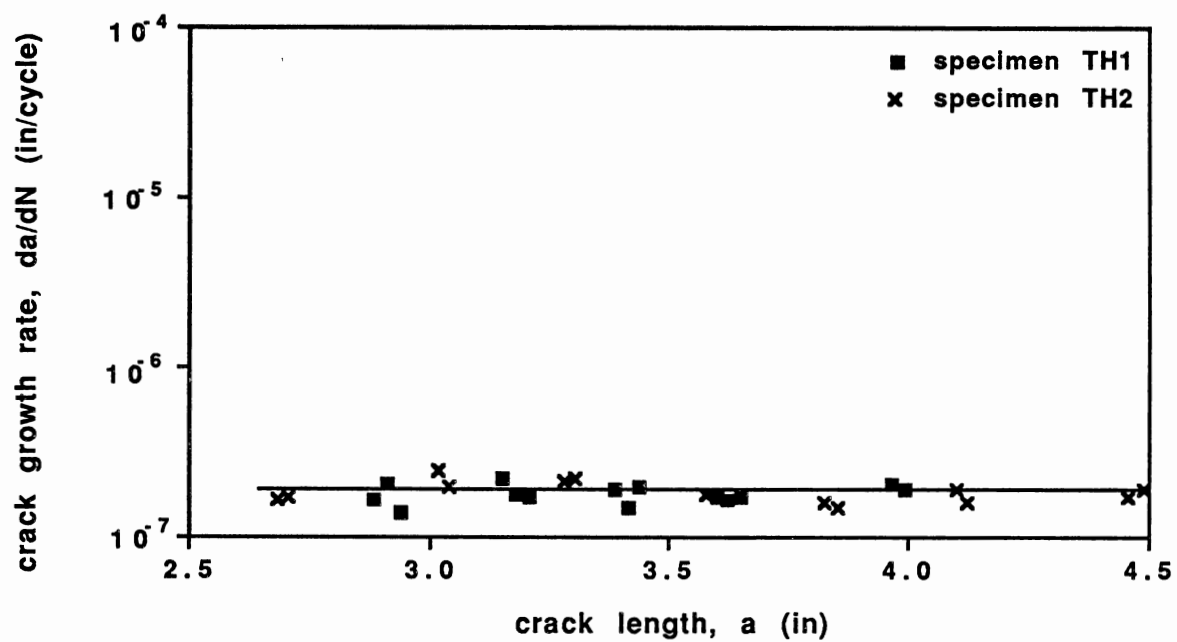


Figure 40. Effect of Crack Length on Crack Growth

Effect of Loading Pins. As mentioned in Chapter III, for the purpose of noise isolation, a pair of plastic loading pins instead of conventional metal pins are employed for most of the formal tests in this research. With the data in the Table 16, a comparison between the crack growth rate data obtained with plastic pins and those obtained with metal pins is shown in Fig. 41.

It is observed that the plastic pin data and the metal pin data are mixed together, and there is no indication of any obvious difference between the two groups of data. Therefore, the type of loading pin dose not have an influence on the crack growth rate.

Acoustic Emission

Acoustic emissions were monitored for the first and third groups of loading applied to specimen TH2. It was observed that the AE signals were intermittent in nature. Table 17 is a summary of the AE test data. The AE terms such as *Event*, *Count*, *Energy (Count)*, and *Amplitude* in the table have been defined in Chapter II. The sum of each parameter was calculated by adding up the measurements of the parameter for all events recorded during the period of measurement. In the following, the characteristics of acoustic emission from fatigue testing and the limitation of AE sensing in fatigue study will be discussed according to the experimental observations. The threshold behavior and the minor cycle stress ratio effect will be examined again using the acoustic emission data.

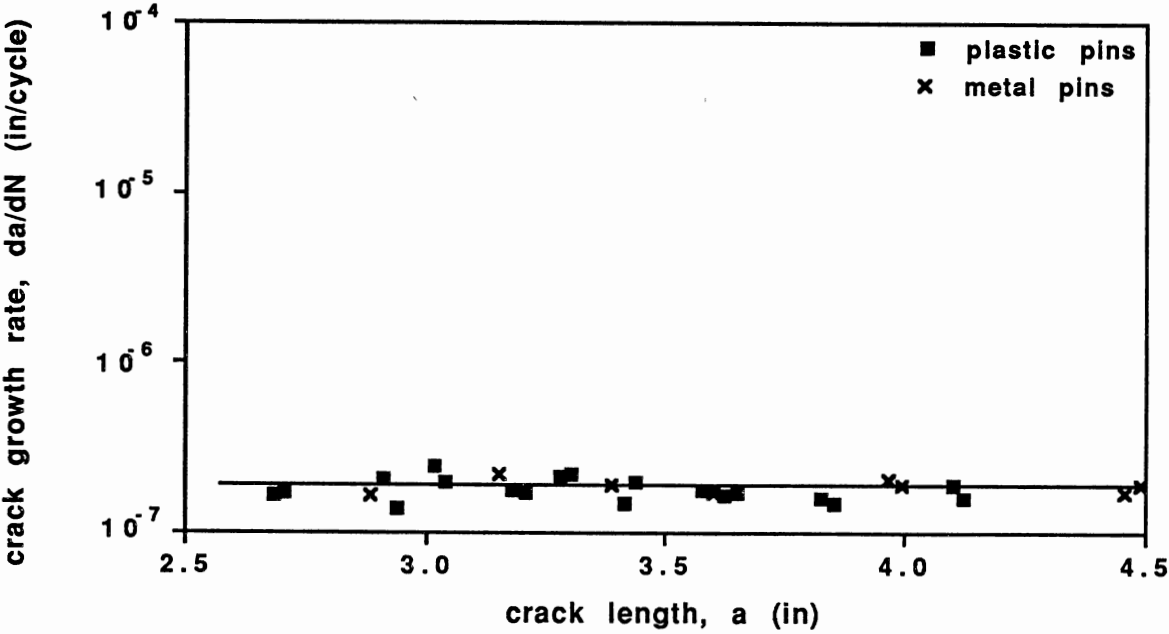


Figure 41. Effect of Loading Pins on Crack Growth

TABLE 17
SUMMARY OF AE TEST DATA

Cycles Applied (10 ² cycles)	Test Data				Loading	
	Event-Sum P _s (times)	Count-Sum C _s (times)	Energy-Sum E _s (energy counts)	Amplitude -Sum A _s (dB)	Group	n
5187	77	77	395	1235	1	49
2845	44	44	234	706		
4440	141	141	736	2264		
4991	85	85	638	1378		
5258	96	96	739	1283		
186	19	19	109	301	1	0
221	14	14	94	259		
306	40	40	207	636		
271	42	42	216	669		
219	30	30	150	480		
1723	38	41	207	624	3 (top)	9
1370	43	43	210	678		
1211	75	75	378	1091		
1274	58	68	371	1063		
726	17	23	103	309	3 (middle)	9
2178	56	56	309	852		
1818	107	107	547	1569		
873	17	17	89	269		
896	22	22	120	314	3 (bottom)	9
2508	39	39	208	624		
1883	80	80	429	1260		
1431	31	35	163	521		
1469	17	17	97	282		
1538	31	33	168	489	1	999
19640	462	462	1907	5028		
29293	274	274	1602	2692		
41873	456	494	3233	5778		
27963	338	338	2500	6068		
33429	260	260	1254	3015		

Intermittent Nature of AE Signals

By comparing the first two columns in Table 17, it is seen that the number of the events recorded is always much smaller than the number of loading cycles applied. This fact indicates that measurable acoustic emission signals do not occur corresponding to every loading cycle, even for loading cycles of the same size. In other words, acoustic emission signals from fatigue testing is of an intermittent nature. This observation is in agreement with some previous AE studies [66, 68]. It is the intermittent nature that limits extensive application of AE sensing in fatigue study.

Similar intermittence exists in crack growth. In general, the distance between atoms is at a magnitude of $10^{-10} m$ [103]. But the crack growth rate obtained macroscopically can be even below such a value [104, 105]. If crack growth is a continuous process, it is implied that the crack growth could proceed through a small distance among atoms within one molecule during the time period of one loading cycle. In fact, this is not true. Therefore, crack growth may not be a continuous process. The intermittence of crack growth was experimentally observed in a previous study [104]. In that study, a specimen was placed on a special cyclic loading stage inside a scanning electron microscope. It was observed that the crack tip moved once every several thousand loading cycles at an intermediate loading level.

The intermittent nature of acoustic emission signals and crack growth is one of the major obstacles to examining fatigue damage

induced by each loading cycle, which could lead to a better understanding of the fatigue damage mechanisms under variable-amplitude loading conditions.

Threshold Behavior

The threshold behavior discussed in the previous section can also be examined using the acoustic emission results from the first loading group. The results are listed in Table 18. Parameters *Event-Rate*, *Count-Rate*, *Energy-Rate* and *Amplitude-Rate* in the table are the parameters of the complex cycle. They are calculated from the data in Table 17 using the following equations,

$$Event-Rate = (Event-Sum)/(N/n_c)$$

$$Count-Rate = (Count-Sum)/(N/n_c)$$

$$Energy-Rate = (Energy-Sum)/(N/n_c)$$

$$Amplitude-Rate = (Amplitude-Sum)/(N/n_c)$$

The *rate-series* of parameters are more informative than the *sum-series* of parameters, because they are less dependent upon the number of loading cycles measured.

As mentioned in Chapter II, the combination of parameters *Count* and *Amplitude* is a good representation of the intensity of AE signals. Thus, the data of *Count-Rate* and *Amplitude-Rate* are

TABLE 18
AE RESULTS OF LOADING GROUP ONE

Cycles per Complex Cycle n_c	Event-Rate $P_s n_c / N$	Count-Rate $C_s n_c / N$	Energy-Rate $E_s n_c / N$	Amplitude -Rate $A_s n_c / N$
	(10^{-3} times/ com-cyc)	(10^{-3} times/ com-cyc)	(10^{-3} energy counts/ com-cyc)	(10^{-2} dB/ com-cyc)
1	1.02	1.02	5.86	1.62
	.624	.624	4.25	1.17
	1.31	1.31	6.76	2.08
	1.55	1.55	7.97	2.47
	1.37	1.37	6.85	2.19
10	1.56	1.56	8.30	2.49
	4.25	4.25	22.8	6.69
	2.20	2.45	11.4	3.64
	1.20	1.20	6.80	19.7
	2.03	2.13	10.9	3.18
50	7.42	7.42	3.81	11.9
	7.70	7.70	41.1	12.4
	15.9	15.9	82.9	25.5
	8.56	8.56	63.9	13.8
	9.12	9.12	70.3	12.2
1000	235	235	971	256
	93.7	93.7	547	91.9
	109	118	772	138
	121	121	894	217
	77.8	77.8	375	90.2

plotted together in Fig. 42. Two horizontal lines pass through the average points of the *Count-Rate* data and the *Amplitude-Rate* data of $n_c=1$ loading, respectively. These lines represent the levels of the corresponding parameters when the minor cycles are considered to be not damaging.

Figure 42 shows that the *Count-Rate* and *Amplitude-Rate* data are above their corresponding baseline for $n_c > 1$, and both parameters increase as n_c increases. Therefore, it can be concluded that under the variable-amplitude loading conditions studied in this research, the intensity of the AE signals increases with increasing number of minor cycles between overload cycles, and the minor cycles below the threshold contribute to fatigue damage.

The energy of acoustic emission signal is also a parameter reflecting the signal intensity. The *Energy-Rate* vs. n_c plot is shown in Fig. 43. Similar to Fig. 42, a horizontal line is drawn through the average point of the *Energy-Rate* data of $n_c = 1$, and it represents the *Energy-Rate* level when minor cycles are not damaging. Since the data points for $n_c > 1$ are all above the horizontal line and increase with an increase in n_c , the above conclusion holds.

From the above discussion, it is clear that the acoustic emission test data lead to a conclusion agreeable to the one drawn from the crack growth rate data. Both types of test data have shown that the traditional concept of below-threshold cycles not causing fatigue damage is not valid under variable-amplitude loading conditions.

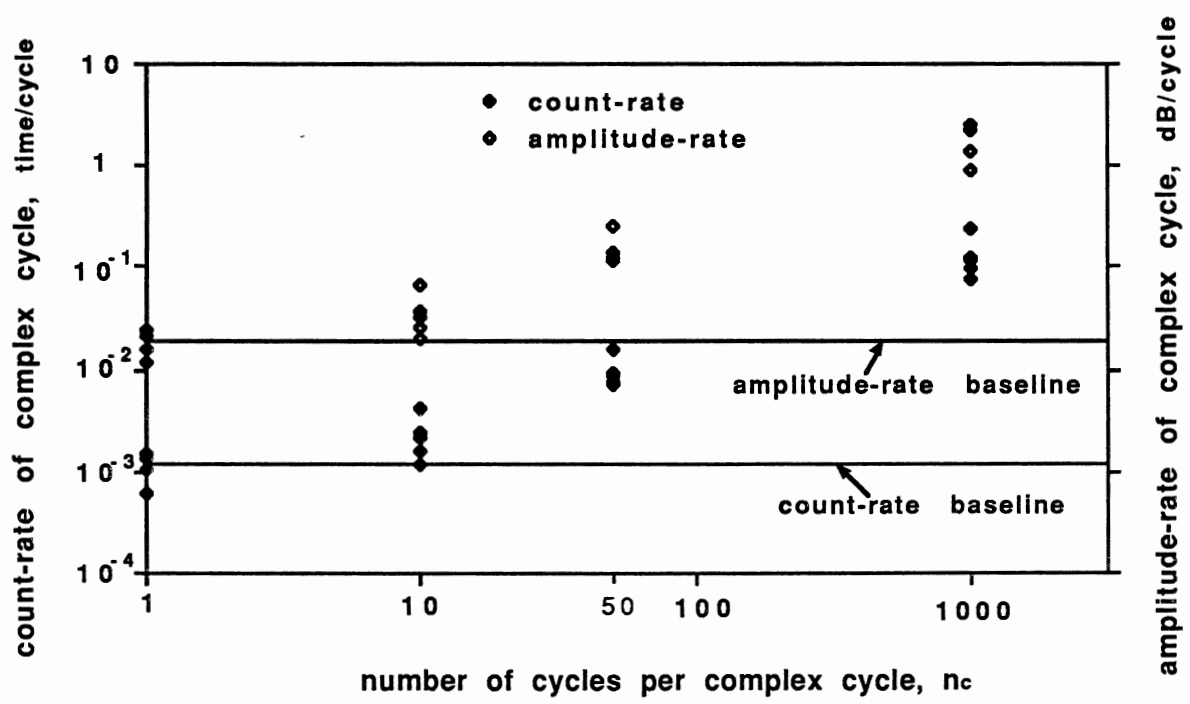


Figure 42. Threshold Behavior Evaluated Using the AE Count and Amplitude Data

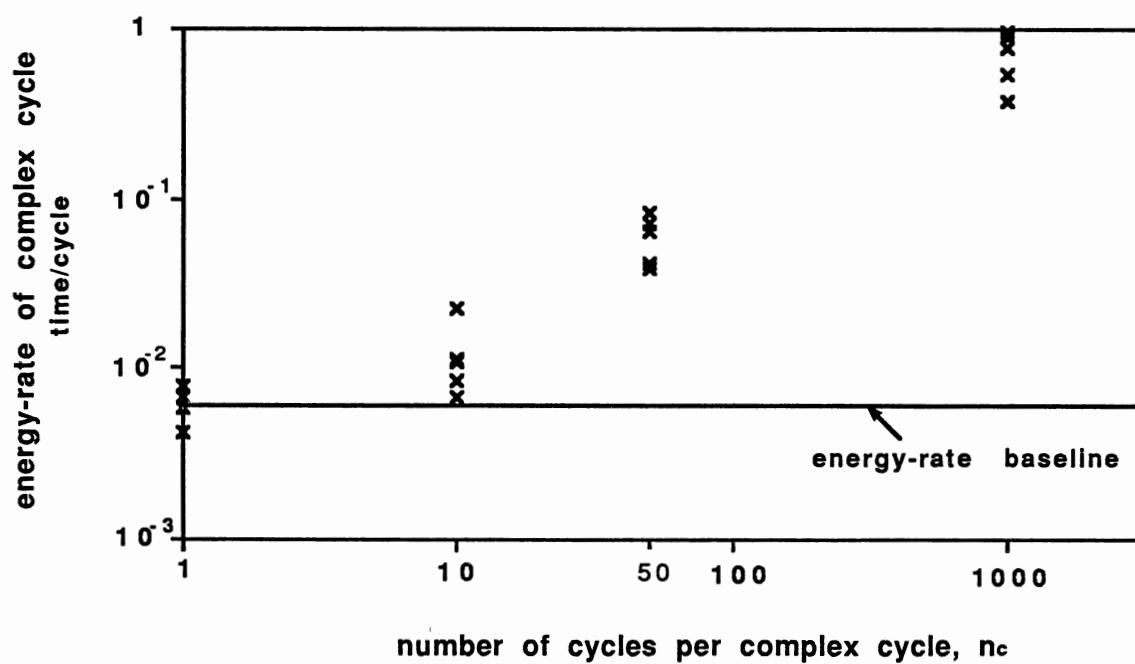


Figure 43. Threshold Behavior Evaluated Using the AE Energy Data

Minor Cycle Stress Ratio Effect

The AE results from the third loading group are presented in Table 19. To show the effect of the minor cycle stress ratio on the major parameters of AE signals, the *Count-Rate* and *Amplitude-Rate* vs. n_c curves, and the *Energy-Rate* vs. n_c curve are plotted in Figs. 44 and 45, respectively. The same horizontal baselines used in Figs. 42 and 43 are also drawn in Fig. 44 and 45, respectively. Here, they represent the level of fatigue damage induced by a complex cycle with no minor cycle.

From Figs. 44 and 45, it is observed that all test data are above the corresponding baselines, and the three AE parameters increase as R_m increases. Therefore, it can be concluded that all minor cycles present cause fatigue damage, and the resulting damage increases as the minor cycle stress ratio increases. Thus, as to the R_m effect, the AE results are consistent with the macrocrack growth results.

CMOD and BFS

In this study, crack mouth opening displacement and back-face strain were monitored under the second group of loading. CMOD was also measured under the first group of loading. In the following sections, the results of crack mouth opening displacement and back face strain measurements will be employed to study crack opening and to discuss the feasibility of using the CMOD and BFS measurements to determine the crack opening stress intensity factor.

TABLE 19
AE RESULTS OF LOADING GROUP THREE

Minor Cycle Stress Ratio	Event-Rate $P_s n_c / N$	Count-Rate $C_s n_c / N$	Energy-Rate $E_s n_c / N$	Amplitude -Rate $A_s n_c / N$
R_m	(10^{-3} times/ com-cyc)	(10^{-3} times/ com-cyc)	(10^{-2} energy counts/ com-cyc)	(10^{-2} dB/ com-cyc)
0.7 (top)	2.23	2.40	1.20	3.62
	3.14	3.14	1.53	4.95
	6.23	6.23	3.12	9.01
	4.56	5.34	2.91	8.34
	2.37	3.16	1.42	4.25
0.6 (middle)	2.55	2.55	1.42	3.91
	5.89	5.89	3.01	8.63
	1.95	1.95	1.02	3.08
	2.41	2.41	1.34	3.51
0.3 (bottom)	1.56	1.56	0.83	2.49
	4.25	4.25	2.28	6.69
	2.20	2.45	1.14	3.64
	1.20	1.20	0.68	1.97
	2.03	2.13	1.09	3.18

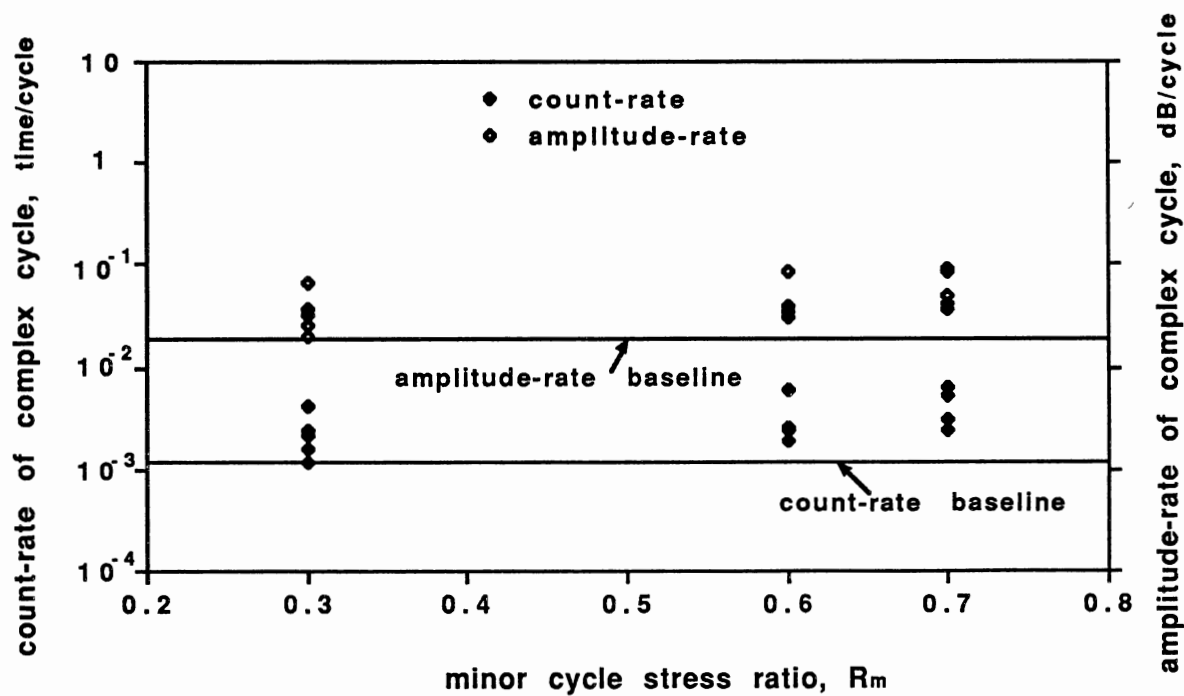


Figure 44. R_m Effects on the AE Count and Amplitude Data

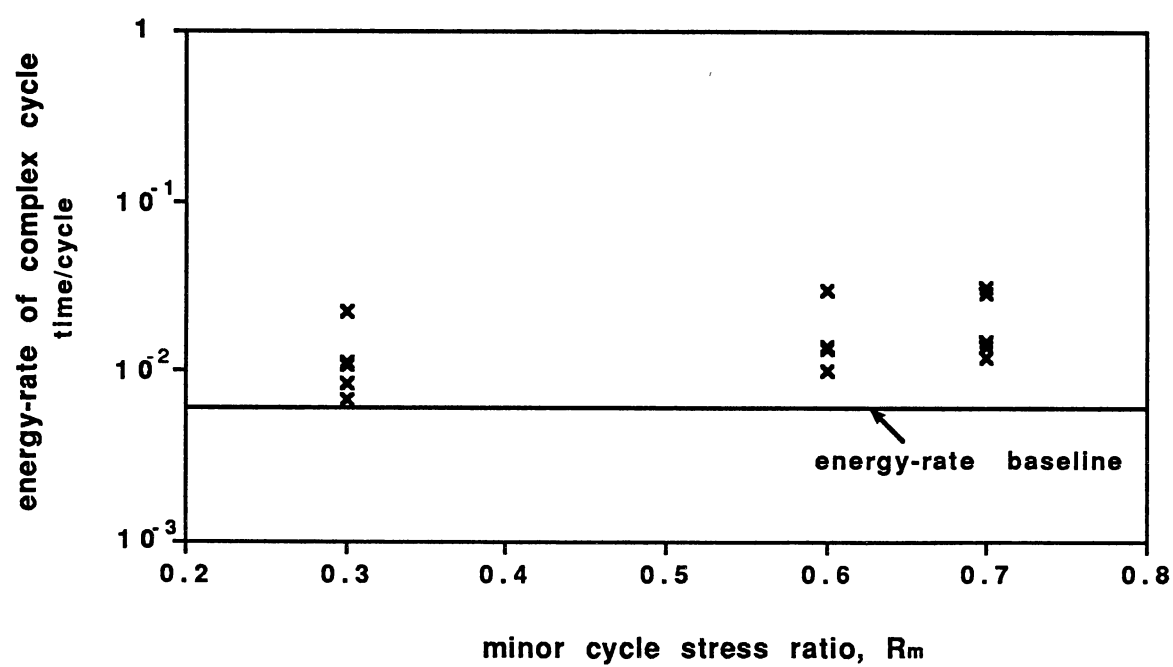


Figure 45. R_m Effect on the AE Energy Data

Crack Opening Observations

In a previous study [82], it was observed that following an isolated overload, the displacements at both the maximum and minimum loads of the minor cycles were increased. The intention of the present testing is to see whether the same behavior occurs after a series of overloads.

For the loading spectrum of $n = 9$ in the first loading group, the CMOD signal recorded is shown in Fig. 46. It is clear that the maximum and the minimum displacements corresponding to the minor cycles remain the same after the first overload as well as the subsequent overloads. The same pattern was observed under other loading spectra of $n \neq 9$ in the first loading group. It seems that the crack is not propped open under the first group of loading. The absence of this behavior is most likely due to the low loading level of the first loading group. This will become clearer from the CMOD and BFS results for loading group two.

Examples of the CMOD and BFS signals for the second loading group are shown in Figs. 47 and 48, respectively. They correspond to the loading spectrum of $n = 9$. These figures show that the maximum and minimum values of the CMOD and BFS signals corresponding to the minor cycles have a step increase after the first overload, which is an indication of the crack being propped open. As mentioned in the section on loading programs, the major difference between the first two groups of loading lies in the loading level. The loading level of the second load group is higher than that of the first.

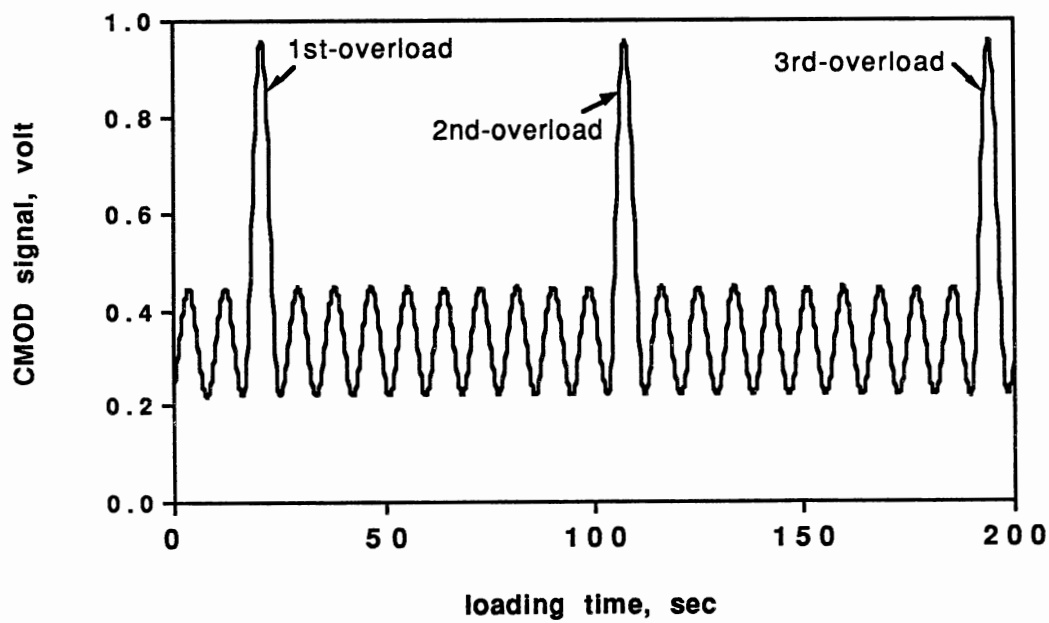


Figure 46. A Typical CMOD Signal From Loading Group One

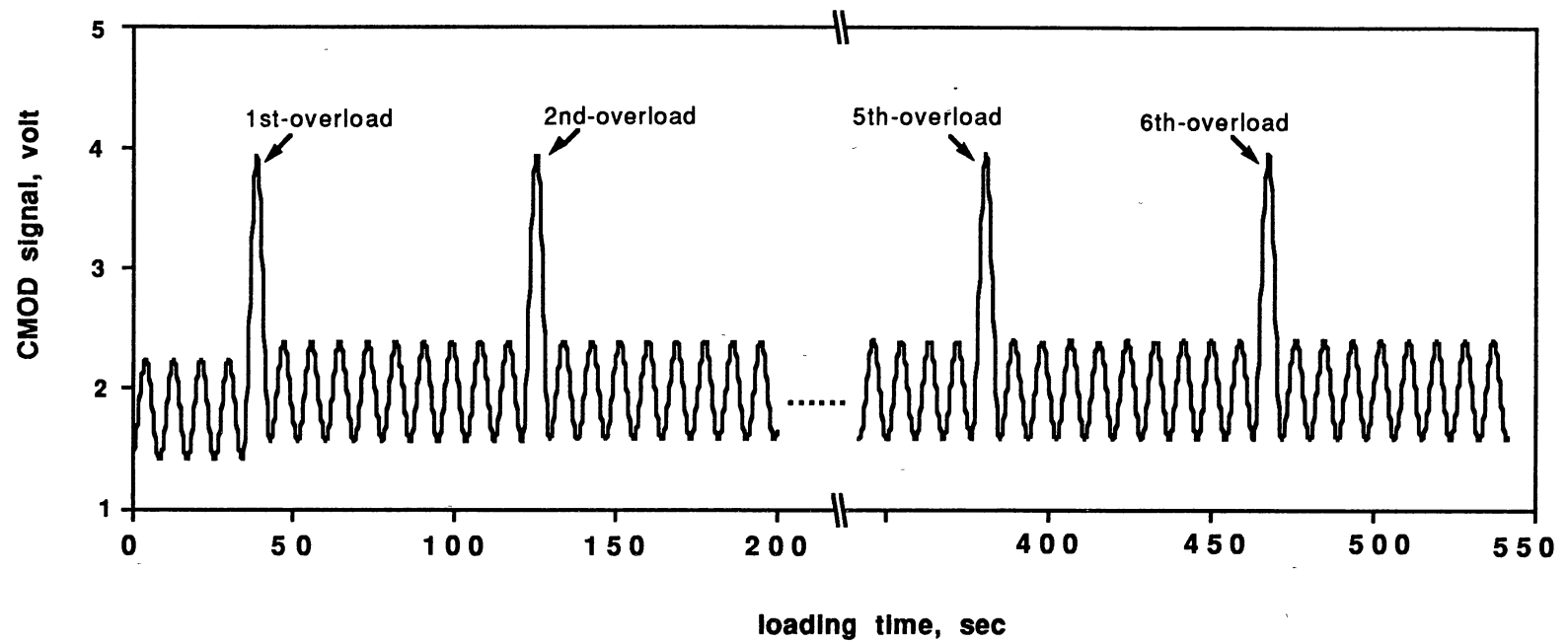


Figure 47. Crack Opening Observed From the CMOD Signal Under Group-Two Loading With $n = 9$

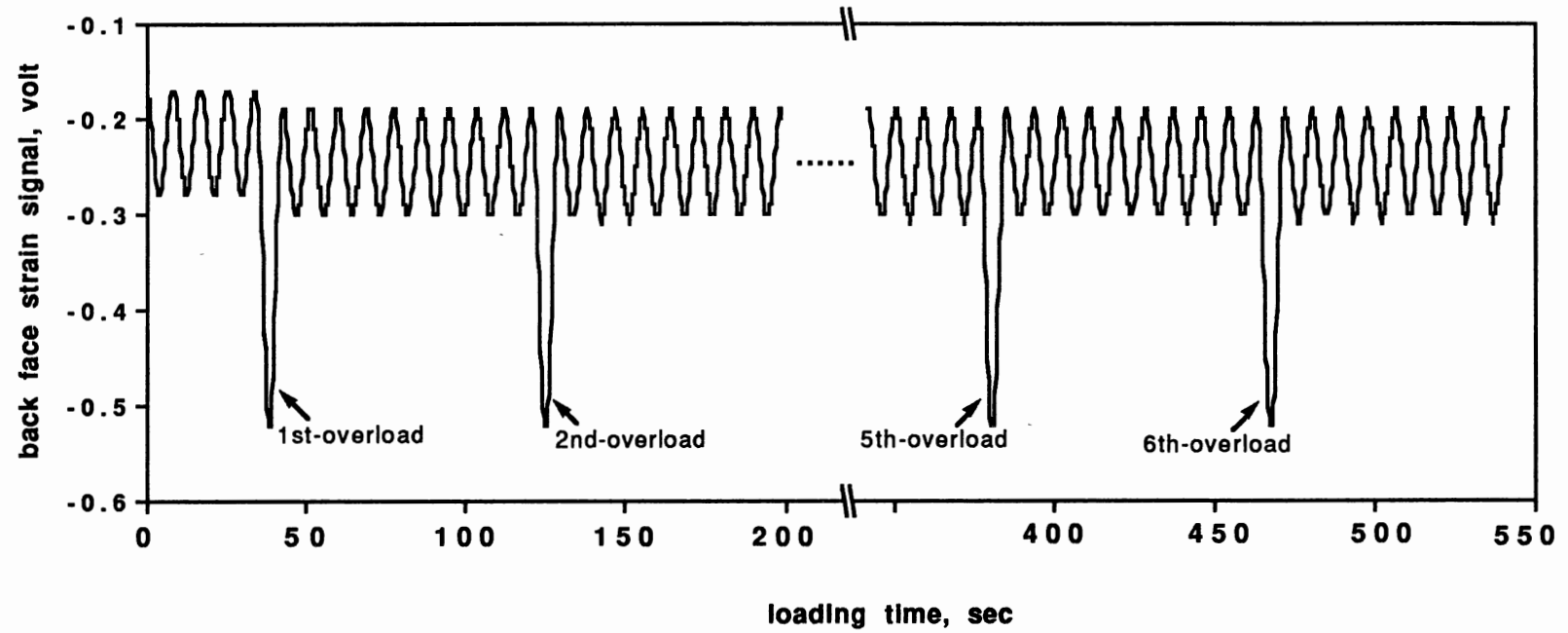


Figure 48. Crack Opening Observed From the BFS Signal Under Group-Two Loading With $n = 9$

From Figs. 47 and 48, it is interesting to observe that the maximum and minimum values of the CMOD and BFS signals of the minor cycle do not have additional step changes after subsequent overloads. In other words, the crack is propped open only after the first overload, not after every overload. The following is a possible explanation of this fact.

When the first overload was acting on the specimen, a large plastic zone formed in front of the crack tip. The plastic deformation propped open the crack at a certain level, which caused a step change in the CMOD and BFS signals after the first overload. The limited number of minor cycles between two overloads usually cannot significantly attenuate the prop effect of the plastic zone. So the prop action remained basically unchanged until the following overload arrived. Since all overloads in the loading spectrum are of the same size, the plastic zones induced by the subsequent overloads are of the same size as that induced by the first overload. The subsequent overloads could not generate a significantly higher level of prop action than that induced by the first overload. Therefore, the CMOD and BFS signals did not experience additional step changes after subsequent overloads. Figure 49 shows that even for a slightly higher number of minor cycles between overloads, such as $n = 49$, the crack opening behavior is similar to the case of $n = 9$ shown in Fig. 48.

The prop opening of the crack is directly related to the interaction between the overloads and the minor cycles. A better understanding of this behavior as well as its dependency upon the

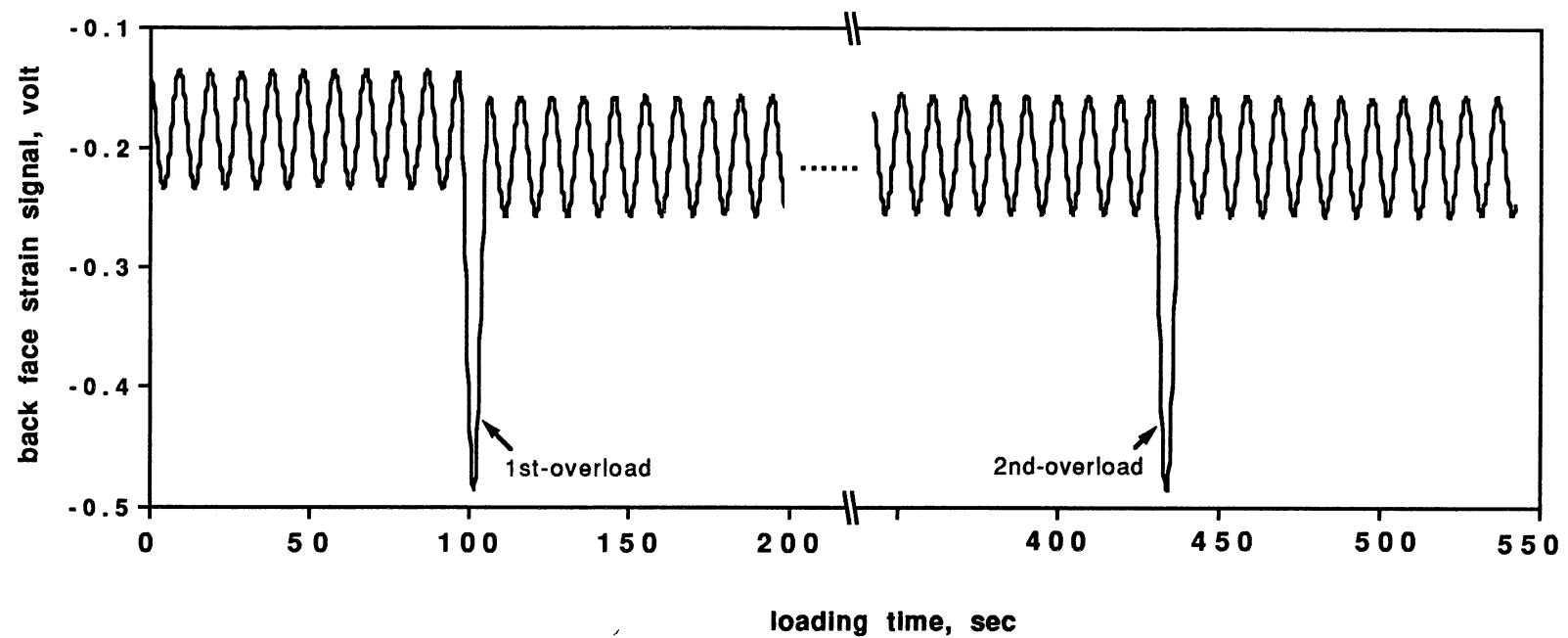


Figure 49. Crack Opening Observed From the BFS Signal Under Group-Two Loading With $n = 49$

loading level and the number of minor cycles between overloads is expected to provide insight to the overload acceleration and retardation study. Further research on this phenomenon is needed.

Feasibility of Determining K_{op}

The crack opening stress intensity factor was used as a parameter to study the overload effect in previous research [44, 55]. As shown in Fig. 7, the crack opening stress intensity factor is determined from the load-displacement curve. It is desired to be able to identify the crack opening stress intensity factor for every loading cycle applied.

In this research, typical load-displacement curves extracted from the CMOD and BFS measurements are shown in Figs. 50 and 51, respectively. Both curves correspond to the rising edge of the first overload in the loading spectrum with $n = 9$ in the second loading group. It is observed that the CMOD curve is basically linear and cannot be used to determine the crack opening stress intensity factor, while the BFS curve has a visible curvature which might be used to determine the crack opening stress intensity factor.

It appears that the BFS measurement is more sensitive than the CMOD measurement where crack opening is concerned. The clip gage technique is not sensitive enough to provide data for calculating K_{op} under the loading conditions used in this research. A similar comment on the clip gage technique is seen in Ref. [82]. The back-face strain technique appears to have the potential for being used to determine K_{op} under the loading conditions studied. Further work

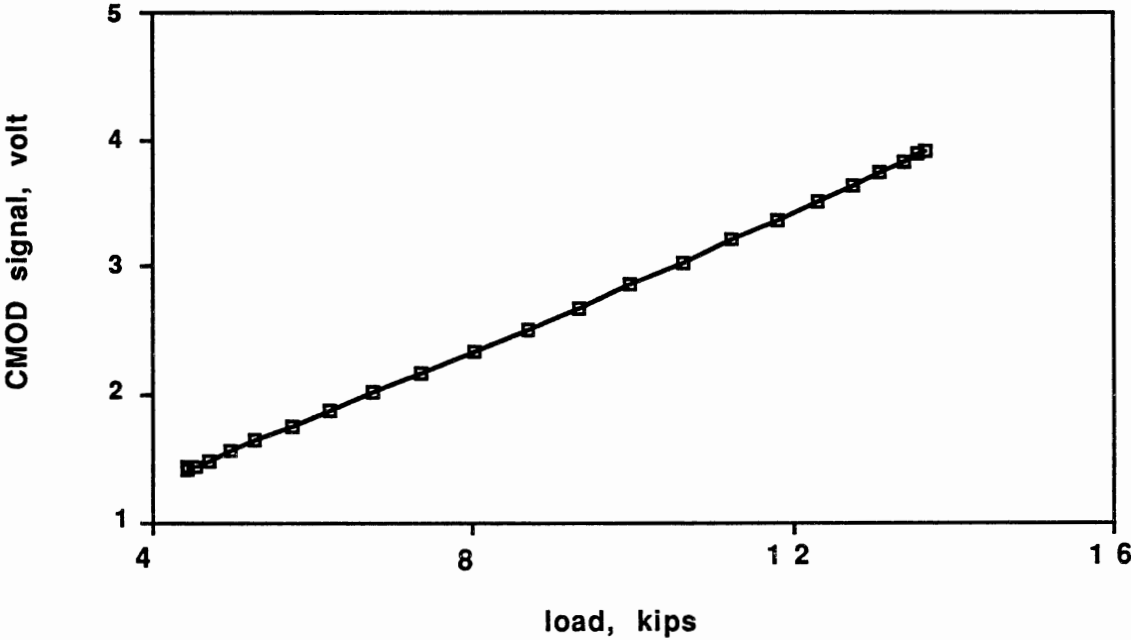


Figure 50. CMOD Vs Load Curve for the First Overload in Group-Two Loading With $n = 9$

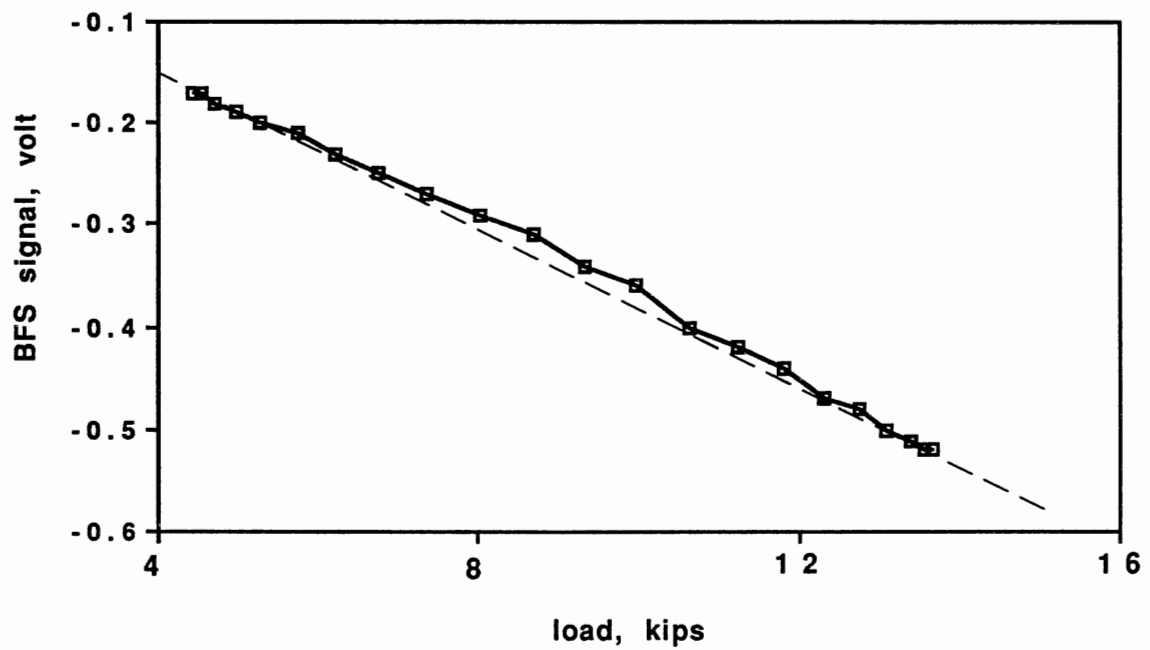


Figure 51. BFS Vs. Load Curve for the First Overload in Group-Two Loading With $n = 9$

on this subject is needed to investigate the crack opening stress intensity factor of every loading cycle and its impact on the overload study.

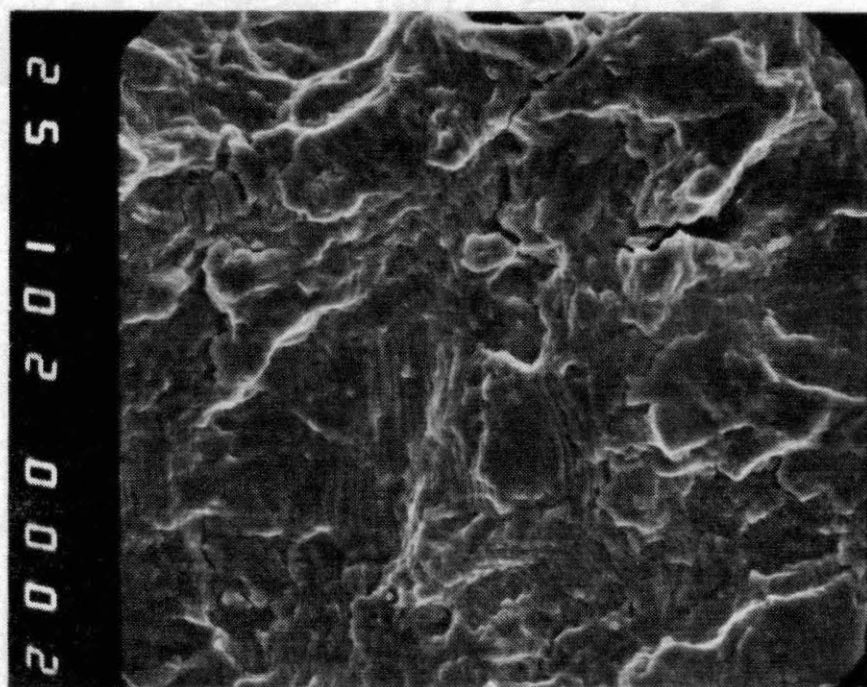
Fatigue Striation

Under the scanning electron microscope, fatigue striations were observed on an area of the crack surface corresponding to a loading of $n = 49$ in the second loading group. The characteristics of the striations and a comparison between the microcrack and macrocrack growth rate data are presented in the following.

Striation Characteristics

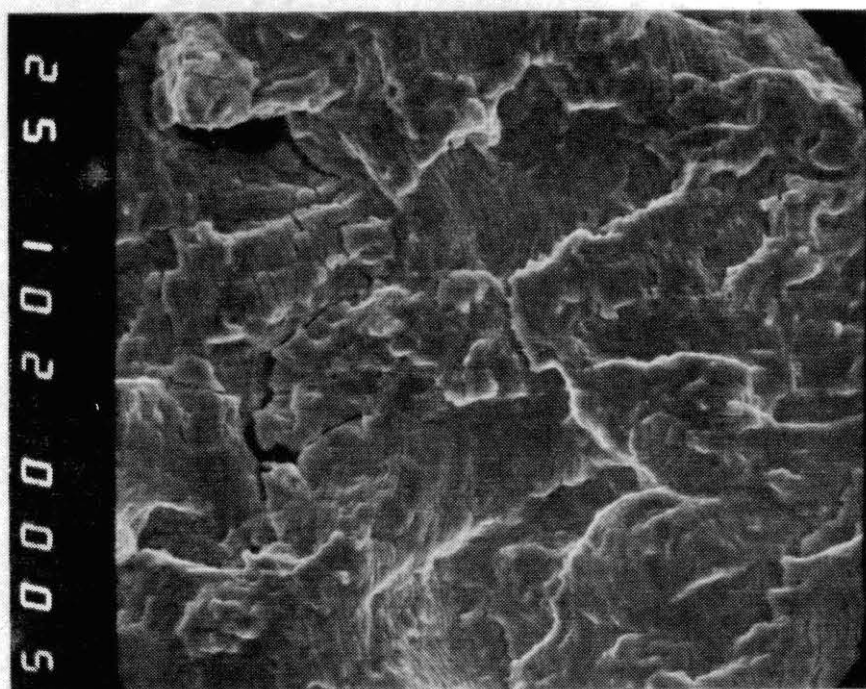
Two striation photos taken at locations #2 and #5 shown in Fig. 29 are presented in Fig. 52 (a) and (b). From the photos, it can be seen that the striations are localized. According to the pattern of the striations, the crack surface can be divided into many small regions. Both the orientation and spacing of the striations vary from region to region. Inside each region, the striation lines are basically parallel to each other and are of the same spacing. These lines form a relatively uniform group.

In general, the striation orientation is perpendicular to the crack growth direction, and the striation spacing represents the crack growth rate. Therefore, each region can be considered as a microcrack of its particular crack growth orientation and speed. The macrocrack growth is the resultant action of all localized microcrack



a) Photo No. 2, 1000×

Figure 52. Examples of the Striations Observed



→
Crack Growth Direction

b) Photo No. 5, 1000×

Figure 52. (Continued)

growths. The localization feature of the striation spacing was also observed in a previous study on 2024-T3 aluminum alloy [87]. It was reported that the microcrack growth rate might vary by a factor of two to four from one region to another.

In this research, the striations observed all correspond to the overload cycles applied. The striations induced by the minor cycles cannot be distinguished even under the SEM. The estimated crack growth rate under loading consisting of only the minor cycles is about 5×10^{-7} in./cycle [6]. The reported SEM resolution is only 10 nm (3.94×10^{-7} in.) [69, 73]. So the limited resolution of the SEM might not allow seeing the minor cycle striations.

Evidence of abrasive damage on the fracture surface was also observed under the SEM. An example is shown in Fig. 53. The photo was taken on a trial specimen. For the loading spectrum applied to the trial specimen, the overload stress ratio was 0.05 and the overload stress intensity range was the same as that in the second loading group. It is clear that the striation lines in two local regions next to the right edge of the photo suffer from severe abrasive damage. Furthermore, it is noted that the striations in Fig. 52 suffer from less abrasive damage than those in Fig. 53. This can be attributed to the higher overload stress ratio ($R_o = 0.3$) adopted in loading group two. A smaller R_o results in more contact between the fractured surfaces, which causes more abrasive damage.

Microcrack and Macrocrack Growth Rates

Since each striation line corresponds to an overload cycle, the

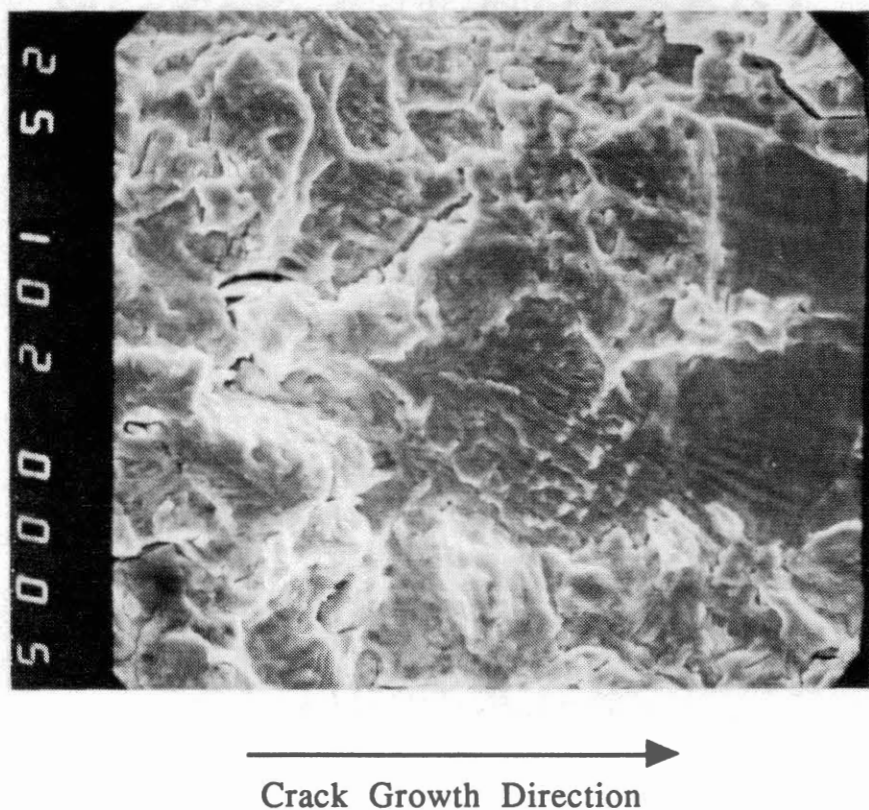


Figure 53. An Example of Evident Abrasive Damage on Fracture Surface (Trial Specimen)

complex cycle crack growth rate, $\left(\frac{da}{dN}\right)_{com}$, is equal to the striation spacing. By measuring the spacings of the striations on each photo, the minor crack growth rate can be determined. The results of such measurements are listed in Table 20. Due to the localized character of the striations, the striation spacings in five to six regions in each photo were measured. Their average is used as the microcrack growth rate in Table 20. As a comparison, Table 21 provides the macro crack growth rate data for crack length from 4.10 to 4.60 inches. Figure 54 is a comparison between the microcrack growth rates and their macrocrack counterparts. It is shown that the two data groups correlate with each other.

Summary of the Results

In the preceding sections of this chapter, all results have been presented and discussed in the sequence of the measurement techniques used. A brief summary of the results in light of the research objectives will be given next. This summary includes the overload effect evaluated using the test data of macrocrack growth, CMOD, BFS, and microcrack growth; the minor cycle damage evaluated using the results of macrocrack growth and acoustic emission; and additional findings obtained during the investigation process.

Overload Effect

The macrocrack growth rate data of loading group one are

TABLE 20
MICRO CRACK GROWTH DATA FOR GROUP-
TWO LOADING WITH $n=49$

Photo No.	2	3	4	5	6	41	421
a(in.)	4.51	4.47	4.39	4.31	4.23	4.40	4.36
(da/dN) _{com} (10 ⁻⁵ in/cyc)	3.17	2.94	3.09	3.38	2.94	3.55	2.85

TABLE 21
MACRO CRACK GROWTH DATA FOR GROUP-
TWO LOADING WITH $n=49$

crack length a (in)	crack growth rate	
	$\frac{da}{dN}$ (10^{-7} in/cyc)	$\left(\frac{da}{dN}\right)_{com}$ (10^{-5} in/cyc)
4.12380	7.858	3.929
4.15003	7.460	3.730
4.17170	6.242	3.121
4.19495	8.170	4.085
4.22233	9.982	4.991
4.24723	8.058	4.029
4.27213	9.958	4.974
4.29843	8.668	4.334
4.32370	9.178	4.589
4.34795	8.858	4.429
4.37028	8.346	4.173
4.39335	8.436	4.218
4.41680	10.63	5.314
4.44030	8.792	4.396
4.46258	8.400	4.200
4.48860	10.69	5.374
4.51598	9.392	4.496

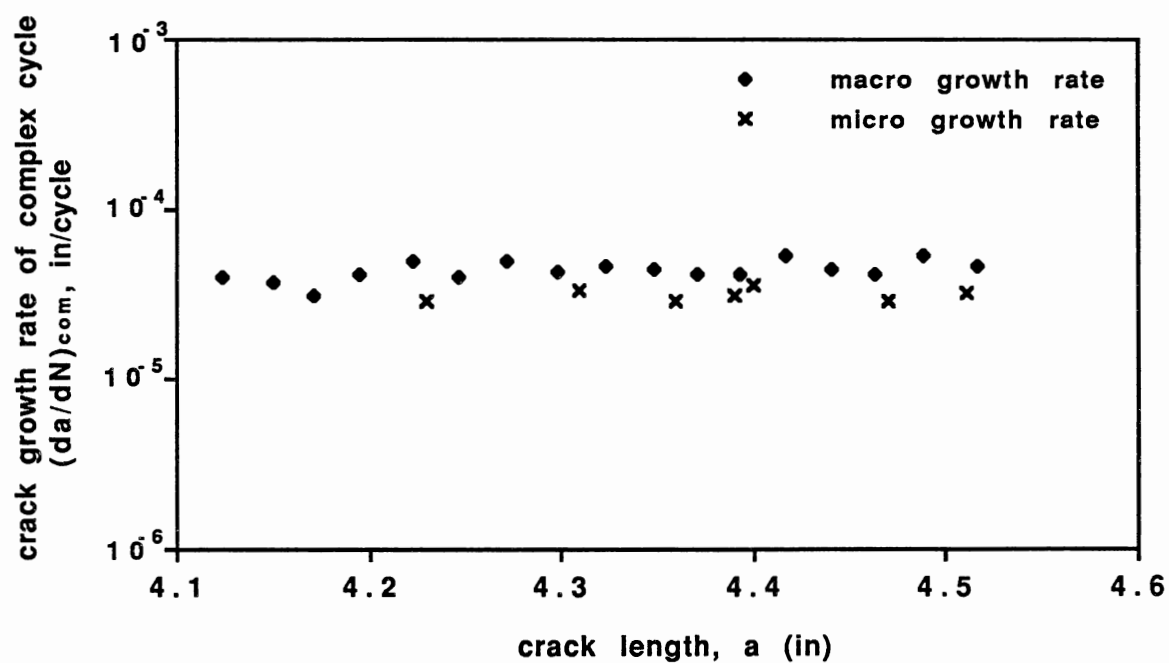


Figure 54. Comparison of the Microcrack and Macrocrack Growth Rate Data From Loading Group Two

compared with an average crack growth rate baseline and a statistical crack growth rate baseline range. The average baseline is based on the non-interaction model. The statistical baseline range is bounded by the upper and lower confidence limit baselines of the population mean of the crack growth rate calculated under the assumption of no load interaction. The comparisons show that the crack growth rate data from the isolated overload programs are on or above the baseline (range) for $10 < n_c < 50$, and below the baseline (range) for $n_c \geq 100$.

It is concluded that under the loading conditions studied, acceleration occurs for $10 < n_c < 50$, retardation occurs for $n_c \geq 100$, and the transition of the overload effect lies between $n_c = 50$ and $n_c = 100$. The level of overload acceleration increases with increasing n_c until it reaches a maximum, then falls rapidly to zero between $n_c = 50$ and $n_c = 100$. After the transition point, the level of retardation increases as n_c increases.

The results of crack mouth opening displacement and back-face strain measurements provide another view of the overload effect. The CMOD and BFS signals from loading group two show a step change in their minor cycle components after the first overload cycle, and no more step change after the subsequent overload cycle. In other words, under the group-two loading conditions, the crack is propped open following the first overload, and then remains unchanged for subsequent overloads. A tentative explanation of this phenomenon has been proposed as follows. The large plastic zone induced by the first overload propped open the crack at a certain

level, which caused a step change in the CMOD and BFS signals after the first overload. Because a small number (e.g., 9 and 49) of the minor cycles between the overloads could not reduce a significant amount of the plastic zone in front of the crack tip, the prop action remained basically the same until the second overload arrived. The second and subsequent overloads maintained the size of the plastic zone at a nearly constant level. So, the CMOD and BFS signals did not experience additional step change.

It was also noted that the loading level had an influence on the extent to which the crack was propped open. The CMOD signal from the first loading group, which has a lower loading level than the second loading group, did not have a step change after the first and the subsequent overload. It seems that the crack is not propped open a significant amount under small loadings.

On the portion of the specimen sample experiencing group-two loading, all striations observed correspond to the overload cycles. This fact indicates that there exists a large difference between overload fatigue damage and minor cycle fatigue damage, whatever the load interaction is. In addition, it has been shown that the complex cycle crack growth rate data calculated using the striation spacing measurements are correlated to the macrocrack crack growth rate data calculated using the traveling microscope measurements.

Fatigue Damage by Minor Cycles

Threshold Behavior. The minor cycles in the first loading group are all below the threshold level calculated using the Barsom

formula. Under such loading, fatigue damage acceleration and retardation observed might imply an increase or a decrease in the threshold. In other words, it seems that the threshold decreases with increasing n_c in the acceleration phase of $10 < n_c < 50$, and increases with increasing n_c in the retardation phase of $n_c \geq 100$. Here, the minor cycle fatigue damage in the baseline calculation is based on the experimental results of a previous study [6].

According to the conventional concept and the ASTM specifications on the crack growth rate at the threshold point, two more baselines for the macrocrack growth rate under the first group of loading were calculated. All macrocrack growth rate data from loading group one have been found to be above the conventional and ASTM baselines. This indicates that the threshold loading level calculated using the Barsom formula is not a conservative estimate of the threshold under all isolated overload spectra in the first loading group, from both the conventional concept and the ASTM recommendation. It seems that the threshold decreases under such loading conditions due to the presence of the overload cycles.

The intensity of the AE signals from the first loading group has been studied in terms of *Count-Rate*, *Energy-Rate* and *Amplitude-Rate*. The averages of the AE data of $n_c = 1$ loading were used as baselines for the three parameters. They represent the AE intensity level when the minor cycles are not damaging. The results show that the AE data for $n_c > 1$ are above their corresponding baselines and each parameter increases as n_c increases. Therefore, it is concluded that under the variable amplitude loading studied in this research,

the below-threshold minor cycles contribute to fatigue damage, and the intensity of the AE signals increases with the number of minor cycles between overloads.

From the above discussion, it is clear that the acoustic emission test data lead to a conclusion in agreement with the one drawn from the macrocrack growth rate data. Both types of test data have shown that the traditional concept of below-threshold cycles not causing fatigue damage is not valid under variable-amplitude loading conditions.

Minor Cycle Stress Ratio Effect. The test results of the third loading group were used to study the minor cycle stress ratio effect. The macrocrack growth rate data show that the complex cycle crack growth rate increases when the minor cycle stress ratio increases. The increased fatigue damage under a higher minor cycle stress ratio can be attributed to the increased minor cycle mean stress. It is also noted that in the double log coordinate system, the $\left(\frac{da}{dN}\right)_{com}$ vs. R_m curve is nearly linear.

Similarly, the test data of each AE parameter increases as the minor cycle stress ratio increases. It is concluded that fatigue damage increases with increasing the minor cycle stress ratio.

Additional Findings

Effect of Crack Increment Between Load Sheddings on (da/dN) .

An equation relating the precision of the crack growth rate to the crack increment between load sheddings has been developed for CT

specimens under constant ΔK testing. It is,

$$\psi = \frac{m \Delta a_{max}}{W(1-\alpha)(2+\alpha)} \frac{Q(\alpha)}{H(\alpha)} \times 100\% \quad (4.28)$$

Equation (4.28) shows clearly that the precision of the crack growth rate in a constant ΔK test is dependent upon the crack increment between load sheddings. A higher crack increment results in a lower precision of the crack growth rate. Furthermore, it has been shown that for a given crack increment between load sheddings, the fluctuation of the crack growth rate is equal to m times the ΔK fluctuation, where the parameter m is a material constant.

Effect of Crack Length on (da/dN) . To evaluate the effect of the crack length on the crack growth rate, the constant- ΔK loading in the fourth loading group is applied at several different crack lengths. Nearly thirty crack growth data were taken. The crack growth rate vs. crack length plot shows that all data points are distributed along a horizontal line. No significant variation trend of the crack growth rate data in response to variations in the crack length is observed. Therefore, it can be concluded that the crack length has no influence on the crack growth rate.

Intermittent Nature of AE Signals. The acoustic emission results show that the number of events recorded is always much smaller than the number of loading cycles applied. This fact indicates that measurable acoustic emission signals do not occur corresponding to every loading cycle, even for loading cycles of the same size. In

other words, acoustic emission signals from fatigue testing are of an intermittent nature. The intermittent nature of acoustic emission signals is one of the major obstacles to examining fatigue damage induced by each loading cycle, which could lead to a better understanding of the fatigue damage mechanisms under variable-amplitude loading conditions.

Striation Characteristics. According to the pattern of the striations observed, the crack surface can be divided into many small regions. Both the orientation and spacing of the striations vary from region to region. Inside each region, the striation lines are basically parallel to each other and of the same spacing. Therefore, each region can be considered as a microcrack of its particular crack growth orientation and speed. The macrocrack growth is the resultant action of all localized microcrack growths.

Evidence of abrasive damage to the striations on the fractured surfaces was also observed under the SEM. The fractured surfaces experiencing loadings of two different overload stress ratios were compared. It seems that loading of a smaller R_o results in more abrasive damage on the fractured surface.

CHAPTER V

SUMMARY AND CONCLUSIONS

Summary

Fatigue damage under variable amplitude loads has been studied using five different methods, namely, macrocrack growth, acoustic emission, crack mouth opening displacement, back-face strain, and fatigue striations. The major findings of this research are summarized below.

Discussion of the effect of the number of cycles per complex cycle on the macrocrack growth rate data has demonstrated the existence of the fatigue damage acceleration phase, the retardation phase, and the transition phase. This discussion contributes to an improved understanding of the overload effect under the isolated overload programs. The CMOD and BFS test results have revealed some characteristics of the crack opening phenomenon which are directly related to fatigue damage under variable-amplitude loading conditions. Striation observations have indicated that there exists a large difference between overload fatigue damage and minor cycle fatigue damage, which might contribute to the mechanism of fatigue damage induced by each loading cycle under variable-amplitude loading conditions.

Fatigue threshold behavior has been studied in terms of the

macrocrack growth rate and the acoustic emission intensity. The conventional concept, the ASTM recommendation, and the available test data on the minor cycle crack growth rate have been used as baselines for evaluating the threshold behavior under variable-amplitude loading conditions. The comparisons between the test data and the baselines have shown that the threshold varies with the loading conditions due to load interaction between overloads and minor cycles.

Discussion of the effects of crack increment between load sheddings on the precisions of ΔK and $\frac{da}{dN}$ in a constant ΔK test yielded meaningful results. Two equations relating the ΔK fluctuation and the $\frac{da}{dN}$ fluctuation to the crack increment between load sheddings, for CT specimens, have been developed. The approach used in the derivation can be applied to the study of the precisions of ΔK and $\frac{da}{dN}$ for other types of specimen.

Special measures have been taken to isolate noise in the acoustic emission monitoring system. The results have shown that plastic pins are a promising substitute for conventional metal pins under relatively small loadings.

Conclusions

1. Under the first loading group, acceleration occurs for $10 < n_c < 50$, retardation occurs for $n_c \geq 100$, and the transition of the overload effect lies between $n_c = 50$ and $n_c = 100$. The level of overload acceleration increases with increasing n_c until it

reaches a maximum, then falls rapidly to zero between $n_c = 50$ and $n_c = 100$. After the transition point, the level of retardation increases as n_c increases.

2. The crack is propped open following the first overload, and then remains unchanged for subsequent overloads under the second loading group. At relatively low loading levels (e.g., the first loading group), the crack may not be propped open a measurable amount.
3. All striations observed correspond to the overload cycles, which indicates that there exists a large difference between overload fatigue damage and minor cycle fatigue damage, whatever the load interaction is.
4. If previous data for the minor cycle crack growth rate are used to formulate the baseline, load interaction causes the threshold to decrease with increasing n_c for $10 < n_c < 50$, and to increase with increasing n_c for $n_c \geq 100$, under the first loading group. If the baseline is based on the conventional concept or the ASTM specifications on crack growth rate at the threshold point, load interaction causes the threshold to decrease for all n_c .
5. Fatigue damage, in terms of the crack growth rate and the intensity of the acoustic emission signals, increases as the minor cycle stress ratio increases. In the double log coordinate system, the $\left(\frac{da}{dN}\right)_{com}$ vs. R_m curve is nearly linear.
6. When the same loading spectrum was applied at various crack tip positions, no significant variation in the crack growth rate

data was observed for constant ΔK . The crack length has no influence on the crack growth rate.

7. If the crack increment between load sheddings is Δa_{max} , the resulting ΔK fluctuation in a constant ΔK test is,

$$\xi = \frac{\Delta a_{max}}{W(1-\alpha)(2+\alpha)} \frac{Q(\alpha)}{H(\alpha)} \times 100\% \quad (3.9)$$

The larger the crack increment between load sheddings, the lower the ΔK precision.

8. If the crack increment between load sheddings is Δa_{max} , the resulting fluctuation of the crack growth rate in a constant ΔK test is,

$$\psi = m \frac{1}{\Delta K} \frac{\partial(\Delta K)}{\partial(a)} (\Delta a_{max}) \times 100\% \quad (4.27)$$

The larger the crack increment between load sheddings, the lower the $\frac{da}{dN}$ precision. The $\frac{da}{dN}$ fluctuation is equal to m times the ΔK fluctuation, where m is a material constant.

9. The use of Delrin plastic pins can effectively isolate the hydraulic system noises. As compared to metal pins, the plastic pins are much cheaper and do not have measurable pin friction noises. The plastic pins perform satisfactorily under relatively low loadings.
10. Acoustic emission signals from fatigue testing are of an intermittent nature. The intermittent nature of acoustic

emission signals is one of the major obstacles to examining fatigue damage induced by each loading cycle, which could lead to a better understanding of the fatigue damage mechanisms under variable-amplitude loading conditions.

11. The complex cycle crack growth rate data calculated using the striation spacing measurements correlated with the macrocrack growth rate data calculated using the traveling microscope measurements.

Suggestions for Future Work

Further work is needed to more precisely define the transition from overload acceleration to overload retardation. A better understanding of the transition phase may provide information about when the overloads are beneficial and when they are detrimental.

Variables such as the ratio of the minor cycle stress range to the overload stress range, the overload stress ratio, and the specimen width may have influence on the overload effect. Investigation of these variables may lead to an improved understanding of fatigue damage under variable-amplitude loadings.

It is suggested that future constant ΔK tests be conducted on constant K specimens instead of CT specimens to avoid constantly calculating loading levels. To acquire stronger AE signals and better striation profiles, aerospace aluminum 7075 and 2024 may be adopted.

REFERENCES

1. Xu, Hao, Reliability Design of Mechanical Strength, Mechanical Engineering Press, Beijing, China, 1984.
2. Miner, M.A., "Cumulative Damage in Fatigue," Journal of Applied Mechanics, ASME Transactions, Vol. 67, Sept., 1945, pp. A149-A164.
3. Paris, P.C. and Erdogan, F.E., "A Critical Analysis of Crack Propagation Laws," Journal of Basic Engineering, ASME Transactions, Series D, Vol. 85, 1963, pp. 528-534.
4. Gurney, T.R., "Some Fatigue Tests on Fillet Welded Joints under Simple Variable Amplitude Loading," Research Report, The Welding Institute, May, 1981.
5. Joehnk, J.M., "Fatigue Behavior of Welded Joints Subjected to Variable Amplitude Stresses," Master's Thesis, The University of Texas at Austin, May, 1981.
6. Zwerneman, F.J. and Frank, K.H., "Fatigue Damage under Variable Amplitude Loads," Journal of Structural Engineering, Vol. 114, No. 1, 1988, pp. 67-83.
7. Rice, J.R., "Mechanics of Crack Tip Deformation and Extension by Fatigue," Fatigue Crack Propagation, ASTM STP 415, American Society for Testing and Materials, 1967, pp. 247-311.
8. Hudson, C.M. and Hardrath, H.F., "Investigation of Effects of Variable-Amplitude Loadings on Fatigue Crack Propagation

- Patterns," NASA Technical Note D-1803, August, 1963.
9. Newman, J.C., Jr., "A Finite Element Analysis of Fatigue Crack Closure," Mechanics of Crack Growth, ASTM STP 590, American Society for Testing and Materials, 1976, pp. 281-301.
 10. Engle, R.M. and Rudd, J.L., "Analysis of Crack Propagation under Variable Amplitude Loading Using the Willenberg Model, " AIAA/ASME/SAE 15th Structures, Structural Dynamics and Materials Conference, Las Vegas, Nevada, April 17-19, 1974, AIAA Paper No. 74-369.
 11. Hertzberg, R.W., Deformation and Fracture Mechanics of Engineering Materials, John Wiley and Sons, 1976.
 12. Ohrloff, N., Gysler, A., and Lutjering, G., "Fatigue Crack Propagation Behavior under Variable Amplitude Loading," Fatigue Crack Growth under Variable Amplitude Loading, Proceedings of the Third International Spring Meeting of the French Metallurgical Society, Paris, France, 1988, pp. 24-34.
 13. Petit, J., et al., "Influence of Microstructure and Environment on Fatigue Crack Propagation Affected by Single or Repeated Overloads in Al 7075 Alloy," Fatigue Crack Growth under Variable Amplitude Loading, Proceedings of the Third International Spring Meeting of the French Metallurgical Society, Paris, France, 1988, pp. 162-179.
 14. Barsom, J.M., "Fatigue Behavior of Pressure-Vessel Steels," WRC Bulletin, No. 194, Welding Research Council, New York, May, 1974.
 15. Boyer, Howard E., Atlas of Fatigue Curves, American Society for

Metals, 1986.

16. Bucci, R.J., "Development of a Proposed ASTM Standard Test Method for New-Threshold Fatigue Crack Growth Rate Measurement," Fatigue Crack Growth Measurement and Data Analysis, ASTM STP 738, American Society for Testing and Materials, 1981, pp. 5-28.
17. Fisher, J.W., et al., "Steel Bridge Members under Variable Amplitude Long Life Fatigue Loading," National Cooperative Highway Research Program Report 267, Lehigh University, Transportation Research Board, Dec., 1983.
18. Schijve, J., et al., "Crack Growth in Aluminum Alloy Sheet Material under Flight-Simulation Loading," International Journal of Fatigue, Vol. 7, No. 3, 1985, pp. 127-136.
19. Heuler, P. and Seager, T., "A Criterion for Omission of Variable Amplitude Loading Histories," International Journal of Fatigue, Vol. 8, No. 4, 1986, pp. 225-230.
20. Smith, Daniel Richard, Jr., "An Investigation of the Acoustic Emission Generated by Various Crack Propagation Modes in 304 Stainless Steel," Ph. D Dissertation, The University of Denver, 1987.
21. Blanchette, Y., et al., "Acoustic Emission Behavior during Crack Growth of 7075-T651 Al Alloy," Engineering Fracture Mechanics, Vol. 24, No. 5, 1986, pp. 647-656.
22. Tetelman, A.S. and Chow, R., "Acoustic Emission and Microcracking Processes," Acoustic Emission, ASTM STP 505, American Society for Testing and Materials, 1972, pp. 30-40.

23. Nondestructive Testing Handbook, Vol. 5: Acoustic Emission Testing, 2nd Ed., American Society of Nondestructive Testing, 1987.
24. Blackburn, P.R., "Acoustic Emission from Fatigue Cracks in Chrome-Molybdenum Steel Cylinders," Journal of Acoustic Emission, Vol. 7, 1988, pp. 49-56.
25. Lindley, T.C. and McIntyre, P., "Application of Acoustic Emission to Crack Detection and Measurement," The Measurement of Crack Length and Shape during Fracture and Fatigue, Beevers, C.T. Ed., Engineering Materials Advisory Service Ltd., West Midlands, U.K., 1981, pp. 285-344.
26. Beattie, A.G., "Acoustic Principles and Instrumentations," Journal of Acoustic Emission, Vol. 2, Nov., 1/2, 1983, pp. 95-127.
27. Bassim, M. Nabil, "Assessment of Fatigue Damage with Acoustic Emission," Proceedings of the International Conference on Acoustic Emission, Lake Tahoe, Nevada, Oct., 1985, pp. S224-S227.
28. Vetrano, J.B. and Jolly, W.D., "In-Service Acoustic Emission Monitoring of Reactor Pressure Vessels," Materials Evaluation, Jan., 1972, pp. 9-12.
29. Blackburn, P.R. and Rana, M.D., "Acoustic Emission Testing and Structural Evaluation of Seamless, Steel Tubes in Compressed Gas Service," Journal of Pressure Vessel Technology, ASME Transactions, Vol. 108, May, 1986, pp. 234-240.
30. McBride, S.L. and Maclachlan, J.W., "Acoustic Emission due to Crack Growth, Crack Face Rubbing and Structural Noise in the

- CC-130 Hercules Aircraft," Journal of Acoustic Emission, Vol. 3, No. 1, 1984, pp. 1-9.
31. Horak, C.R. and Weyhreter, A.F., "Acoustic Emission System for Monitoring Components and Structures in a Severe Fatigue Noise Environment," Materials Evaluation, May, 1977, pp. 59-63, 68.
 32. Carlyle, J.M. and Scott, W.R., "Acoustic Emission Fatigue Analyzer," Experimental Mechanics, Oct., 1976, pp. 369-372.
 33. Mills, W.J. and Hertzberg, R.W., "Load Interaction Effects on Fatigue Crack Propagation in 2024-T3 Aluminum Alloy," Engineering Fracture Mechanics, Vol. 8, 1976, pp. 657-667.
 34. Bannantine, Julie A., et al., Fundamentals of Metal Fatigue Analysis, Prentice Hall, Inc., 1990.
 35. Fleck, N.A., "Influence of Stress State on Crack Growth Retardation," Basic Questions in Fatigue, Vol. I, ASTM STP 924, American Society for Testing and Materials, 1988, pp. 157-183.
 36. Mills, W.J., Hertzberg, R.W., and Roberts, Richard W., "Load Interaction Effects on Fatigue Crack Growth in A514F Steel Alloy," Cyclic Stress-Strain and Plastic Deformation Aspects of Fatigue Crack Growth, ASTM STP 637, American Society for Testing and Materials, 1977, pp. 192-208.
 37. Abtahi, A., Albrecht, P., and Irwin G.R., "Fatigue of Periodically Overloaded Stiffener Detail," Journal of the Structural Division, Proceedings of the American Society of Civil Engineers, Vol. 102, No. ST11, Nov. 1976, pp. 2103-2119.
 38. Albrecht, P., Abtahi, A., and Irwin G.R., "Fatigue Strength of

- Overloaded Bridge Components," Civil Engineering Report, University of Maryland, College Park, MD, 1975.
39. Tokaji, K., et al., "Fatigue Crack Retardation of Low Carbon Steel in Saltwater," Journal of Engineering Materials and Technology, ASME Transactions, Vol. 106, Jan., 1984, pp. 38-42.
 40. Davidson, D.L. and Hudak, S.J., Jr., "Alterations in Crack-Tip Deformation during Variable-Amplitude Fatigue Crack Growth," Fracture Mechanics: Eighteenth Symposium, ASTM STP 945, American Society for Testing and Materials, 1988, pp. 934-954.
 41. Ward-Close, C.M., Blom, A.F., and Ritchie, R.O., "Mechanisms Associated with Transient Fatigue Crack Growth under Variable-Amplitude Loading: An Experimental and Numerical Study," Engineering Fracture Mechanics, Vol. 32, No. 4, 1989, pp. 613-638.
 42. Lankford, J. and Davidson, D.L., "The Effect of Overloads upon Fatigue Crack Tip Opening Displacement and Crack Tip Opening/Closing Loads in Aluminum Alloys," Advances in Fracture Research, Proceedings of the 5th International Conference on Fracture, Cannes, France, D. Francois et al., Ed., Pergamon Press, Oxford, U.K., Vol. 2, 1981, pp. 899-906.
 43. Christensen, R.H., Metal Fatigue, McGraw-Hill, New York, 1959.
 44. Elber, W., "The Significance of Fatigue Crack Closure," Damage Tolerance in Aircraft Structures, ASTM STP 486, American Society for Testing and Materials, 1971, pp. 230-240.
 45. Schijve, J., "Fatigue Damage Accumulation and Incompatible Crack Front Orientation," Engineering Fracture Mechanics, Vol.

- 6, 1974, pp. 245-252.
46. Jones, R.E., "Fatigue Crack Growth Retardation after Single-Cycle Peak Overload in Ti-6Al-4V Titanium Alloy," Engineering Fracture Mechanics, Vol. 5, 1973, pp. 585-604.
 47. Wheeler, O.E., "Spectrum Loading and Crack Growth," Journal of Basic Engineering, ASME Transactions, March, 1972, pp. 181-186.
 48. Schijve, J., "Lecture II - Fatigue Cracks, Plasticity Effects and Crack Closure," Engineering Fracture Mechanics, Vol. 11, 1979, pp. 182-196.
 49. de Castro, J.T.P. and Parks, D.M., "Decrease in Closure and Delay of Fatigue Crack Growth in Plane Strain," Scripta Metallurgica, Vol. 16, 1982, pp. 1443-1446.
 50. Bathias, C. and Vancon, M., "Micromechanisms of Fatigue Crack Growth Retardation Following Overloads," Engineering Fracture Mechanics, Vol. 10, 1978, pp. 409-424.
 51. Schijve, J., "The Effects of Pre-Strain on Fatigue Crack Growth and Crack Closure," Engineering Fracture Mechanics, Vol. 8, 1976, pp. 575-581.
 52. Albrecht, P. and Yamada, K., "Rapid Calculation of Stress Intensity Factors," Journal of Structural Division, Proceedings of the American Society of Civil Engineers, Feb., 1977, pp. 377-389.
 53. Forman, R.G., Kearney, V.E., and Engle, R.M., "Numerical Analysis of Crack Propagation in Cyclic-Loaded Structures," Journal of Basic Engineering, ASME Transactions, Vol. 89, No. 3, 1967, pp. 459-464.

54. Newman, J.C., Jr., "A Crack-Closure Model for Predicting Fatigue Crack Growth under Aircraft Spectrum Loading," Methods and Models for Predicting Fatigue Crack Growth under Random Loading, ASTM STP 748, American Society for Testing and Materials, 1981, pp. 53-84.
55. Newman, J.C., Jr., "Prediction of Fatigue-Crack Growth under Variable-Amplitude and Spectrum Loading Using a Closure Model," Design of Fatigue and Fracture Resistant Structures, ASTM STP 761, American Society for Testing and Materials, 1982, pp. 255-277.
56. Dill, H.D. and Saff, C.R., "Spectrum Crack Growth Prediction Method Based on Crack Surface Displacement and Contact Analyses," Fatigue Crack Growth under Spectrum Loads, ASTM STP 595, American Society for Testing and Materials, 1976, pp. 306-319.
57. Barsom, J.M., "Fatigue-Crack Growth under Variable Amplitude Loading in ASTM A514-B Steel," Progress in Flaw Growth and Fracture Toughness Testing, ASTM STP 536, American Society for Testing and Materials, 1973, pp. 147-167.
58. Fuchs, H.O., and Stephens, R.I., Metal Fatigue in Engineering, Wiley & Sons, Inc., 1980.
59. Amzallag, C., Rabbe, P., Bathias, C., Benoit, D., and Truchon, M., "Influence of Various Parameters on the Determination of the Fatigue Crack Arrest Threshold," Fatigue Crack Growth Measurement and Data Analysis, ASTM STP 738, American Society for Testing and Materials, 1981, pp. 29-44.

60. "Standard Test Method for Measurement of Fatigue Crack Growth Rates," ASTM E647-88, Annual Book of ASTM Standards, Vol. 03.01, 1989, pp. 636-654.
61. Rolfe, S.T. and Barsom, J.M., Fracture and Fatigue Control in Structures, Applications of Fracture Mechanics, Prentice-Hall, Inc., 1977.
62. Koterazawa, R., "Fatigue Crack Propagation under Periodic Overstressing," Materials, Experimentation and Design in Fatigue, Proceedings of Fatigue 81, Society of Environmental Engineers, England, March, 1981, pp. 159-169.
63. Dowling, N.E., "Estimation and Correlation of Fatigue Lives for Random Loading," International Journal of Fatigue, July, 1988, pp. 179-185.
64. "Standard Definition of Terms Relating to Acoustic Emission," ASTM Designation: E610-82, Committee on Nondestructive Testing, Subcommittee E07.04 on Acoustic Emission.
65. Pollock, A.A., Practical Guide to Acoustic Emission Testing, Physical Acoustic Corporation, Princeton, New Jersey, 1988.
66. Lindley, T.C., Palmer, I.G., and Richards, C.E., "Acoustic Emission Monitoring of Fatigue Crack Growth," Materials Science and Engineering, Vol. 32, 1978, pp. 1-15.
67. Ghorbanpoor, Alireza, "Acoustic Emission Characterization of Fatigue Crack Growth in Highway Bridge Components," Ph. D. Dissertation, The University of Maryland, Dec., 1985.
68. Morton, T.M., Smith, S., and Harrington, R.M., "Effect of Loading Variables on the Acoustic Emissions of Fatigue-Crack Growth,"

- Experimental Mechanics, May, 1974, pp. 208-213.
69. Harris, D.O. and Dunegan, H.L., "Continuous Monitoring of Fatigue-Crack Growth by Acoustic-Emission Techniques," Experimental Mechanics, Feb., 1974, pp. 71-81.
 70. Houssny-Emam, M. and Bassim, M.N., "Study of the Effect of Heat Treatment on Low Cycle Fatigue in AISI4340 Steel by Acoustic Emission," Materials Science and Engineering, Vol. 61, 1983, pp. 79-88.
 71. Hamel, F., Bailom, J.P., and Bassim, M.N., "Constructive and Destructive Interference in Acoustic Emission during Fatigue Crack Propagation," Ultrasonics, May, 1979, pp. 125-127.
 72. Schijve, J., "Observation on the Prediction of Fatigue Crack Growth Propagation under Variable-Amplitude Loading," Fatigue Crack Growth under Spectrum Loads, ASTM STP 595, American Society for Testing and Materials, 1976, pp. 3-23.
 73. McEvily, Arthur J., "On Crack Closure in Fatigue Crack Growth," Mechanics of Fatigue Crack Closure, ASTM STP 982, American Society for Testing and Materials, 1988, pp. 35-43.
 74. Davidson, David L., "Plasticity Induced Fatigue Crack Closure," Mechanics of Fatigue Crack Closure, ASTM STP 982, American Society for Testing and Materials, 1988, pp. 44-61.
 75. Zhang, S., Schulte, K, and Marisson, R., "Systematic Fracture Surface Analyses for the Evaluation of the Crack Closure Concept," Fatigue Crack Growth under Variable Amplitude Loading, Proceedings of the Third International Spring Meeting of the French Metallurgical Society, Paris, France, 1988, pp. 48-

- 63.
76. Koning, A.U. de, "Prediction of Low and High Crack Growth Rates under Constant and Variable Amplitude Loading," Fatigue Crack Growth under Variable Amplitude Loading, Proceedings of the Third International Spring Meeting of the French Metallurgical Society, Paris, France, 1988, pp. 208-217.
77. Allison, J.E., "The Measurement of Crack Closure during Fatigue Crack Growth," Fracture Mechanics: Eighteenth Symposium, ASTM STP 945, American Society for Testing and Materials, 1988, pp. 913-933.
78. Allison, J.E., Ku, R.C., and Pompetizki, M.A., "A Comparison of Measurement Methods and Numerical Procedures for the Experimental Characterization of Fatigue Crack Closure," Mechanics of Fatigue Crack Closure, ASTM STP 982, American Society for Testing and Materials, 1988, pp. 171-185.
79. Roberson, L.J. and Kirk, M.T., "A Statistical Approach to Crack Closure Determination," Mechanics of Fatigue Crack Closure, ASTM STP 982, American Society for Testing and Materials, 1988, pp. 230-246.
80. Ashbaugh, N.E., "Effects of Load History and Specimen Geometry on Fatigue Crack Closure Measurements," Mechanics of Fatigue Crack Closure, ASTM STP 982, American Society for Testing and Materials, 1988, pp. 186-196.
81. Donald, J.K., "A Procedure for Standardizing Crack Closure Levels," Mechanics of Fatigue Crack Closure, ASTM STP 982, American Society for Testing and Materials, 1988, pp. 222-229.
82. Zwerneman, F.J. and Frank, K.H., "Crack Opening under Variable

- Amplitude Loads," Fracture Mechanics: Perspectives and Directions (Twentieth Symposium), ASTM STP 1020, American Society for Testing and Materials, 1989, pp. 548-565.
83. Deans, W.F. and Richards, C.E., "A Simple and Sensitive Method of Monitoring Crack and Load in Compact Fracture Mechanics Specimens Using Strain Gages," Journal of Testing and Evaluation, Vol. 7, 1979, pp. 147-154.
84. Schijve, J., "Fatigue Crack Closure: Observations and Technical Significance," Mechanics of Fatigue Crack Closure, ASTM STP 982, American Society for Testing and Materials, 1988, pp. 5-34.
85. Forsyth, P.J.E. and Ryder, D.A., "Fatigue Fracture," Aircraft Engineering, Vol. 32, No. 374, 1960, pp. 96-99.
86. Forsyth, P.J.E. and Ryder, D.A., "Some Results of the Examination of Aluminum Alloy Specimen Fracture Surfaces," Metallurgia, Vol. 63, 1961, pp. 117-124.
87. Hertzberg, R.W. and Paris, P.C., "Application of Electron Fractography and Fracture Mechanics to Fatigue Crack Propagation," Proceeding of International Fracture Conference, Sendaim Japan, Vol. 1, 1965, pp. 459-478.
88. Engle, L. and Klingele, H., An Atlas of Metal Damage: Surface Examination by Scanning Electron Microscope, Translated by Murray Stewart, Prentice-Hall, Inc., New Jersey, 1981.
89. McMillan, J.C. and Pelloux, R.M.N., "Fatigue Crack Propagation under Program and Random Loads," Fatigue Crack Propagation, ASTM STP 415, American Society for Testing and Materials,

- 1967, pp. 247-311.
90. McMillan, J.C. and Hertzberg, R.W., "Application of Electron Fractography to Fatigue Studies," Electron Fractography, ASTM STP 436, American Society for Testing and Materials, 1968, pp. 89-123.
 91. Von Euw, E.F.J., Hertzberg, R.W., and Roberts, Richard W., "Delay Effects in Fatigue Crack Propagation," Stress Analysis and Growth of Cracks, ASTM STP 513, American Society for Testing and Materials, 1972, pp. 230-259.
 92. Morton, T.M., Harrington, R.M., and Bjeletich, J.G., "Acoustic Emissions of Fatigue Crack Growth," Engineering Fracture Mechanics, Vol. 5, 1973, pp. 691-697.
 93. Cheng, C., et al., Engineering Fracture Mechanics, National Defense Press, Beijing, China, 1978.
 94. Bernard, P.J., Lindley, T.C., and Richards, C.E., "Mechanisms of Overload Retardation during Fatigue Crack Propagation," Fatigue Crack Growth under Spectrum Loads, ASTM STP 595, American Society for Testing and Materials, 1976, pp. 78-97.
 95. Alawi, H. and Shaban, M., "Fatigue Crack Growth under Random Loading," Engineering Fracture Mechanics, Vol. 32, No. 5, 1989, pp. 845-854.
 96. Oppenheim, A.V. and Schafer, R.W., Discrete Time Signal Processing, Prentice-Hall, Inc., New Jersey, 1989.
 97. Pollock, A.A., "Threshold, Gain, Sensitivity and Noise in ICC-Based Systems," TECH NOTES, Physical Acoustic Corporation, TN-103-16-1/88, Jan., 1988.

98. Kim, Chul Jung, "Acoustic Emission Study of Fatigue Crack Extension Position in a Stress Cycles (Fracture)," Ph. D. Dissertation, Northwestern University, 1984.
99. Mathieson, P.A.R., "Acoustic Emissions from Fatigue Cracks in Steels," Ph.D. Dissertation, Cranfield Institute of Technology (U.K.), 1987.
100. Nakajima, H., et al., "Detecting Acoustic Emission during Cyclic Crack Growth in Simulated BWR Environment," Fatigue Crack Measurement and Data Analysis, ASTM STP 738, American Society for Testing and Materials, 1981, pp. 139-160.
101. Kim, C.J., Lu, Guo-Zhi, and Weertman, J., "Fatigue Crack Advance Presumably Detected by Acoustic Emission Signals," Scripta Metallurgica, Vol. 17, March, 1983, pp. 359-364.
102. Meyer, Stuart L., Data Analysis for Scientists and Engineers, John Wiley & Sons, Inc., USA, 1975.
103. Qian, M. G., Metallurgy, Shanghai Science and Technology Press, Shanghai, PRC, 1982.
104. Davidson, D. L. and Lankford, J., "Fatigue Crack Growth Mechanics for Ti-6Al-4V (RA) in Vacuum and Humid Air," Metallurgical Transactions A, Vol. 15A, October, 1984, pp. 1931-1940.
105. Radon, J. C., "Fatigue Crack Growth in the Threshold Region," Fatigue Thresholds, Fundamentals and Engineering Applications, Vol. 1, J. Backlund, A. F. Blom and J. C. Beevers (eds.), Engineering Materials Advisory Services Ltd., West Midlands, England, 1982, pp. 33-44.
106. Ray, S. K. and Grandt, A. F., Jr., "Comparison of Methods for

- Measuring Fatigue Crack Closure in a Thick Specimen," Mechanics of Fatigue Crack Closure, ASTM STP 982, American Society for Testing and Materials, 1988, pp. 197-213.
107. Spatz, C. and Johnston, J. O., Basic Statistics: Tales of Distributions, Brooks/Cole Publishing Company- A Division of Wadsworth Publishing Company, Inc., USA, 1976.
108. Ott, Lyman, An Introduction to Statistical Methods and Data Analysis, Second Edition, PWS Publishers- A Division of Wadsworth Publishing Company, Inc., USA, 1984.

APPENDICES

APPENDIX A

CONFIDENCE LIMITS OF POPULATION MEAN BASED ON A GROUP OF DATA

If a group of data has a mean of \bar{y} , then their population mean lies in a certain range around \bar{y} . Confidence limits of a mean define the variation range of the population mean with a certain degree of confidence.

The general formulas for the confidence limits of the population mean are [107],

$$UL = \bar{y} + z \frac{S}{\sqrt{N_s}} \quad (A.1)$$

$$LL = \bar{y} - z \frac{S}{\sqrt{N_s}} \quad (A.2)$$

where, UL is the upper confidence limit, LL is the lower confidence limit, z can be found from the normal-curve table [107] according to the confidence level chosen, N_s is the number of data in the group, and S is the estimate of the population variance. The estimate of the population variance can be calculated as follows,

$$S = \sqrt{\frac{\Sigma y^2}{N_s - 1}} \quad (\text{A.3})$$

where, y 's represent data in the group.

APPENDIX B

CONFIDENCE LIMITS OF POPULATION MEAN BASED ON A REGRESSION LINE

For a least-square regression line of form,

$$\hat{y} = \hat{\beta}_0 + \hat{\beta}_1 x \quad (\text{B.1})$$

the population mean of y corresponding to a specific x lies in a certain range around \hat{y} . Confidence limits of \hat{y} define the variation range of the population mean of y with a certain degree of confidence.

The limits of $\eta \times 100\%$ confidence can be calculated by the following equations [102, 108],

$$UL = \hat{y} + t_{\theta/2} S_\epsilon \sqrt{\frac{1}{n_s} + \frac{(x - \bar{x})^2}{S_{xx}}} \quad (\text{B.2})$$

$$LL = \hat{y} - t_{\theta/2} S_\epsilon \sqrt{\frac{1}{n_s} + \frac{(x - \bar{x})^2}{S_{xx}}} \quad (\text{B.3})$$

where, n_s is the number of original data for the regressive calculation, \bar{x} is the average of x 's, $t_{\theta/2}$ is the percentage point of the t -distribution corresponding to the percentage area, $\theta/2 = (1 - \eta)/2$,

and the degree of freedom, $df = n_s - 2$, and S_{xx} and S_{ε} can be calculated as,

$$S_{xx} = \Sigma x^2 - \frac{(\Sigma x)^2}{n_s} \quad (\text{B.4})$$

$$S_{\varepsilon} = \sqrt{\frac{S_{yy} - \hat{\beta}_1 S_{xy}}{n_s - 2}} \quad (\text{B.5})$$

where,

$$S_{yy} = \Sigma y^2 - \frac{(\Sigma y)^2}{n_s} \quad (\text{B.6})$$

$$S_{xy} = \Sigma xy - \frac{(\Sigma x)(\Sigma y)}{n_s} \quad (\text{B.7})$$

In general, the confidence limits of a regression line are two hyperbolas around the regression line, as shown in Fig. 55. The hyperbolas have the shortest distance apart when $x = \bar{x}$.

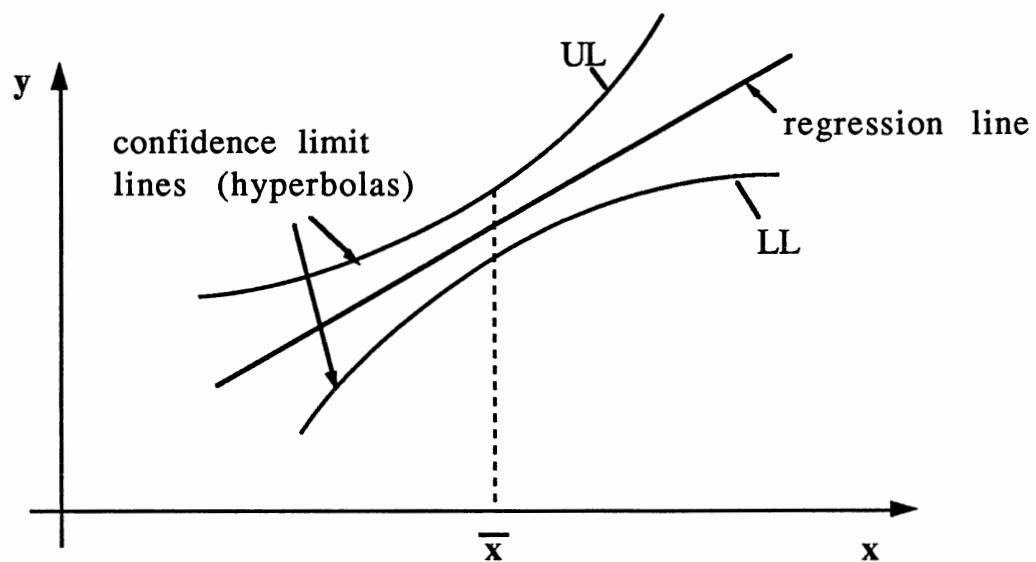


Figure 55. Shape of the Confidence Limit Lines for a Regression Line

VITA^v

Zhendong Zhou

Candidate for the Degree of

Doctor of Philosophy

Thesis: FATIGUE DAMAGE UNDER VARIABLE AMPLITUDE LOADS

Major Field: Civil Engineering

Biographical:

Personal Data: Born in Shanghai, P.R. of China, July 29, 1960, the son of mother Wenshi Hu and father Zhongmin Zhou; married to Man Liu, January 26, 1986; father of daughter Sophia Jiulin.

Education: Graduated from Tielu High School, Shenyang, P.R. of China, 1978; received the Bachelor of Science Degree in Mechanical Engineering from the Dalian Institute of Technology, PRC, in June, 1982; received Master of Science Degree in Mechanical Engineering from the Northeast University of Technology, PRC, in January, 1986; completed requirements for the Degree of Doctor of Philosophy at Oklahoma State University in July, 1991.

Professional Experience: Engineer, Research and Development Center, National Pump Company, PRC, July, 1982, to July, 1983; Research Associate, Department of Mechanical Engineering, Northeast University of Technology, PRC, August, 1983, to December, 1985; Lecturer and Research Associate, Department of Engineering Mechanics, Shenyang Polytechnic University, PRC, January, 1986, to August, 1987; Teaching Assistant and Teaching Associate, School of Civil Engineering, Oklahoma State University, June, 1988, to present.